Montanuniversität Leoben

Dissertation

Microstructure-property relationships of a novel metal-cored wire for welding of ultra-high strength steels

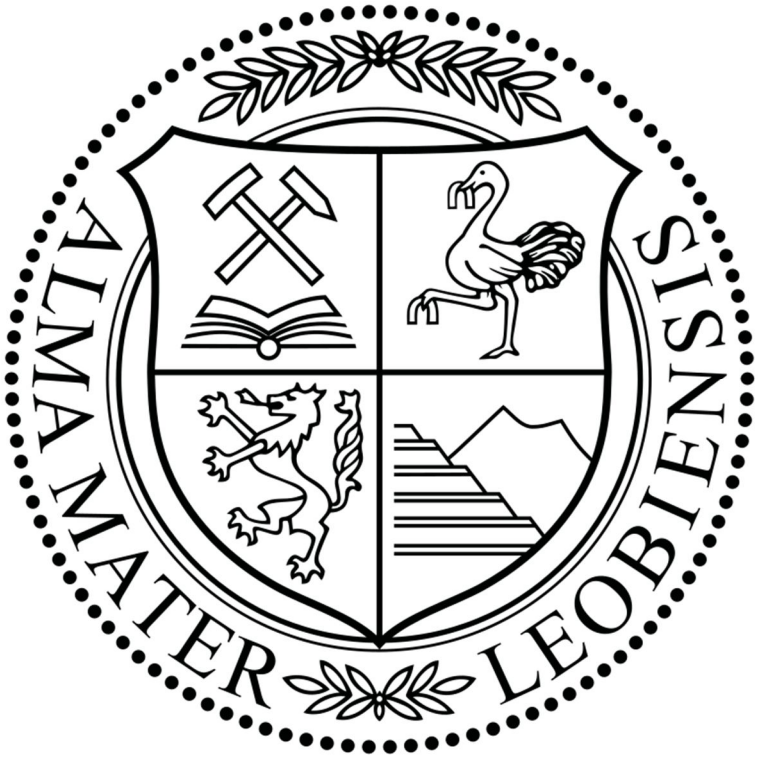

Phillip Haslberger

Leoben, March 2018

Conducted at

Department of Physical Metallurgy and Materials Testing, 8700 Leoben, Austria

in the frame of

K-Project Network of Excellence for Metal JOINing, handled by FFG.

The K-Project Network of Excellence for Metal JOINing is fostered in the frame of COMET - Competence Centers for Excellent Technologies by BMWFW, BMVIT, FFG, Land Oberösterreich, Land Steiermark, Land Tirol and SFG. The program COMET is handled by FFG.

Affidavit

I declare in lieu and oath, that I wrote this thesis and performed the associated research myself, using only the literature cited in this volume.

Leoben, March 2018 Phillip Haslberger

Danksagung

Meine persönliche und fachliche Entwicklung wäre ohne die Unterstützung durch mein Umfeld nicht möglich gewesen. Mit den folgenden Zeilen möchte ich diejenigen hervorheben, die das Entstehen dieser wissenschaftlichen Arbeit möglich gemacht und maßgeblich beeinflusst haben.

An erster Stelle gebührt mein Dank *Prof. Ronald Schnitzer*. Am Anfang des Projekts warst du noch für meinen Firmenpartner tätig und seitens der Firma bei den Projekttreffen dabei, bevor du 2016 an die Uni berufen wurdest, um den Lehrstuhl für Stahldesign zu leiten. Ich bin dir sehr dankbar, dass du mich gleich als ersten Dissertanten in den neuen Lehrstuhl übernommen hast, und von da an meine Betreuung seitens der Uni übernommen hast. Deine guten fachlichen Ratschläge und dein motivierender Führungsstil haben definitiv dazu beigetragen, dass ich jeden Tag gerne in die Arbeit gegangen bin, um mich mit hochfesten Schweißungen zu beschäftigen.

Besonders bedanken möchte ich mich auch bei meiner ersten Betreuerin als Dissertant, *Sophie Primig*. Du hast mich nach Abschluss meines Diplomstudiums mithilfe einer Ausschreibung einer hochinteressanten Dissertation so lange umgarnt, bis ich mich dazu entschloss, in Leoben zu bleiben. Damit hast du meinem Leben einen ganz gehörigen Schubser in die richtige Richtung gegeben. Deine wissenschaftliche Betreuung am Anfang der Projektlaufzeit war ebenfalls eine tolle Orientierungshilfe für den weiteren Verlauf der Dissertation.

Meine Ansprechpartner bei voestalpine Böhler Welding Austria, *Daniel Schwarz, Sylvia Holly und Hannes Pahr*, hatten dankenswerterweise immer ein offenes Ohr für meine Vorschläge zur Legierungsentwicklung und versorgten mich mit ausreichend Probenmaterial. Danke für die gute Zusammenarbeit und natürlich den finanziellen Aufwand, den voestalpine Böhler Welding Austria für meine Arbeit und die Schweißzusatzentwicklung betrieben hat.

Die Projekte M2 und M3 brachten eine lustige und konstruktive Mischung aus Werkstofflern, Schweißern und Simulanten zusammen. Die regelmäßigen Projekttreffen waren ungemein effizient darin, neue Fragen aufzuwerfen und eine kritische Sichtweise auf die Ergebnisse zu bewahren. Immer bereichernd mit dabei waren *Norbert Enzinger, Christian Schneider, Ernst Kozeschnik, Dominik Zügner, Wolfgang Ernst und Herbert Staufer*. Speziell erwähnen möchte ich auch die Heidenarbeit, die Norbert Enzinger als operativer Leiter des K-Projekts das ganze Jahr über erledigen musste, damit sich die anderen bestmöglich auf die Forschungsarbeit konzentrieren konnten. Herzlichen Dank an meine Projektpartner für die fachliche Unterstützung im Rahmen dieses sehr gut gelungenen Netzwerks. Danke auch an die

österreichische IIW Community und speziell die Grazer für die interessanten Tage und unterhaltsamen Abende bei den IIW Konferenzen.

Großer Dank gilt auch dem Department Metallkunde und Werkstoffprüfung und seinen Mitarbeitern. Die tatkräftige Unterstützung des nichtwissenschaftlichen Personals und speziell des Sekretariats war ebenso wichtig für mich wie die teils fachlichen und teils weniger fachlichen Diskussionen mit meinen Dissertanten-Kollegen. Natürlich haben sich all meine Bürokollegen ein besonderes Lob verdient. Vor allem *Christina Hofer* als meine Schwammerl-Tutorin und *Christoph Turk* als mein Diplomarbeits-Cheffe waren für mich die perfekten Bürokollegen am Anfang meiner Diss.

Mein ganzes Studium wäre wohl nicht möglich gewesen ohne die Unterstützung meiner Eltern in allen Lebenslagen. *Liebe Renate, lieber Heinz*, vielen lieben Dank, dass ihr mir das Studium ermöglicht habt und mir meinen Lebensweg so leicht wie möglich gemacht habt. Ihr habt immer gewusst, was es für mich braucht und was ihr dazu beisteuern könnt. Damit konnte ich mein Leben auf einem äußerst stabilen Fundament aufbauen.

Zu guter Letzt, und eigentlich doch allen voran, möchte ich meiner Frau *Anna* danken. Seitdem wir uns kennen, bereicherst du mein Leben jeden Tag. Die gemeinsamen Stunden mit dir und mit Kellie möchte ich gegen nichts auf der Welt eintauschen. Du gleichst mich aus und bist immer für mich da. Dank dir treibt mich wohl die beste Motivation, die es gibt: Die Motivation, für seine Familie zu sorgen.

Der Beginn aller Wissenschaften ist das Erstaunen,

dass die Dinge sind, wie sie sind.

Aristoteles

Table of Contents

Part A

Part B

List of abbreviations and symbols

APFIM	Atom probe field ion microscope
APT	Atom probe tomography
ARPGE	Automatic Reconstruction of Parent Grains from EBSD
C_{eq}	Carbon equivalent
COMET	Competence Centers for Excellent Technologies
EBSD	Electron backscatter diffraction
FFG	Österreichische Forschungsförderungsgesellschaft
GMAW	Gas metal arc welding
GT	Greninger-Troiano
HAZ	Heat affected zone
HSLA	High strength low alloy
IIW	International Institute of Welding
KS	Kurdjumov-Sachs
LOM	Light optical microscopy
LTT	Low transformation temperature
MAG	Metall-Aktivgas
NW	Nishiyama-Wassermann
SAW	Submerged arc welding
SEM	Scanning electron microscopy
SMAW	Shielded metal arc welding
TEM	Transmission electron microscopy
WD	Working distance

Part A

1 Abstract

Steel constructions for cranes or vehicles are frequently welded by gas metal arc welding. In energy efficient designs with a low component weight, thermomechanically processed ultra-high strength steels are a profound choice of material. Welding consumables for this type of steels are currently available up to a yield strength of min. 960 MPa. In the frame of this work the goal was to develop a new welding consumable with a minimum yield strength of 1100 MPa, while keeping the toughness at -20 °C above 47 J. All-weld metal samples with different alloying contents were produced for characterization of the mechanical properties and the microstructure. The objective of this thesis was especially to establish methods for an in-depth characterization of the microstructure and to correlate microstructural characteristics with the mechanical properties. A combination of light optical microscopy and electron backscatter diffraction (EBSD) was used to study the martensitic microstructure, and additionally atom probe tomography was employed for precipitate characterization. The all-weld metal is a multipass welding structure containing several sources of inhomogeneity, and the issue of sample preparation for locally restricted methods is addressed accordingly.

With a combination of these methods, the effect of several alloying elements on the microstructure and the mechanical properties of the all-weld metal was studied. Particularly high effort was expended for analyzing the effects of microalloying elements on the weld metal. The investigations showed, that all microalloying elements acted negatively on the impact toughness. Titanium and vanadium formed (Ti,V)(C,N) clusters in the weld metal and strengthened it significantly. Because vanadium exhibited a moderate toughness loss compared to the strength increase, this microalloying element was recommended for strengthening the weld metal by V(C,N) cluster formation. This strengthening concept was combined with a toughening concept. The toughness of the material was improved by reducing the contents of carbon, silicon and manganese, which resulted in a refined martensitic microstructure with a higher amount of high angle grain boundaries, thus impeding crack propagation.

Overall, the effects of changes in the alloying contents on the microstructure of the all-weld metal could be identified. The target values for yield strength and impact toughness were met. In the future, the service properties of the developed filler wire in welded joints will have to be evaluated.

2 Kurzfassung

Stahlkonstruktionen für Kräne oder den Transportsektor werden häufig mithilfe des Metall-Aktivgasschweißens (MAG-Schweißens) hergestellt. Für das Design von energieeffizienten Leichtbau-Komponenten bietet sich die Verwendung von thermomechanisch produzierten, ultra-hochfesten Stählen an. Für diese Stahlgruppe sind zurzeit Schweißzusätze bis zu einer Mindeststreckgrenze von 960 MPa verfügbar. Im Rahmen dieser Arbeit war es das Ziel, einen neuen Schweißzusatz mit einer Mindeststreckgrenze von 1100 MPa und einer Kerbschlagarbeit von mehr als 47 J bei -20 °C zu entwickeln. Es wurden Schweißgutproben mit unterschiedlichen Legierungsgehalten produziert, um die resultierenden mechanischen Eigenschaften und die Mikrostruktur zu charakterisieren. Eine Aufgabe dieser Dissertation war im Speziellen, Methoden für eine tiefgehende Charakterisierung der Mikrostruktur zu erforschen, um in weiterer Folge spezifische Merkmale der Mikrostruktur mit den mechanischen Eigenschaften des Schweißguts korrelieren zu können. Eine Kombination von Lichtmikroskopie und Elektronen-Rückstreubeugung (EBSD) wurde für die Charakterisierung der martensitischen Struktur verwendet. Ergänzend wurde Atomsondentomographie für die Analyse von möglicherweise vorhandenen Ausscheidungen eingesetzt. Da Schweißgutproben Mehrlagenschweißungen mit entsprechenden Quellen für Inhomogenitäten sind, wurde speziell die Probenvorbereitung für lokal begrenzte Methoden diskutiert.

In weiterer Folge wurde mithilfe dieser kombinierten Methodik der Einfluss mehrerer Legierungselemente auf die Mikrostruktur und die mechanischen Eigenschaften untersucht. Ein spezieller Fokus wurde auf die Einflüsse von Mikrolegierungselementen auf das Schweißgut gelegt. Es zeigte sich, dass alle Mikrolegierungselemente die Kerbschlagarbeit des Schweißguts negativ beeinflussen. Titan und Vanadium bildeten (Ti,V)(C,N) Ausscheidungen und erhöhten damit die Festigkeit des Schweißguts. Weil Vanadium eine große Festigkeitssteigerung bei moderatem Zähigkeitsverlust bewirkte, wurde dieses Mikrolegierungselement für eine Festigkeitssteigerung durch V(C,N) Ausscheidungen empfohlen. Dieses Konzept wurde mit einem Konzept zur Steigerung der Zähigkeit verbunden. Die Zähigkeit des Schweißguts wurde durch eine Absenkung des Gehalts von Kohlenstoff, Silizium und Mangan verbessert. Diese Absenkung bewirkte eine Kornfeinung der martensitischen Struktur und einen höheren Anteil von Großwinkelkorngrenzen im Material, der eine Rissausbreitung durch Rissablenkung behindert.

Zusammenfassend konnten die Einflüsse von Änderungen der Legierungszusammensetzung auf die Mikrostruktur der Schweißgutproben identifiziert werden. Die Zielwerte der mechanischen Kenngrößen wurden erreicht. In weiterer Folge müssen die Eigenschaften des Schweißzusatzes im Einsatz in tatsächlichen Schweißverbindungen evaluiert werden.

3 Introduction

Joining of materials is an omnipresent discipline of materials science. A constant demand for new processes and the ability to join new, advanced materials drives research and development in this area. The K-project metal JOINing was created to form and foster a research network dealing with various aspects of joining of materials and its simulation. The FFG provided funding in the frame of the program COMET together with several federal ministries and provincial governments. The project structure including the titles of the covered topics is outlined in figure 1. Two sections were established, dealing with joining of modern materials and the development of new, efficient welding processes. In the "Materials" section, one project dealt with joining of ultra-high strength steels. Within this project, the current thesis was created.

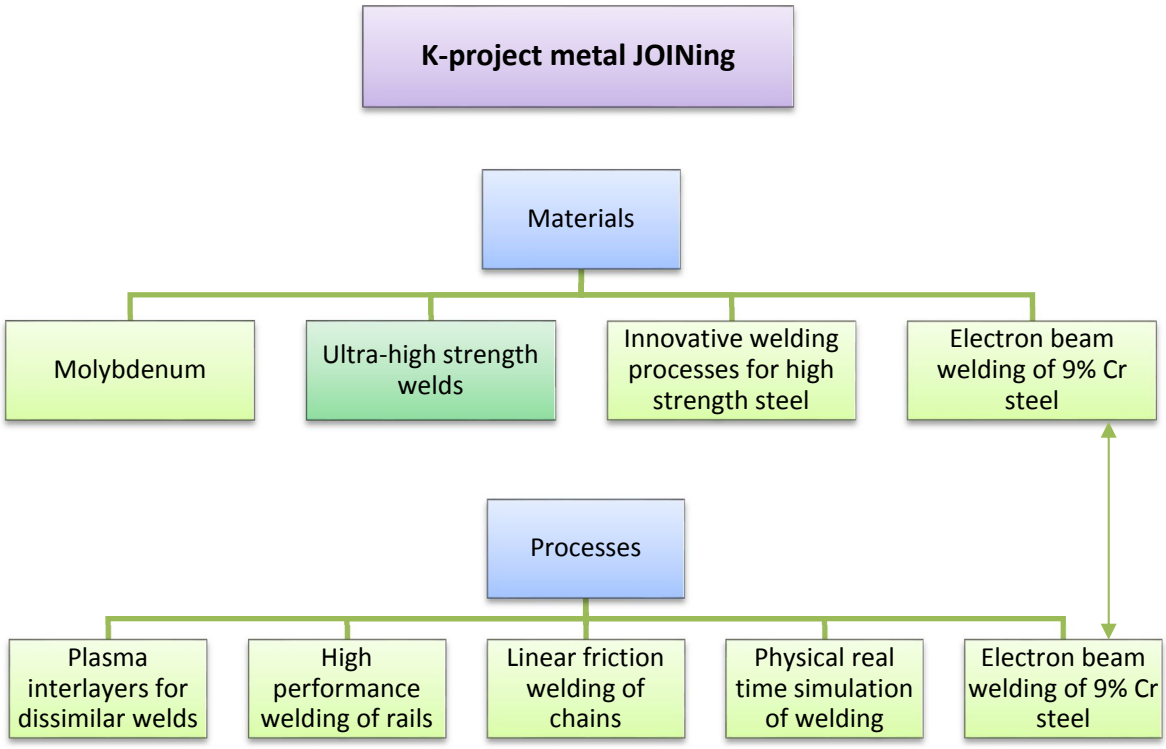

Figure 1: Project structure of the K-project metal JOINing. The current thesis is embedded in the project "Ultra-high strength welds" in the section "Materials".

Welded components are crucial parts of many steel constructions, such as cranes and vehicles. In terms of energy efficiency and cost efficiency, the use of lightweight concepts is advantageous. For the steel industry, this implies the development and use of high strength materials to be able to reduce the amount of material and maintain the load carrying capacity. Thermomechanically processed low alloy steels were recently introduced as a high strength

material with good weldability. Also the welding process plays an important role. Due to its user-friendliness, suitability for automatization and comparably low costs, gas metal arc welding (GMAW) is commonly used in these applications. Since its industrial introduction in the late 1940's and early 1950's many aspects of the GMAW process have been refined to guarantee a more stable welding system and better mechanical properties of the weld. Apart from welding parameters like current, voltage, wire feeding speed and welding position the selection of a suitable welding consumable is very important for this process. For high strength low alloy steels, several filler wires with a yield strength up to 960 MPa are available. The highest classified filler wire according to the standard EN ISO 18276 possesses a yield strength of 890 MPa. Until now, steels with a higher yield strength (i.e. 1100 MPa or higher) needed to be welded with an undermatching filler wire, making it impossible to exploit the full potential of these materials.

In the frame of the K-project metal JOINing the goal was to develop a new metal-cored filler wire with a yield strength of 1100 MPa together with the industrial partner voestalpine Böhler Welding Austria GmbH. Starting from a reference sample with min. 960 MPa yield strength the chemical composition of the filler wire was systematically varied and all-weld metal samples were produced and tested regarding their mechanical properties with tensile and Charpy V-notch tests. The alloy design involved adjustments of the most common alloying elements, and the addition of microalloying elements and more "exotic" elements. Much effort was put in studying the effect of microalloying elements on the weld metal, because their beneficial effect on both strength and toughness of common steels is well studied. The alloy design was accompanied by thermodynamic and kinetic simulations, which helped create promising alloying concepts and estimate the strength of the outcoming weld metals.

The focus of this PhD thesis was the microstructural characterization of the various samples, which was done at the Montanuniversität Leoben. The used methods ranged from light optical microscopy, scanning electron microscopy, electron microprobe and X-ray diffraction to the near atomic scale with atom probe tomography. This enabled a characterization of the material on several length scales, resolving the macroscopic appearance of the weld metal, as well as the martensitic microstructure and precipitates on a nanometer scale. The results should deepen the understanding of the microstructure-property relationships and therefore accelerate the development of this brand-new, cutting-edge filler wire. Furthermore, emphasis is put on the benefit of the used high resolution methods to the welding community.

In the following pages, this PhD thesis will summarize the state of the art and outline the most important findings of the appended publications.

4 State of the Art

4.1 Gas metal arc welding (GMAW)

The GMAW process was industrially introduced in the late 1940's and continuously improved during the following decades to optimize productivity [1]. A schematic of the process is shown in figure 2 [2]. During welding, a consumable electrode is melted off by an arc between the electrode and the workpiece and provides filler metal for the melted pool. The arc and the melted pool are shielded from the atmosphere with inert or active gases. Depending on the shielding gas, this process is also known as "metal inert gas welding" or "metal active gas welding". The electrode, the shielding gas and the welding current are fed via a water- or air-cooled welding torch [3–5].

The application areas of GMAW range from repair weldments in small craft shops to serial production of small- and medium-sized components and fabrication of large components. The high flexibility regarding weldable materials and positions, the high welding speed and the possibility for automization and roboter welding make GMAW a very economical welding process [3].

4.2 High strength steel weld metal and its microstructure

Typical high strength steel weld metals are fabricated by gas metal arc welding (GMAW), shielded metal arc welding (SMAW) or submerged arc welding (SAW), and exhibit a yield strength in a range between 500 and 1000 MPa [6]. Most grades are low alloyed and typically contain C and the most common solid solution strengtheners Si, Mn, Ni and Mo [7]. The total alloying content and especially the C content are kept low to maintain weldability [8]. For deoxidation Mn, Si, Al or Ti are added because high O contents drastically impair the impact toughness of the weld [7,9,10]. The effects of these alloying elements are described in more detail in chapter 4.3.

The welding process and its large amount of variables make the microstructure formation quite complex. During welding, the formed weld pool thermally and chemically interacts with the base material, which influences the chemical composition of the liquid metal and creates a steep thermal gradient normal to the fusion line [7,11]. The heat input causes the formation of a heat affected zone (HAZ) in the base metal. A typical macro-etched welded joint is shown in figure 3, differentiating between base metal, HAZ and weld metal.

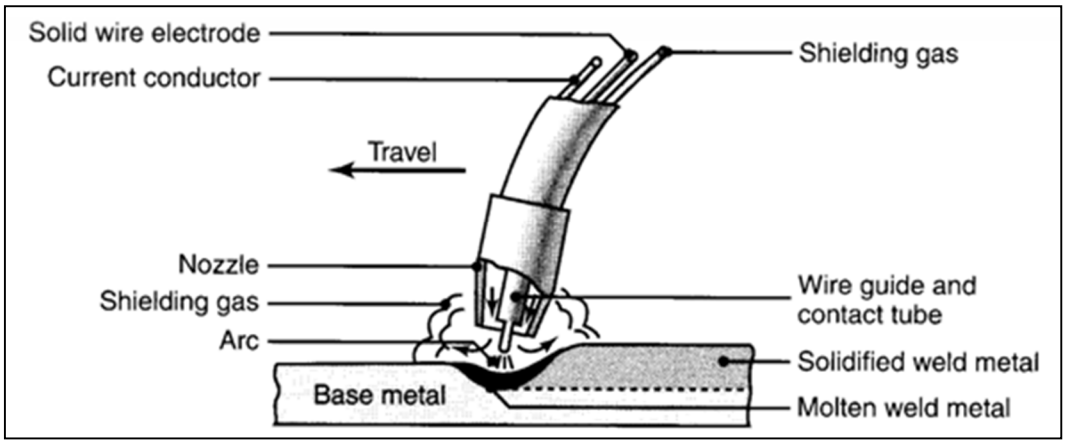

Figure 2: Schematic of GMAW process [2].

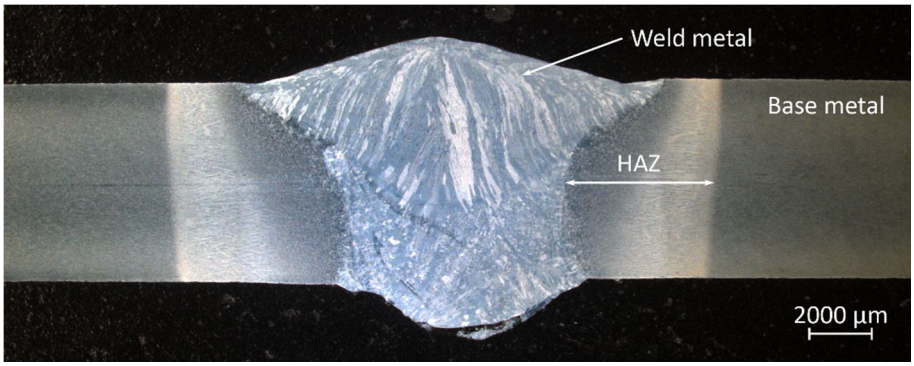

Figure 3: Macro-etched welded joint with typical denominations.

The steep thermal gradient in the weld metal leads to a directional solidification of the primary δ-ferrite grain structure [7,11] and consequently a formation of columnar austenite grains [11–17]. During this solidification process a high degree of segregation of alloying elements and impurities can occur, which is persistent throughout further cooling or short heat treatments [7]. Once the temperature is low enough, the austenitic structure will transform to the final ferritic microstructure, which strongly depends on the cooling rate.

At room temperature, the final weld usually contains a mixture of different microstructural constituents [6,7,18–23], namely polygonal ferrite, Widmannstaetten ferrite, acicular ferrite, upper and lower bainite, the martensite-austenite constituent (also known as MA-phase [24–26] or MA islands [27]) and martensite. In the past decades, many studies focused on the maximization of the area fraction of acicular ferrite both in the weld metal and in the HAZ, because this microstructure is known for its good combination of strength and toughness [7,28–39].

The acicular ferritic microstructure forms during cooling from austenite in a cooling range, which is often found in arc welding techniques and is typically associated with the formation of mixed ferritic and bainitic microstructures [40]. Acicular ferrite consists of fine interlocked ferritic laths [34,40,41]. Its appearance in the microscope is depicted in figure 4 [42]. The existence of non-metallic inclusions is required for its formation, because the first laths nucleate intragranularly on non-metallic inclusions [34]. However, a large controversy dealt with the potential of inclusions to act as nucleation sites for the ferritic laths [7,32,34,38,41]. Some considered the chemical composition of the inclusions to be less important than their size and number [32,41]. Other studies suggested that Ti-rich inclusions would be more effective than Al-rich or Mn-rich inclusions [38] or that the most important factor is a Mn-depleted zone around an inclusion [34]. Loder et al. [37] recently summarized the nucleation potential of many inclusion types. Most of the active inclusion types were rich in Ti, which supports the claim of Evans [38] that the Ti content has to be controlled in order to maximize the amount of acicular ferrite in the material. As acicular ferrite formation is competing with the formation of bainite and other ferritic phases, these need to be suppressed to maximize the amount of acicular ferrite. Bainite and Widmannstaetten ferrite typically nucleate at prior austenite grain boundaries [42]. Consequently, an increase in prior austenite grain size or the formation of allotriomorphic ferrite will suppress the formation of bainite and Widmannstaetten ferrite, because a large prior austenite grain size reduces the nucleation sites available, and the formation of allotriomorphic ferrite renders the prior austenite grain boundaries inert for bainite nucleation [40]. This is schematically shown in figure 5 [42]. The beneficial effect of a large prior austenite grain size for the acicular ferrite formation was confirmed by Vanovsek et al. [39].

If these metallurgical measures work, the formation of acicular ferrite at the surfaces of non-metallic inclusion will be energetically most favourable. The ferritic laths will grow into the austenitic matrix in different directions, leading to a star-like morphology [43,44]. During growth the laths maintain a Nishiyama-Wassermann (NW) [45] or a Kurdjumov-Sachs (KS) [46] orientation relationship with the prior austenite [47]. Subsequently, the fine interlocked microstructure is built by sympathetic nucleation on already formed laths, and impingement or intersection of already formed laths [34,44]. The final microstructure will contain fine grains with a high amount of high angle grain boundaries, which impedes both dislocation movement and crack propagation [47,48]. This explains the well-balanced strength and toughness properties of acicular ferrite.

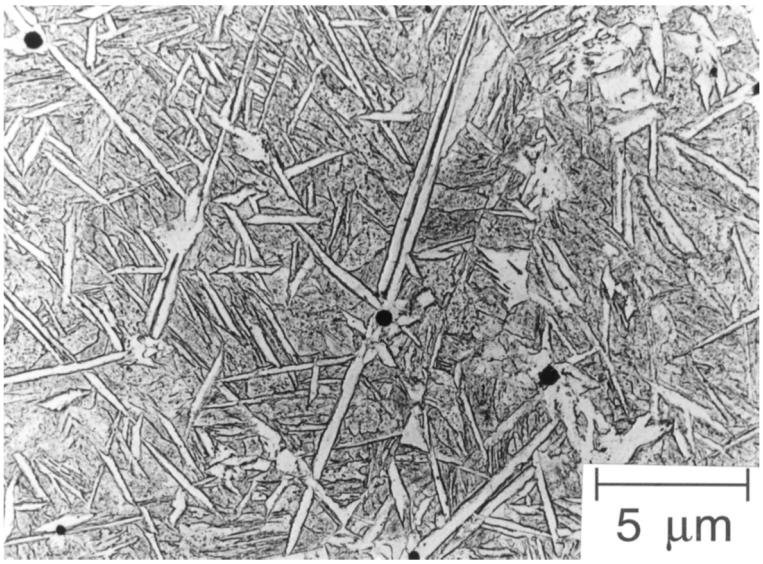

Figure 4: Appearance of acicular ferrite in an electron microscope. The first acicular ferrite laths will form on non-metallic inclusions. The final microstructure consists of interlocked ferritic laths [42].

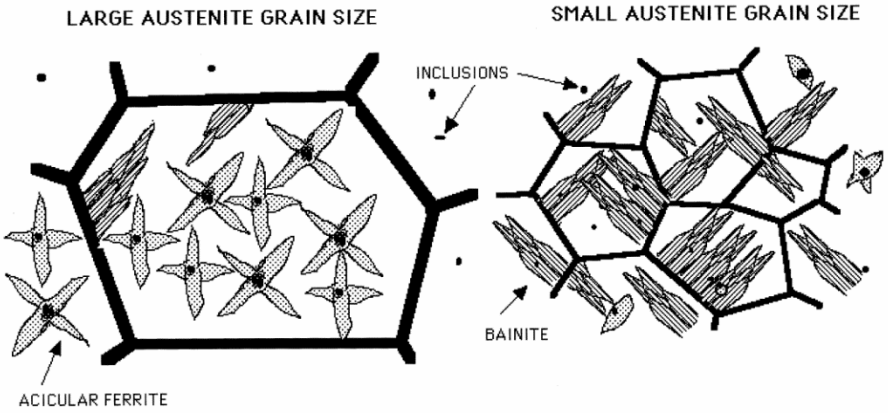

Figure 5: Influence of the prior austenite grain size on the formation of acicular ferrite [42].

At levels above 600 MPa yield strength the microstructure will shift from predominantly acicular ferrite to predominantly bainite and martensite [23,49,50]. In this type of material, a new microstructural constituent was identified as coalesced bainite and extensively studied [51–53]. It was concluded, that these large grains form by coalescence of several bainitic laths, resulting in the morphology depicted in figure 6 [53]. Keehan et al. proposed, that coalesced bainite is detrimental to the impact toughness of the weld metal because of its coarse scale [54]. He suggested, that the amount of coalesced bainite in the weld should be controlled by decreasing Ni and Mn contents [54,55].

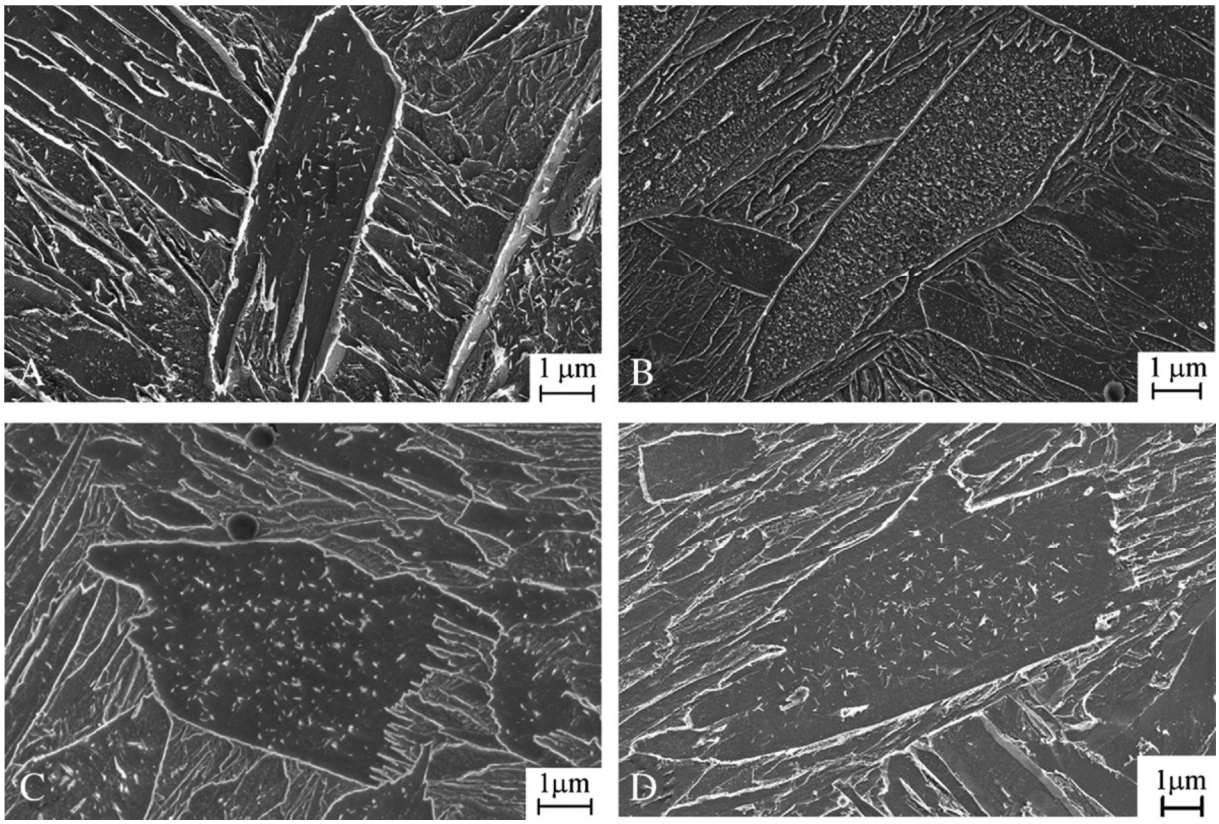

Figure 6: Typical appearance of coalesced bainite in the SEM, showing its large size compared to the surrounding microstructure [53].

At a level of 1000 MPa, the weld metal will mainly consist of martensite, bainite and small amounts of retained austenite or MA-phase [19,56]. The microstructural constituent known as MA-phase was mainly investigated due to its appearance in the intercritical HAZ of single-pass and multi-pass steel welds [24,27]. These blocky islands or interlath films consist of high carbon martensite mixed with retained austenite [26]. MA-islands can additionally contain cementite [57]. The MA-phase forms from carbon enriched austenite islands during accelerated cooling. The fresh martensite has a particularly high hardness and deteriorates the toughness and ductility of the steel by local crack initiation or matrix debonding [24–27,58]. Especially MA-phase aligned at prior austenite grain boundaries is detrimental to the mechanical behavior of the material [24,59].

Extensive studies on the microstructure of welds with 1000 MPa or more are rare because of their novelty. The current doctoral thesis and the appended publications are intended to shed light on the microstructure of this class of weld metal.

Apart from the static strength, also fatigue strength is a key property for steel welds. Several studies suggest that the residual stress state of the material is very important for its fatigue performance [60–63]. Due to the thermal contraction during cooling and possible geometric

constraints, tensile residual stresses will form in the weld metal and in the HAZ. Tensile residual stresses can severely reduce the lifetime of a component. Contrarily, the lifetime can be prolonged by introducing compressive residual stresses. This assumption led to the development of low transformation temperature (LTT) filler wires [61]. These wires contain high contents of alloying elements, which retard ferrite, pearlite and bainite formation (typically Cr and Ni, occasionally small additions of Mn and Mo). A comprehensive summary of different LTT wires, including their chemical composition, can be found in a paper by Ooi et al. [61]. Optimum properties were found for wires with a martensite start temperature of ca. 200 °C, which engenders a martensite finish temperature close to room temperature [64]. When the austenite transforms to martensite during cooling, the accompanying volume expansion due to the transformation induces compressive stresses in the weld metal. These stresses counteract and reduce the tensile residual stresses, which build up linearly during cooling. This reduction of tensile residual stresses improves the fatigue lifetime of the component [61]. The resulting microstructure of LTT wires should be fully martensitic. Nevertheless, the static yield strength of this kind of weld metal is usually in the range of 600-900 MPa [61]. Additionally, the high alloying content makes LTT wires quite costly.

4.3 Alloying elements and their strengthening and toughening potential

Microstructure and mechanical properties of high strength steel welds are controlled by a deliberate addition of alloying elements. The most important alloying element in steels is C, and it also affects the properties of steel welds greatly [7]. It influences the formation of microstructural constituents substantially and has a great strengthening potential [10]. The C content in high strength steel welds is usually restricted to 0.2 wt.% because of the risk of cold cracking [65] and the occurrence of brittle fracture in the material [7]. Optimum C contents for many different types of deposits are between 0.07 and 0.10 wt.% [10]. Si also shows a strong solid solution strengthening effect, which is even more pronounced in weld metal compared to parent metals [10]. It is used to deoxidize the material and promotes the formation of acicular ferrite [66]. However, even at small amounts it is detrimental to toughness due to the formation of martensite and/or austenite microphases in combination with the strength increment [7]. The austenite stabilizers Mn, Ni and Cu lower the austenite to ferrite transformation temperature, which generally results in a refined microstructure. Additionally, these elements act as solid solution strengtheners [7,67]. Cu was also found to form precipitates upon aging or during multipass welding, but only in combination with an impairment of toughness [67–71]. Cr and Mo suppress the austenite to ferrite transformation

kinetically and harden the material [7]. Mo is reported to deteriorate the impact toughness even at concentrations as low as 0.1 wt.% [10,72].

The mentioned alloying elements also play a great role in defining the properties of the HAZ of a weld. The weldability of high strength steels can be diminished by a high hardness in the HAZ, which can induce cold cracking, and the presence of impurities (P, S, O, N, H, Cu, Ab, As), which can impair toughness properties or cause hot cracking [73]. The hardenability of the HAZ and the corresponding susceptibility for cold cracking is described by the carbon equivalent (C_{eq}). For low heat input processes, the C_{eq} defined by the IIW is [73]:

$$C_{eq} = C + \frac{Mn}{20} + \frac{Mo}{15} + \frac{Ni}{40} + \frac{Cr}{10} + \frac{V}{10} + \frac{Cu}{20} + \frac{Si}{25}$$

If the C_{eq} is higher than 0.2 %, preheating may be necessary during welding to reduce the cooling rate in the HAZ and consequently restrict the formation of brittle phases.

A concept, which is frequently used in conventional high strength low alloy steels, is microalloying with Ti, Nb, V or Al, with the goal to refine the grain size or to induce precipitation. T. Gladman's book "The physical metallurgy of microalloyed steels" [74] and a comprehensive review by R. Lagneborg et al. [75] on "The role of Vanadium in microalloyed steels" provide a well-documented overview of this concept and its applications. The microalloying elements generally show a high affinity to C and N. This can be expressed by the solubility products of the corresponding carbides and nitrides at different temperatures, which is summarized for all microalloying elements in figure 7 [75]. TiN is the most stable compound and can still be present in liquid steel. VC has a comparably high solubility and can be dissolved at low temperatures in the austenite range. For each element, the carbide shows a higher solubility than the nitride. Or in other words, the nitride will be stable up to higher temperatures. All carbides and nitrides except AlN are mutually soluble due to their identical cubic crystal structure and their very similar lattice parameter. If C and N are present in the steel, carbonitrides will form. Similarly, if several microalloying elements are present, the resulting precipitates will be precipitates with mixed chemical composition [74,75].

Depending on the desired effect on the microstructure, an appropriate microalloying element has to be picked. The following paragraphs summarize the most important properties and effects of the different microalloying elements.

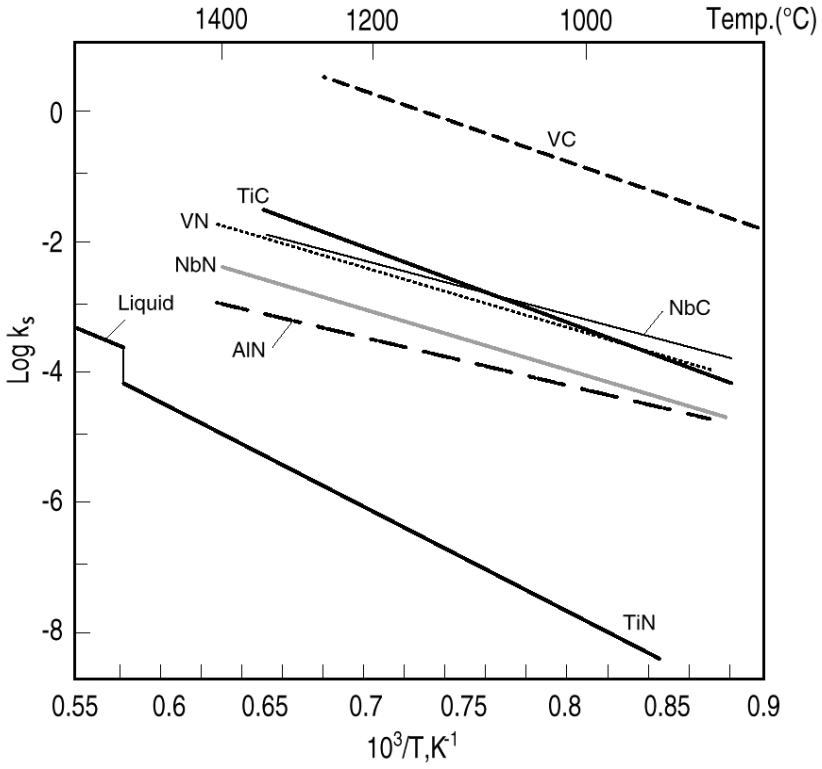

Figure 7: Summary of the solubility of several microalloy carbides and nitrides in steel [75].

Ti is commonly added to control the grain size and prevent grain growth during initial cooling and heat treatments [76]. The TiN particles are stable and retain their size up to about 1250 °C, and hinder grain coarsening by pinning the austenite grain boundaries. This effect is also used to improve the HAZ properties of weldments, where the existence of a TiN dispersion promotes a fine microstructure in reaustenized areas [74]. For a suitable size distribution and number of precipitates the ratio Ti/N has to be adjusted to about 2 [76]. One group of researchers pursued the idea of using TiB_2 as a grain refining agent in steel castings [77]. Experiments revealed, that BN and Ti(C,N) formed instead of TiB_2 which pinned the austenite grain boundaries [78].

Nb is frequently used in thermomechanically processed steels and shows three main effects: austenite grain refinement, retardation of recrystallization, and retardation of the γ/α-transformation [79,80]. The main mechanisms responsible for this behavior are the strong solute drag effect of Nb in solid solution [81], and the Zener drag created by Nb(C,N) precipitates [74]. The Nb(C,N) particles are usually formed by strain-induced precipitation, which makes this microalloying element especially interesting for hot-rolled steels [82].

VC and VN are mainly used for precipitation strengthening due to their higher solubility in ferrite and austenite compared to other microalloy carbides and nitrides [74,75,83,84]. These

precipitates form either during the γ/α-transformation via interphase precipitation or from a supersaturated ferrite during tempering. Interphase precipitates are aligned in regularly arranged lines, which originate from a repetitive nucleation at the interface of the propagating γ/α-transformation front [75,84–86]. Upon faster cooling V will stay in solid solution down to room temperature [74]. During reheating below 700 °C general precipitation of V(C,N) will occur, which results in a random distribution of precipitates [84]. As VN is more stable than VC, the first V(C,N) particles formed will be rich in N. Only when no more N is available for precipitate formation, the particles will become enriched in C [75]. Apart from its potency for precipitate formation, V was also found to promote the formation of acicular ferrite [87,88]. It was suggested, that intragranular segregation of V may facilitate the nucleation of acicular ferrite laths [88].

Al is often alloyed as a deoxidizing agent due to its strong affinity to oxygen [74]. This results in clean steels with high toughness. If both Al and N are available in the ferritic matrix, hexagonal AlN will form, which refines the prior austenite grain, strengthens the material and removes free N from the matrix [74].

Some research groups reported on the effect of more “exotic” alloying elements on steels, and more particularly on steel welds. Particular attention was paid to the existence of different types of inclusions in the weld metal. Trindade et al. [89] proposed, that an addition of 50 ppm Zr refines the microstructure by promotion of acicular ferrite formation on ZrO_2 particles. Another group showed, that an addition of Zr to self-shielded arc welds alters the inclusion landscape by capping spinel oxides and preventing their agglomeration [90]. A similar mechanism was found in flux-cored arc welds with Mg additions, where Al-Mg-O inclusions were capped by MgO, preventing their growth and consequently improving the impact toughness [91].

Based on the summarized information from literature, the alloying content was varied in the current project to study and confirm the effect of different alloying elements on the properties of the weld metal.

4.4 Characterization of high strength steel weld metal

The characterization of high strength steel weld metal has to span several length scales; from the macroscopic geometry and size of the weld beads down to nm-sized precipitates. Metallographic samples of weldments are typically prepared in cross-sections, because in many cases this viewing direction reveals all necessary macroscopic and microscopic features.

Macro-etching with Nital or similar etchants [92] is frequently used to produce macrographs for several purposes. Macrographs help to determine the optical appearance of the weld and its geometry, and to identify the size and shape of the HAZ [14,22,35,60,72,93–95], as is shown in figure 3. The existence of defects prior to service can be evaluated [22] and fracture locations after service can be depicted [96,97]. The macrographs serve as basis for an illustration of the location of samples for mechanical testing or microscopy [36,39,93,98] and can be superimposed with hardness maps or residual stress maps [60,61,70,96,97,99,100]. This is exemplified in figure 8, which shows a hardness mapping covering a large part of an all-weld metal sample. On a mesoscale, the columnar grain structure is often depicted for an assessment of the column size [12,13,39,72,101] or is analyzed in multipass welds together with reheated fine grained zones for a comparison to impact toughness [14,15,17,93,99,101–103]. The column size is usually defined by the columnar width, which is measured by the linear intercept method [11]. In low strength steel weldments, the prior austenite grain columns can be easily identified by a ferritic seam decorating the prior austenite grain boundaries [11,13,104]. In steel weldments with higher strength, the formation of ferrite at the prior austenite grain boundaries is suppressed. For a determination of the column width, contrast has to be produced by a suiting etchant and image processing [39].

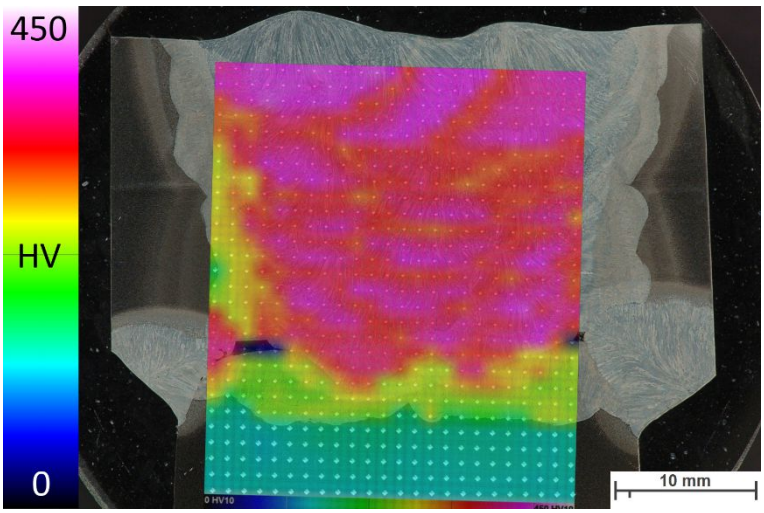

Figure 8: Macro-etched sample superimposed with hardness mapping.

A more detailed look at the microstructure of steel welds usually reveals a mixture of different microstructural constituents, as mentioned earlier. In general, the characterization method is chosen to guarantee a clear distinction of these constituents and to enable the determination of an area fraction for each constituent [6,7,19–23,105]. The classification of the ferritic constituents in the weld metal was approached by several research groups with different

systems [7], which can lead to confusion in both reading and presentations. Sub-commission IX-J of the International Institute of Welding (IIW) put much effort in a standardization of these classifications and published guidelines for a consistent identification of constituents [106]. Nevertheless, new systems emerged, adapting the IIW scheme with suggested improvements [107,108]. Independent of the used system, the constituents are usually identified from light optical micrographs or scanning electron micrographs. For this type of material, the achievable resolution is high enough for a clear resolution of the microstructure. In rare cases transmission electron microscopy (TEM) was applied for a more detailed view on lath-like ferritic structures or the nucleation of acicular ferrite on inclusions [6,23,56]. Although these techniques work well for mixed microstructures and the correlation of a mixed microstructure to toughness [7], the current thesis uses more suiting methods for the characterization of a fully martensitic microstructure with precipitates. The next chapters deal with the main methods, electron backscatter diffraction and atom probe tomography.

4.5 Electron backscatter diffraction (EBSD) and displacive transformations in steel

EBSD is a frequently used method in modern materials science, which provides crystallographic information of the investigated material. The information can help to recognize existing phases, to determine texture components or local strains, and to investigate grain structures and sizes in all kinds of materials. Several comprehensive books and reviews are available dealing with the working principle and main applications of EBSD [109–112]. Modern measurement systems with a fast high resolution camera and a field emission gun as electron source enable the investigation of fine grained steel microstructures [113].

Especially the understanding of displacively transformed microstructures in steel was deepened significantly in the course of the last years. The crystallographic morphology of acicular ferrite, upper bainite, lower bainite and martensite was described by Gourgues et al. [47]. They summarized characteristics for each constituent, such as grain boundary misorientation distributions and texture preferations. The hierarchic structure of bainite and martensite was described by several Japanese studies [114–119]. As outlined in figure 9 from Ungár et al. [120], the parent austenite grain is divided into packets, which contain blocks with overall six variants. These blocks are built up by sub-blocks comprising numerous laths [118]. The packet size and block size are linearly dependent on the prior austenite grain size [116,121]. Various studies characterized bainitic or martensitic microstructures at room

temperature and their orientation relationship to the prior austenite grain. This parent/daughter orientation relationship was first described many decades ago, and these early findings are still frequently cited as the Kurdjumov-Sachs (KS) relationship [46], the Nishiyama-Wassermann (NW) relationship [45], and the Greninger-Troiano (GT) relationship [122]. These orientation relationships can be used to reconstruct the prior austenite grain structure. Some groups refined the orientation relationships for better results of their reconstructions [123–125]. One reconstruction approach is to analyze pole figures from the original EBSD measurement, because the max. 24 martensite variants forming within one prior austenite grain produce a characteristic pattern in the pole figure [126–128]. Other methods use a nucleation and growth approach and compare adjacent data points [124,129–131]. A commercially available software was developed by Cayron et al. [130–133] using the nucleation and growth process. This software called ARPGE (Automatic Reconstruction of Parent Grains from EBSD) allows a fast and automated reconstruction of the prior austenite grains with KS, NW or GT relationship.

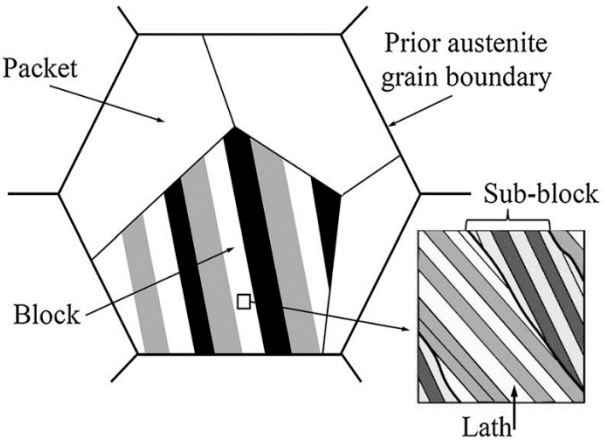

Figure 9: Hierarchic structure of lath martensite [120].

4.6 Atom probe tomography (APT) and precipitate characterization in steel

APT combines nearly atomic resolution with the information on the chemical identity of all involved atoms. Developments in the last decades facilitated 3D atom probe with a position-sensitive detector, a local electrode and, by implication, 3-dimensional reconstructions of the measurements [134,135]. Therefore, it is eminently suited for the characterization of precipitates or nanoscale segregations in a material. With the advance of laser-assisted atom

probe the range of examinable materials was drastically broadened [136]. The laser allowed the analysis of electrically isolating materials and brittle materials. Basic reviews on the method itself, the physics behind it and its applications can be found elsewhere [136–138].

After reconstruction of the measured volume, microstructural features can be visualized, such as clusters or precipitates. Depending on the size of the clusters, the identification method needs to be chosen accordingly. For well-defined clusters and precipitates, the maximum separation method or the creation of isoconcentration surfaces are suitable for an evaluation of their number, size and chemical composition [137,139]. Since 3-dimensional atom probe in its early stages was applied for the characterization of precipitation processes in Al-Mg-Si alloys [140] and pressure vessel steels [141], many alloy systems have been studied. The precipitate evolution in microalloyed steels was studied extensively, confirming the knowledge summarized by Gladman in his book in 1997 [74]. It was shown, that alloying with Ti and Nb will result in precipitates with a TiN core and a NbC shell due to their different thermal stability [142], and that the Nb-rich shell can incorporate Mo [143]. A study on a Nb-alloyed steel proved, that as little as four minutes at 700 °C suffice to drastically strengthen the material by formation of Nb(C,N) clusters [144]. V is known to form precipitates via interphase or random precipitation, and the resulting V(C,N) precipitates and their distribution were studied as well [85,145].

Despite its potential for a thorough characterization of steel on a nanoscale, the use of APT in the welding community is very limited. The atom probe field ion microscope (APFIM), the predecessor of the 3D atom probe, was used in the 90’s to study the segregation of alloying elements to ferrite-austenite grain boundaries, which were mainly enriched in C and B [146,147]. Since 2000, most APT investigations of welds focused on reactor pressure vessel steels and the evolution of Cu precipitates [70,71,141,148–150].

4.7 Relation of the current thesis to the state of the art

The current thesis is built upon a combination of knowledge on steel welds and their microstructure, martensite and its microstructural hierarchy, microalloying elements and their beneficial effects, and finally modern characterization techniques with a high spatial resolution. Until now, the welding community concentrated on the characterization of mixed steel microstructures and the classification of the contained microstructural components. In most cases, LOM and SEM were enough to gain the information needed and draw connections

to the mechanical properties. Only in rare cases, more advanced techniques like EBSD, TEM or APT were used.

The current thesis intends to outline the usefulness of these advanced techniques and give guidelines for an efficient high resolution microstructural characterization of all-weld metal samples. In a further step, the author wants to contribute to the knowledge of the microstructure-property relationships of this class of material by applying these techniques and comparing the analyzed microstructure to the mechanical properties. The effect of various alloying elements on both microstructure and mechanical properties should be clarified and be discussed in the nature of already existing literature.

5 Summary of Publications

5.1 List of publications

5.1.1 Appended papers

All appended papers can be found in part B of this thesis.

Paper I:

Haslberger P, Ernst W, Schnitzer R (2016)

Mikrostrukturielle Charakterisierung von ultra-hochfesten Schweißgütern

Berg- und Hüttenmännische Monatshefte 61: 321-324

DOI: 10.1007/s00501-016-0494-2

Paper II:

Haslberger P, Holly S, Ernst W, Schnitzer R (2017)

Microstructural characterization of martensitic all-weld metal samples

Practical Metallography 54: 513-532

DOI: 10.3139/147.110464

Paper III:

Haslberger P, Ernst W, Schnitzer R (2017)

High resolution imaging of martensitic all-weld metal

Science and Technology of Welding and Joining 22: 336-342

DOI: 10.1080/13621718.2016.1240980

Paper IV:

Haslberger P, Holly S, Ernst W, Schnitzer R (2018)

Precipitates in microalloyed ultra-high strength weld metal studied by atom probe tomography

Accepted for publication in Welding in the World

Paper V:

Haslberger P, Holly S, Ernst W, Schnitzer R (2018)

Microstructure and mechanical properties of high-strength steel welding consumables with a minimum yield strength of 1100 MPa

Journal of Materials Science 53: 6968-6979

DOI: 10.1007/s10853-018-2042-9

Paper VI:

Haslberger P, Ernst W, Schneider C, Holly S, Schnitzer R (2018)

Influence of inhomogeneity on several length scales on the local mechanical properties in V-alloyed all-weld metal

Submitted to Science and Technology of Welding and Joining

Contributions of the author: The author of this thesis is responsible for planning, conception and writing of all papers. The all-weld metal samples were supplied by voestalpine Böhler Welding Austria GmbH, where also the chemical compositions of the alloys and their mechanical properties were measured. All microstructural investigations (both experiments and data evaluation) were carried out and interpreted by the author of this thesis. Following results were produced externally:

Paper IV: The electron microprobe analysis was conducted at voestalpine Stahl Donawitz GmbH.

Paper VI: The sub-sized Charpy V-notch tests were carried out at voestalpine Stahl GmbH. The hardness mappings were conducted at TU Graz. The electron microprobe analysis was conducted at voestalpine Stahl Donawitz GmbH.

Ronald Schnitzer, Wolfgang Ernst, Sylvia Holly and Christian Schneider are gratefully acknowledged for their help and for their valuable input.

5.1.2 Co-authored papers related to this work

Schnitzer R, Zügner D, Haslberger P, Ernst W, Kozeschnik E (2017) Influence of alloying elements on the mechanical properties of ultra-high strength weld metal. Science and Technology of Welding and Joining 22:536-543.

Holly S, Haslberger P, Zügner D, Schnitzer R, Kozeschnik E (2018) Development of high-strength welding consumables using calculations and microstructural characterization. Welding in the World.

5.1.3 Conference contributions

Haslberger P, Ernst W, Schnitzer R (2016) Mikrostrukturielle Charakterisierung von ultra-hochfesten Schweißgütern. ASMET-Forum Junge Forschung, Leoben.

Haslberger P, Ernst W, Schnitzer R (2016) IIW Document IX-L-1156-16: High resolution imaging of martensitic all-weld metal. IIW Intermediate Meeting, Madrid, and IIW Annual Assembly, Melbourne.

Haslberger P, Holly S, Ernst W, Schnitzer R (2017) Precipitates in microalloyed all-weld metal of ultra-high strength steel studied by atom probe tomography. 63rd Metallkunde-Kolloquium, Lech am Arlberg.

Haslberger P, Holly S, Ernst W, Schnitzer R (2017) IIW Document II-C-534-17: Precipitates in microalloyed ultra-high strength weld metal studied by atom probe tomography. IIW Intermediate Meeting, Trollhättan, and IIW Annual Assembly, Shanghai.

Haslberger P, Ernst W, Schneider C, Holly S, Schnitzer R (2018) IIW Document II-C-550-18: Influence of inhomogeneity on several length scales on the local mechanical properties in V-alloyed all-weld metal. IIW Intermediate Meeting, Genova.

5.1.4 Supervised theses

Stadler M (2016) Vergleichende Analyse von Laser- und Voltage-Spektren von Atomsonden-messungen an ultra-hochfesten Stahl-Schweißnähten. Bachelor thesis, Montanuniversität Leoben.

Pranger M (2017) Vergleich der Mikrostruktur ausgewählter hochfester Schweißungen. Master thesis, Montanuniversität Leoben.

Schönmaier H (2018) Restaustenit in ultra-hochfestem Schweißgut. Master thesis (currently ongoing), Montanuniversität Leoben.

5.2 Summary of published contents

5.2.1 Aim and scope of the investigations

In the course of the K-project metal JOINing the goal was to develop a new metal-cored filler wire for gas metal arc welding with a target yield strength of 1100 MPa and a target impact toughness of 47 J at -20 °C. Based on the approximate totalized content of alloying elements and the used welding parameters, a martensitic microstructure was expected in the weld metal. After reviewing the existing literature and the knowledge on the microstructure-property relationships of HSLA steels in general, the contents of alloying elements were systematically varied to study their influence on the martensitic microstructure and the mechanical properties. Additional alloying elements were introduced because of their known beneficial effects on several classes of steel, particularly the microalloying elements Ti, Nb, V and Al. In order to reduce the necessary experimental efforts, thermodynamic and kinetic simulations were conducted by colleagues from the TU Wien using MatCalc [151,152]. Their predictions on strength and precipitation kinetics of the all-weld metal aided in suggesting promising alloying contents.

The mechanical properties of the experimental filler wires were measured on specimens prepared from all-weld metal samples according to DIN EN ISO 15792-1. These samples were welded in seven layers with three weld beads per layer, after the base material was buffered. This is schematically shown in figure 10. The buffering prevents a dilution of the weld metal and the base metal, which simplifies the comparison between different filler wires.

The in-depth microstructural characterization of the all-weld metal samples, which was carried out mainly at the Montanuniversität Leoben, was intended to answer the following questions:

- Which methods are well-suited for a thorough characterization of martensitic weld metal, which occasionally contains nm-sized precipitates? From a methodical point of view, this involves the issue of sample preparation, time consumption and costs of the used apparatus, resolving power of the used apparatus, and effort of data evaluation.
- How is the behavior of the weld metal regarding solidification structure and prior austenite grain structure? How can these structures be visualized in the microscope?
- Is the studied weld metal fully martensitic at room temperature? How does the martensite look like, and how is it affected by changes in alloying contents?

- Do the microalloying elements induce precipitation in the weld metal? Which microalloying elements are most beneficial for the resulting mechanical properties?
- Which connections can be made between alterations in the microstructure and corresponding changes in the mechanical properties?
- How does the thermal inhomogeneity due to the multipass technique influence the mechanical properties and the complexity of microstructural characterization? Is it possible to study the microstructure of the thermally unaffected last deposited bead, and correlate its microstructure to the mechanical properties of the whole weld?

These questions are discussed in the following pages with respect to the published papers appended to this thesis.

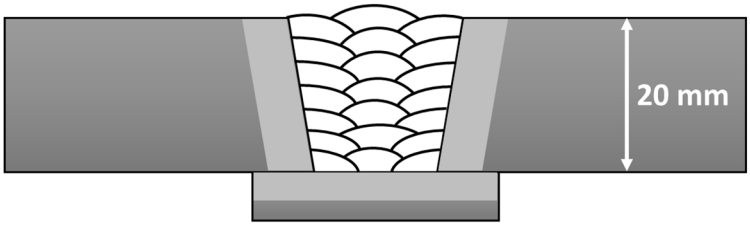

Figure 10: Sketch of all-weld metal sample according to DIN EN ISO 15792-1 with seven layers and three weld beads per layer. A lighter shading indicates the buffered zone.

5.2.2 LOM and EBSD for grain size measurements

The first assignment of this study was to find methods for an efficient and economic characterization of the microstructure of the weld metal. Considering the applied alloying concepts, this involved the characterization of the martensitic matrix, as well as the characterization of presumably occurring precipitates. **Papers I and II** elaborate the results from LOM and EBSD and discuss their suitability for grain size evaluations of the martensitic matrix.

The metallographic samples with the approximate chemical composition stated in table 1 were prepared from the all-weld metal using the standard procedure: embedding → grinding → polishing. Due to its simplicity compared to other methods, light optical microscopy was the first choice for the microstructural characterization. In order to produce a contrast in the LOM, the metallographic samples were etched after polishing. The used etchants and corresponding etching times are shown in table 2 (**Paper II**).

Table 1: Approx. alloying contents in wt.% of the all-weld metal investigated in **Paper II**.

C	Si	Mn	Cr	Mo	Ni	Fe
0.09	0.80	2.5	0.75	0.70	3.0	Rest

Table 2: Suitable etchants for LOM investigations of metallographic samples (**Paper II**).

Name	Composition	Procedure
Nital	3% HNO_3 in ethanol	Etching for 2-3 seconds
Picric acid	100 ml saturated picric acid, 10 ml Xylol, 0.5 ml HCl, a few drops of liquid soap as a wetting agent	Etching for ca. 60 seconds, immersing in hot water before cleaning
LePera	Two parent solutions [153], mixed 1:1	Mixing of parent solutions directly before wetting the surface with ethanol and etching for ca. 30 seconds

In **Paper I**, a micrograph at low magnification after etching with picric acid showed the primary cellular-dendritic solidification structure (figure 11). Consequently, this etchant is useful for a determination of the primary and secondary dendrite spacings. Etching with nital led to an orientation contrast of the prior austenite grain structure at low magnifications (figure 12). However, if the misorientation between two prior austenite grains was unfavorable, the contrast produced by nital etching was too low and they could not be separated. Therefore, etching with nital could only be used as an indicator of the prior austenite grain structure, and was not suitable for a reliable determination of the prior austenite grain size.

Paper II introduced the LePera etchant as an alternative to the previously mentioned etchants. However, apart from the possibility to produce colorful images, the additional information gained from LePera etched samples was limited. At high magnifications, nital etching and LePera etching revealed the martensitic microstructure. Nevertheless, the resolution achievable in the LOM is too low for a precise determination of the martensitic block size. No evidence was found for other microstructural constituents than martensite. This result was already expected because of the short cooling time from 800 °C to 500 °C in approximately 5 seconds.

In summary, LOM with picric acid samples delivered satisfactory results for a determination of the primary and secondary dendritic spacings, but the prior austenite grain structure and the final martensitic structure could not be analyzed precisely. A more powerful characterization technique was needed. Consequently, **Paper II** suggested the use of EBSD. For this method, any deformations introduced into the sample surface by grinding and

polishing needed to be removed prior to the measurement. Therefore, a vibropolishing step was added to the sample preparation process. The setup for EBSD measurements in the SEM chamber is shown in figure 13. The parameters for the EBSD acquisition software can be found in the appended **Paper II**.

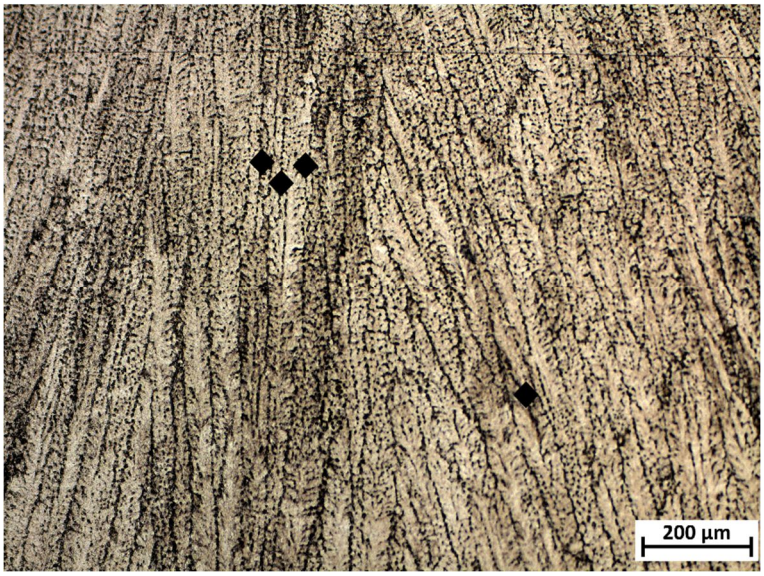

Figure 11: Primary dendritic solidification structure of the all-weld metal etched with picric acid. The indents served as position markers (**Paper I**).

Figure 12: Orientation contrast of the prior austenite grains resulting from nital etching. The same position as in figure 11 is shown for a comparison of the primary dendritic and the columnar austenite grain structure (**Paper I**).

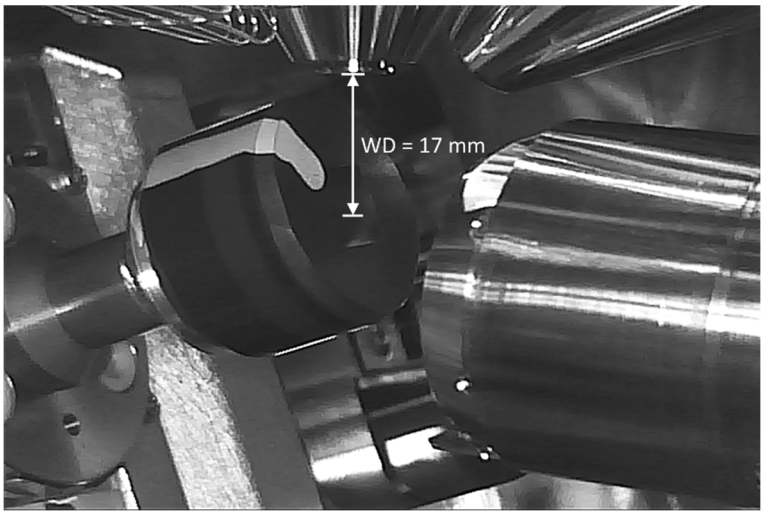

Figure 13: Setup in the SEM chamber for EBSD measurements. The sample was tilted to 70°. The working distance (WD) was set to 17 or 19 mm depending on the space available for the metallographic sample.

The more sophisticated preparation process, the long acquisition time for a measurement and the many microscope hours hence needed may be a disadvantage compared to the LOM, but the high resolution and high amount of information gained from the EBSD measurements were a clear improvement. An evaluation of the EBSD measurements allowed a reliable determination of the martensitic block size. Based on the orientation relationship between martensite and prior austenite, the prior austenite grain structure was reconstructed from the EBSD scans. These reconstructions reflected the prior austenite grain structure much more precisely than the nital etched samples in the LOM. They are consequently more suitable for determining the prior austenite grain size.

Paper II finally concluded with the suggestion, that a combination of LOM and EBSD provides all necessary information for a quantitative analysis of the grain size on all hierarchic microstructural levels. This was demonstrated on a reference sample. All micrographs were taken in the last deposited bead of the all-weld metal sample (figure 14), because in all other locations the microstructure may have been altered by reheating during deposition of subsequent beads. This approach ensures comparability of grain size measurements from different alloys. A more detailed discussion with an exemplary comparison of two alloys can be found in **Paper III**.

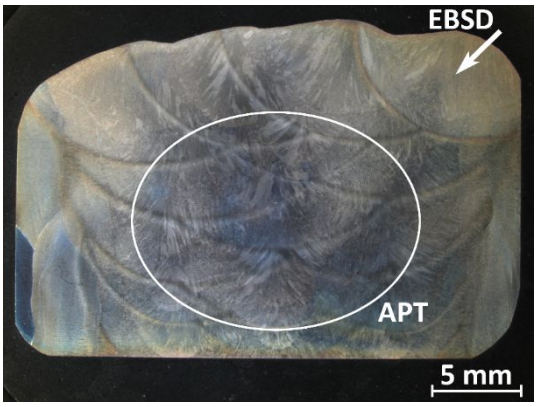

Figure 14: Locations of EBSD and APT measurements (**Paper III**).

5.2.3 APT for precipitate characterization

Although the spatial resolution of EBSD is high enough for depicting the martensitic matrix, it does not suffice for a characterization of nm-sized precipitates. APT with its nearly atomic resolution is suitable for analyzing number density, size and chemical composition of possibly existing precipitates. **Paper III** shows the potential of this method. In random locations of the center area of the all-weld metal sample, a cementite particle and nanoscale segregations of alloying elements were measured. The issue of sample preparation is discussed more extensively in **Paper IV**. The complex multilayer design of the all-weld metal implicates a complex thermal history, which is unique at every position in the cross section. A site-specific preparation of APT samples would only be reasonable in combination with an exhaustive simulation of the thermal history in the prepared position, with additional support by numerous APT measurements for validation. Contrarily, the approach chosen was to randomly prepare 10 APT specimens per alloy from the center area (figure 14) and determine an average size and chemistry of the existing precipitates. Additionally, for **Paper IV** a set of samples was prepared from the last deposited bead, which does not undergo any reheating except the soaking treatment (150 °C for 16 hours). In this set of samples no precipitates were existent, proving the assumption that the precipitates only formed during reheating by subsequent weld beads.

Overall, a combination of LOM and EBSD in the last deposited bead and APT in the reheated centre of the all-weld metal sample was developed and successfully applied to ensure a comprehensive characterization of all important microstructural features. The following section describes, how key alloying elements affect the microstructure and consequently the mechanical properties of the all-weld metal.

5.2.4 Microstructure-property relationships of martensitic all-weld metal

One focus of this doctoral thesis was to understand the influence of the microstructure on the static strength and the impact toughness of the investigated ultra-high strength all-weld metal. The topic was approached by separating the development of an alloying strategy in a strengthening concept and a toughening concept. Most modern literature suggests the use of the microalloying elements Ti and Nb for grain size refinement and consequently toughness improvement. V and Al are commonly used for strengthening of steel by nitride formation. Contrarily (and surprisingly), the addition of Ti and Nb deteriorated the impact toughness of the all-weld metal. Low contents of Al did not show a significant impact on the strength or toughness of the all-weld metal in the investigated content range. These findings were published in the co-authored papers related to this thesis by Schnitzer et al. [154] and Holly et al. [155]. **Paper IV** deals with the strength increase resulting from microalloying additions. In a first group of samples, all four microalloying elements were added and the V content was varied. Table 3 shows the chemical composition and the approximate size of the found precipitates measured with APT. The main conclusions were, that both Ti and V induce clustering in the all-weld metal. The type of precipitates was stated as (Ti,V)(C,N) with MX type stochiometry. Increasing the V content resulted in a V enrichment and a bigger size of the precipitates. Nb and Al did not show any signs of clustering, and did therefore not contribute to the strength increase of these samples. Because of the drastic toughness decrease with increasing microalloy content, it was decided to study a second group of alloys, which were only alloyed with V. The observed clusters were mainly V(C,N) and are exemplarily depicted in figure 15. These clusters significantly strengthened the material with only minor reductions of the impact energy. Consequently, alloying with V was established as the strengthening concept for the all-weld metal. The optimum V content was 0.2 wt.%.

Table 3: Average chemical composition of precipitates in at.% and approximate precipitate size measured from 10 microalloyed samples prepared from random locations (**Paper IV**).

Element	Ti-Nb-Al	Ti-Nb-Al-0.2V	Ti-Nb-Al-0.5V
Ti	**22** ± 10	**15** ± 4	**17** ± 4
Nb	**6** ± 2	**8** ± 4	**7** ± 1
V	-	**18** ± 2	**19** ± 6
N	**7** ± 4	**15** ± 4	**20** ± 4
C	**15** ± 13	**19** ± 4	**17** ± 4
Fe	**40** ± 8	**14** ± 3	**12** ± 4
Precipitate size	1-5 nm	5 nm	10 nm

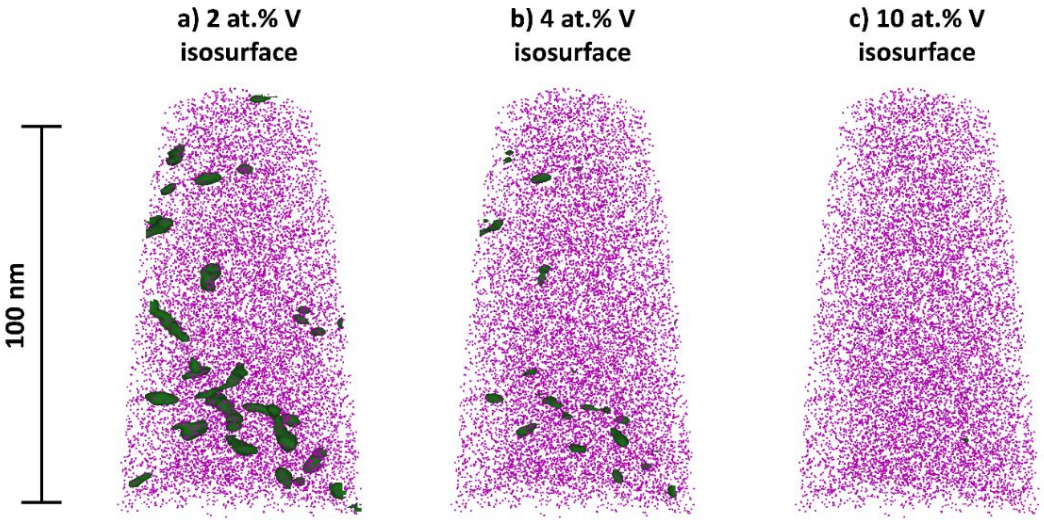

Figure 15: Reconstruction of an APT specimen of a V-alloyed sample. Small V-rich clusters were found (**Paper V**).

Paper V, which summarizes the most important findings of the thesis, shortly elaborates this strengthening concept again, and introduces the developed toughening concept. According to **Paper I** a correlation of the primary dendrite spacings to the impact toughness was not observed. Therefore, the toughening concept of **Paper V** involves the prior austenite grain structure and the final martensitic structure. Four alloys with the compositions stated in table 4 were compared. The toughness of the weld metal was increased by reducing the grain size of the martensitic matrix and by a morphological shift of the martensitic matrix from a mostly parallel arrangement of blocks to a mostly interlocked and chaotic arrangement of blocks (see figure 16). The respective grain sizes were evaluated from EBSD measurements and the corresponding prior austenite grain reconstructions with ARPGE. A reduction of the prior austenite grain size resulted in a smaller effective grain size for crack propagation. This result is consistent with most literature on grain size and toughness in martensitic microstructures [116,121,156,157]. It also shows, that developed concepts for a maximization of the fraction of acicular ferrite by increasing the prior austenite grain size (as described in section 4.2) cannot be applied to martensitic all-weld metal. As a crack will be deflected by high angle grain boundaries, but is able to propagate through low angle grain boundaries, the tolerance angle for the effective grain size was set to 15°. The smaller effective grain size goes hand in hand with a higher average grain boundary misorientation, which is also beneficial for crack deflection. The alloy variations leading to the reduced grain sizes were a lower C, Mn and Si content, represented by the martensite start temperature in figure 17. The reduced grain sizes due to the lower alloy contents resulted in a higher impact toughness compared to the reference sample, which is shown in figure 18.

Table 4: Chemical composition of the investigated alloys in wt.% (**Paper V**).

	C	Si	Mn	P	S	Cr	Mo	Ni	V
Alloy A	0.12	0.81	2.4	0.012	0.009	0.70	0.72	3.19	0
Alloy B	0.08	0.74	2.4	0.009	0.009	0.63	0.73	2.55	0
Alloy C	0.08	0.46	1.1	0.008	0.010	0.73	0.82	3.28	0
Alloy D	0.09	0.52	1.6	0.012	0.009	0.78	0.56	2.92	0.22

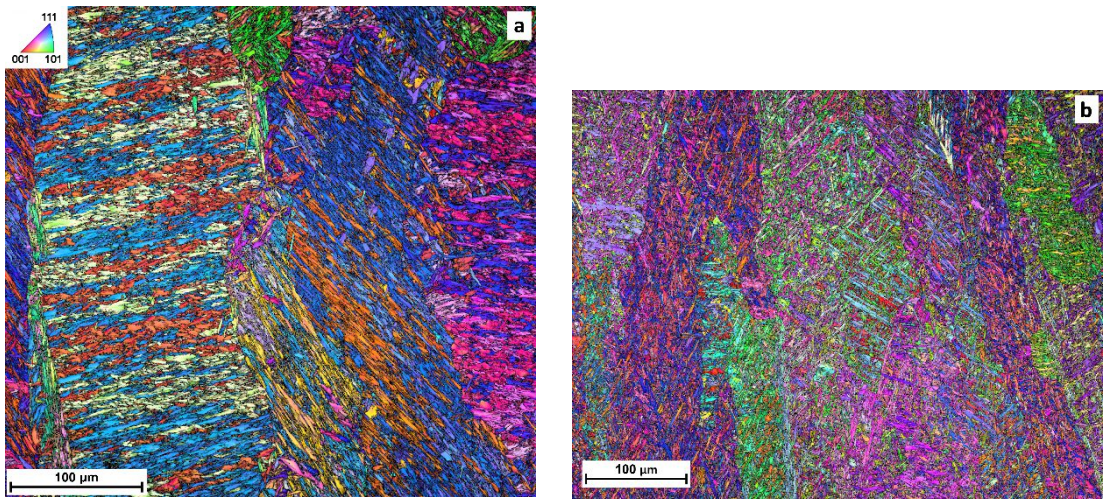

Figure 16: Inverse pole figure + image quality maps of alloys A and C from table 4. A shift from a parallel arrangement of blocks in alloy A (a) to a chaotic, interlocked arrangement of blocks in alloy C (b) is clearly visible (**Paper V**).

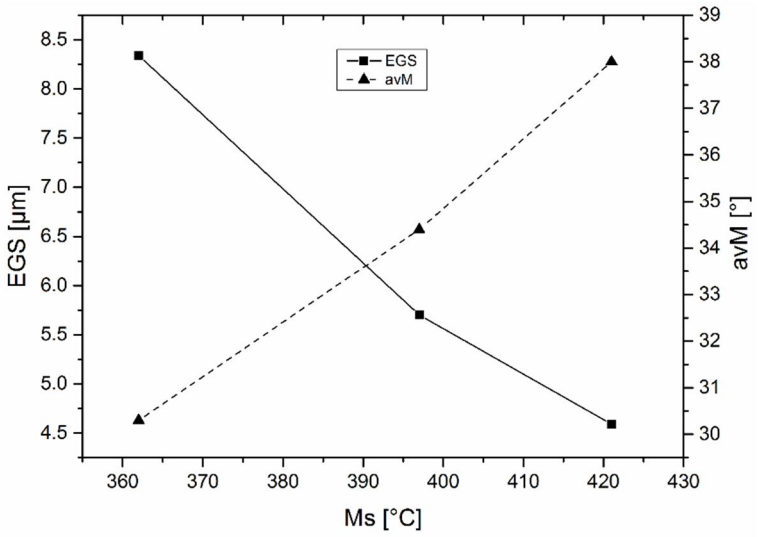

Figure 17: Effective grain size (EGS) and average misorientation (avM) evaluated from EBSD measurements in dependence of the martensite start temperature (**Paper V**).

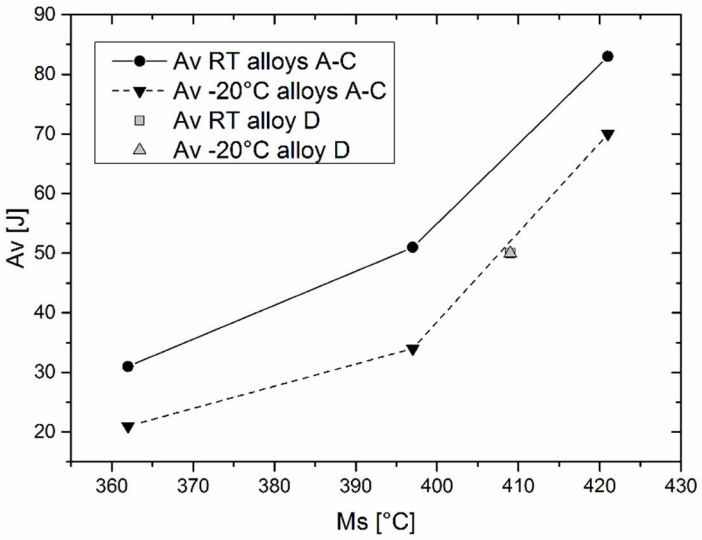

Figure 18: Impact toughness (Av) at room temperature and at -20 °C in dependence of the martensite start temperature (Ms). The values of alloy D are inserted as grey shaded points in the diagram (**Paper V**).

In a final step, the strengthening concept and the toughening concept were combined. Alloying with moderate amounts of V and simultaneously reducing the contents of V, Si and Mn resulted in an all-weld metal sample with a yield strength of over 1100 MPa and a toughness of more than the required 47 J at -20 °C.

5.2.5 Homogeneity of the all-weld metal sample on several length scales

As mentioned earlier, it is essential to describe the measurement location for methods with a high resolution and a small field of view. Figure 14 from **Paper III** indicates the chosen locations for the APT and EBSD measurements, which were selected based on assumptions regarding the time of precipitate formation and for maximum comparability of the EBSD scans of different alloys. This picture of the macro-etched all-weld metal implies the existence of several sources of inhomogeneity in a multipass weld, which inevitably affect the microstructure. **Paper VI** describes observed inhomogeneities in the studied weld metal on several length scales. Apart from the well-known phenomenon, that the macrostructure of multipass welds contains columnar regions and fine-grained regions, segregations of alloying elements to primary dendrite boundaries were measured with an electron microprobe. These microstructural and chemical inhomogeneities induce local fluctuations in the mechanical properties. A hardness mapping (figure 19) revealed fluctuations between 350 and 410 HV. For a comparison of hardness and toughness fluctuations, sub-sized Charpy V-notch samples

were prepared for local impact toughness measurements (figure 20). In the upper part samples a large portion of the notch length was located in the last deposited bead of the all-weld metal. However, despite the existent hardness fluctuations and the corresponding microstructural fluctuations, the sub-sized Charpy V-notch tests showed no significant difference between the impact energy of the upper part and the impact energy of the reheated material. This result indicates that the toughness loss due to the formation of V-rich precipitates is comparable to the toughness gain due to tempering of the martensitic matrix. It also justifies the approach to focus on the martensitic structure of the last bead for the EBSD measurements and the correlation of grain size and toughness.

Although the findings of **Paper VI** support the used approaches for sample preparation and data interpretation, they also show potential for further measurements in order to deepen the understanding of this multipass structure.

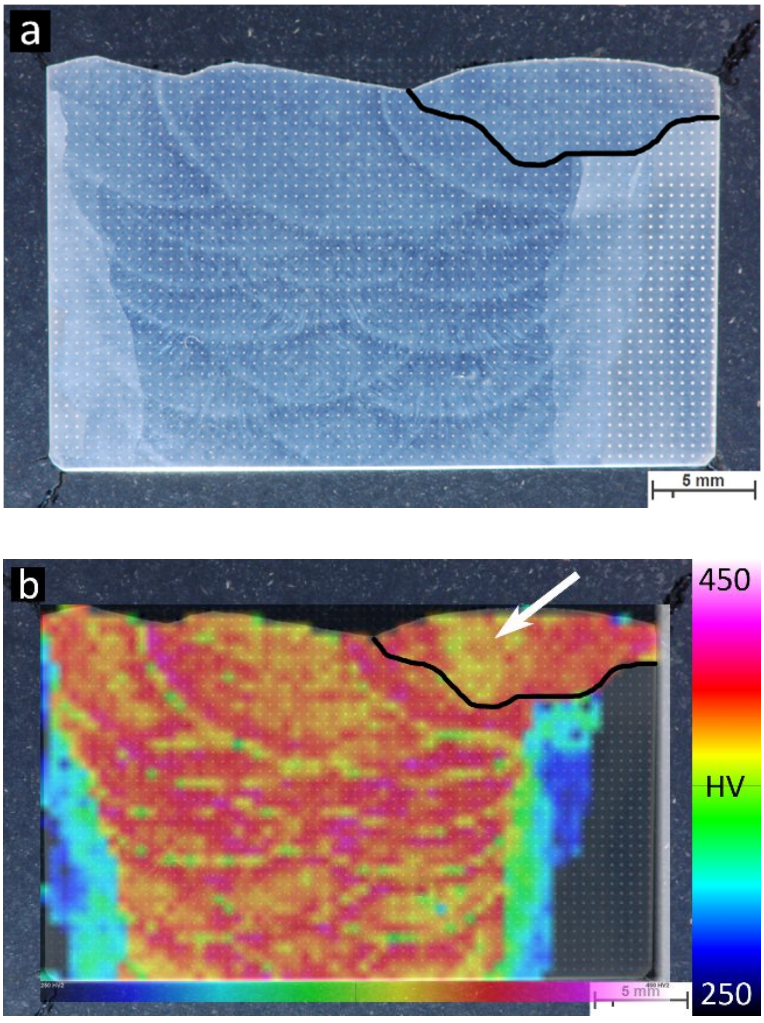

Figure 19: Hardness mapping of a V-alloyed all-weld metal sample. The melting line of the last bead is marked by a black line (**Paper VI**).

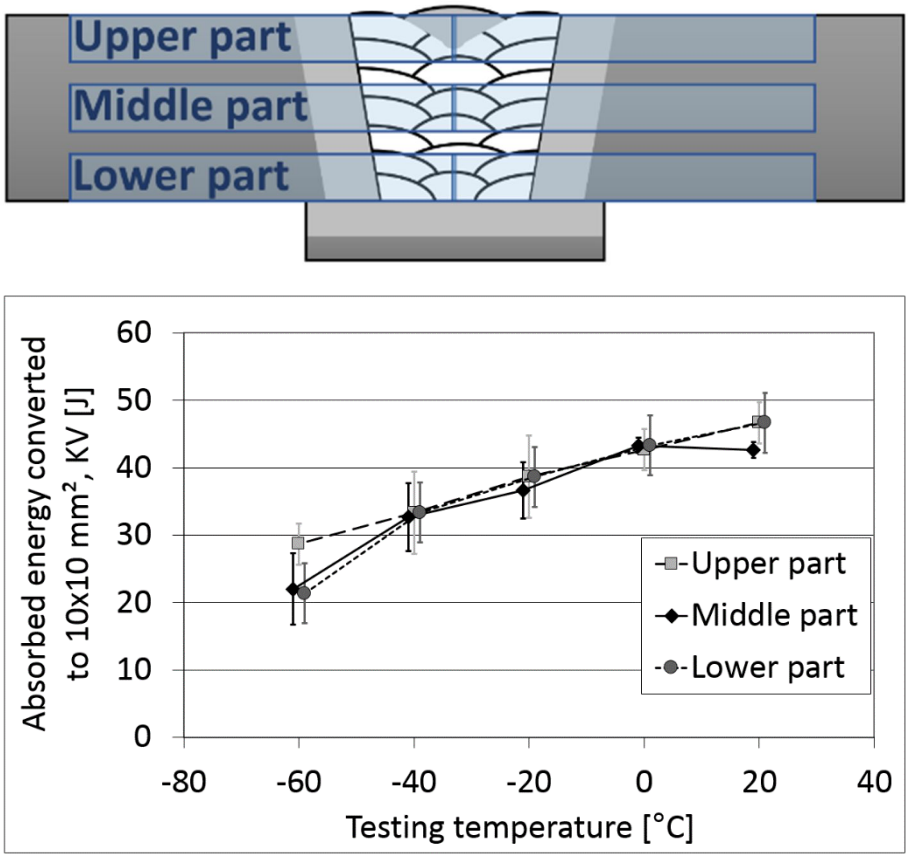

Figure 20: Sub-sized Charpy V-notch samples were prepared for a determination of the local impact energy of the all-weld metal (**Paper VI**).

6 Outlook and open questions

In the course of the project, the goal of producing a filler metal with a minimum yield strength of 1100 MPa and an impact toughness of 47 J at -20 °C was reached. A strengthening and toughening concept was developed and correlated with microstructural changes in the weld metal. An efficient way to characterize all important microstructural features in the martensitic all-weld metal was introduced. However, some interesting topics were not addressed so far, and some questions are still unsolved.

First of all, the limit of 47 J was exceeded by only a few Joules. A sum of several influences and consequent fluctuations can result in a toughness decrease, pushing the impact values below the set limit. Slight variations in the alloying content can occur due to powder mixing variations or variations in the welding process, which will affect the microstructure of the all-weld metal. The investigated temperatures lie in the transition range of the impact energy curve, which may also lead to a more pronounced variation of the measured impact values. Further development efforts and a deeper understanding of microstructural processes are essential to elevate the impact toughness into a save range.

According to the current thesis, a shift from a predominantly parallel arrangement of martensitic blocks to a more chaotic and interlocked arrangement of blocks occurs in dependence of the alloying content. The exact reasons for this shift are not yet identified. A comparability of this interlocked martensite to acicular ferrite can neither be confirmed nor ruled out. Furthermore, the change in prior austenite grain size depending on the alloying content is not fully understood and should definitely be a focus of further investigations, especially because a refined prior austenite grain size is always beneficial for the impact toughness of martensitic steels.

The observed prior austenite grain structure was columnar with a column length of typically several millimeters in regions, where the weld metal was not reaustenized. The fast cooling rate and the directional growth of the austenite crystals may induce a texture in the prior austenite grain structure and the final martensitic microstructure. This texture could influence the measured grain sizes and could also directly influence the measured impact toughness. This topic should be elaborated with EBSD.

One further influence on the impact toughness could be the existence of retained austenite or MA-phase in the weld metal. Currently, Hannah Schönmaier is investigating this topic in her master thesis. If her results show that retained austenite is existent and that there might be a correlation with the mechanical properties, further investigations could severely deepen the understanding of this type of weld metal.

During the project, first attempts were made to study segregations of alloying elements to block boundaries with APT. The segregation of phosphorus and other elements depending on the overall alloy content and the grain size would be another interesting topic. The required site-specific preparation would have to be studied carefully because of the existing inhomogeneities in the weld metal.

One main conclusion of the current thesis was, that V is the most potent microalloying element for strengthening of the weld metal. The other microalloying elements were disregarded due to their more negative influence on the toughness. However, the range of alloying contents and the combinations of different microalloying elements tried were limited. An interesting development direction would be to try all four microalloying elements (Ti, Nb, V and Al) separately and increase the range of content variation. Maybe another microalloying element apart from V evolves as indispensable alloying addition for this 1100 MPa filler wire.

Once the alloying concept was optimized and the static properties of the all-weld metal sample are in a stable and safe regime, issues like the mechanical properties in actual welded joints with different base materials and service properties in various environments can be assessed. The suitability of the filler wire for welding TM-steels and QT-steels with an appropriate strength needs to be checked. The applicability of the filler wire for various modern welding processes with different heat inputs and dilutions should be evaluated. The reaction of the welded material to post weld heat treatments, which may deteriorate the toughness of the weld due to severe vanadium precipitate formation, should also be investigated. Its susceptibility to hydrogen-assisted cold cracking might be of interest as well. Furthermore, the intended applications require a good fatigue performance, which will have to be examined. In this field, the current filler wire will have to compete with the already existing LTT wires.

Overall, the progress of the development of this metal-cored filler wire is promising. Although many microstructural issues were addressed and solved in this thesis and the appended publications, there is still a number of open questions for further research.

7 References

1. Dolby RE (2013) Milestones in welding technology. Philos Mag 93:3863–3877. doi: 10.1080/14786435.2013.793854
2. Rajasekaran R (2015) Welding | MIG Welding | Gas Metal Arc Welding | Metal Inert Gas Welding | GMAW Process. In: Encycl. Eng. http://www.mechscience.com/mig-welding-gas-metal-arc-welding-metal-inert-gas-welding-gmaw-process-3/.
3. Dilthey U (2006) Schweißtechnische Fertigungsverfahren 1 - Schweiß- und Schneidtechnologien. Springer Verlag, Berlin Heidelberg
4. Antonini JM (2014) Comprehensive Materials Processing. Compr Mater Process. doi: 10.1016/B978-0-08-096532-1.00807-4
5. Pal K, Pal SK (2011) Effect of pulse parameters on weld quality in pulsed gas metal arc welding: A review. J Mater Eng Perform 20:918–931. doi: 10.1007/s11665-010-9717-y
6. Bose-Filho WW, Carvalho ALM, Strangwood M (2007) Effects of alloying elements on the microstructure and inclusion formation in HSLA multipass welds. Mater Charact 58:29–39. doi: 10.1016/j.matchar.2006.03.004
7. Grong O, Matlock DK (1986) Microstructural development in mild and low-alloy steel weld metals. Int Met Rev 31:27–48. doi: 10.1179/imtr.1986.31.1.27
8. Keehan E, Karlsson L, Andrén H-O, Bhadeshia H (2006) New Developments with C-Mn-Ni High-Strength Steel Weld Metals, Part A — Microstructure. Weld J 85:200s–210s.
9. Widgery DJ (1976) Deoxidation practice for mild steel weld metal. Weld J 55:57s–68s.
10. Abson DJ, Pargeter RJ (1986) Factors influencing as-deposited strength, microstructure, and toughness of manual metal arc welds suitable for C-Mn steel fabrications. Int Mater Rev 31:141–196. doi: 10.1179/095066086790324302
11. Bhadeshia HKDH, Svensson LE, Gretoft B (1986) The austenite grain structure of low-alloy steel weld deposits. J Mater Sci 21:3947–3951. doi: 10.1007/BF00553451
12. Kluken AO, Grong Ø, Rørvik G (1990) Solidification microstructures and phase transformations in Al-Ti-Si-Mn deoxidized steel weld metals. Metall Trans A 21:2047–2058. doi: 10.1007/BF02647252
13. Zhang Z, Farrar RA (1995) Columnar grain development in C-Mn-Ni low-alloy weld metals and the influence of nickel. J Mater Sci 30:5581–5588. doi: 10.1007/BF00356690
14. Reed RC, Bhadeshia HKDH (1994) A simple model for multipass steel welds. Acta Metall Mater 42:3663–3678. doi: 10.1016/0956-7151(94)90432-4
15. Bhadeshia HKDH, Svensson LE (1989) The microstructure of submerged arc-weld deposits for high-strength steels. J Mater Sci 24:3180–3188. doi: 10.1007/BF01139039
16. Vanovsek W, Bernhard C, Fiedler M, Posch G (2013) Influence of aluminum content on the characterization of microstructure and inclusions in high-strength steel welds. Weld World 57:73–83. doi: 10.1007/s40194-012-0008-0
17. Amrei MM, Monajati H, Thibault D, et al (2016) Microstructure characterization and hardness distribution of 13Cr4Ni multipass weld metal. Mater Charact 111:128–136. doi: 10.1016/j.matchar.2015.11.022
18. Johnson MO, Evans GM, Edwards G (1995) The Influence of Titanium Additions and Interpass Temperature on the Microstructures and Mechanical Properties of High Strength SMA Weld Metals. ISIJ Int 35:1222–1231.
19. Keehan E, Zachrisson J, Karlsson L (2010) Influence of cooling rate on microstructure and properties of high strength steel weld metal. Sci Technol Weld Join 15:233–238. doi: 10.1179/136217110X12665048207692

20. Bajic N, Sijacki-Zeravcic V, Bobic B, et al (2011) Filler Metal Influence on Weld Metal Structure of Microalloyed Steel. Weld J 90:55s–62s.

21. Jiang QL, Li YJ, Wang J, Zhang L (2011) Effects of inclusions on formation of acicular ferrite and propagation of crack in high strength low alloy steel weld metal. Mater Sci Technol 27:1565–1569. doi: 10.1179/026708310X12815992418535

22. Sumi H, Oi K, Yasuda K (2015) Effect of chemical composition on microstructure and mechanical properties of laser weld metal of high-tensile-strength steel. Weld World 59:173–178. doi: 10.1007/s40194-014-0191-2

23. Zhang T, Li Z, Ma S, et al (2016) High strength steel (600–900 MPa) deposited metals: microstructure and mechanical properties. Sci Technol Weld Join 21:186–193. doi: 10.1179/1362171815Y.0000000079

24. Davis C, King J (1993) Effect of cooling rate on intercritically reheated microstructure and toughness in high strength low alloy steel. Mater Sci Technol 9:8–15.

25. Staiger MP, Jessop B, Hodgson PD, et al (1999) Effect of Nitrogen on Formation of Martensite-Austenite in Low Carbon Steels. ISIJ Int 39:183–190.

26. Li Y, Baker TN (2010) Effect of morphology of martensite–austenite phase on fracture of weld heat affected zone in vanadium and niobium microalloyed steels. Mater Sci Technol 26:1029–1040. doi: 10.1179/026708309X12512744154360

27. Akselsen OM, Solberg JK, Grong O (1988) Effects of martensite-austenite (M-A) islands on intercritical heat-affected zone toughness of low carbon microalloyed steels. Scand J Metall 17:194–200.

28. Farrar RA, Harrison PL (1987) Acicular ferrite in carbon-manganese weld metals: An overview. J Mater Sci 22:3812–3820. doi: 10.1007/BF01133327

29. Abson DJ (1989) Non-metallic inclusions in ferritic steel weld metals - a review. Weld World, Le Soudage Dans Le Monde 27:76–101.

30. Sugden A, Bhadeshia H (1989) Lower acicular ferrite. Metall Trans A 20:1811–1818.

31. Babu S, Bhadeshia H (1990) Transition from bainite to acicular ferrite in reheated Fe–Cr–C weld deposits. Mater Sci Technol 6:1005–1020.

32. Zhang Z, Farrar RA (1996) Role of non-metallic inclusions in formation of acicular ferrite in low alloy weld metals. Mater Sci Technol 12:237–260.

33. Jiang QL, Li YJ, Wang J, Zhang L (2011) Effects of Mn and Ti on microstructure and inclusions in weld metal of high strength low alloy steel. Mater Sci Technol 27:1385–1390. doi: 10.1179/026708310X12701149768052

34. Wan XL, Wang HH, Cheng L, Wu KM (2012) The formation mechanisms of interlocked microstructures in low-carbon high-strength steel weld metals. Mater Charact 67:41–51. doi: 10.1016/j.matchar.2012.02.007

35. Seo JS, Lee C, Kim HJ (2013) Influence of Oxygen Content on Microstructure and Inclusion Characteristics of Bainitic Weld Metals. ISIJ Int 53:279–285. doi: 10.2355/isijinternational.53.279

36. Seo JS, Seo K, Kim HJ, Lee C (2014) Effect of titanium content on weld microstructure and mechanical properties of bainitic GMA welds. Weld World 58:893–901. doi: 10.1007/s40194-014-0168-1

37. Loder D, Michelic SK, Mayerhofer A, Bernhard C (2017) On the Capability of Nonmetallic Inclusions to Act as Nuclei for Acicular Ferrite in Different Steel Grades. Metall Mater Trans B Process Metall Mater Process Sci 48:1992–2006. doi: 10.1007/s11663-017-0984-y

38. Evans GM (1995) Microstructure and properties of ferritic steel welds containing Al and Ti. Weld J 74:249s–261s.

39. Vanovsek W, Bernhard C, Fiedler M, Schnitzer R (2013) Effect of titanium on the solidification and postsolidification microstructure of high-strength steel welds. Weld World 57:665–674. doi: 10.1007/s40194-013-0063-1

40. Babu SS, Bhadeshia HKDH (1991) Mechanism for the Transition from Bainite to Acicular Ferrite. Mater Trans 32:679–688.

41. Ricks RA, Howell PR, Barritte GS (1982) The nature of acicular ferrite in HSLA steel weld metals. J Mater Sci 17:732–740. doi: 10.1007/BF00540369

42. Bhadeshia HKDH (2001) Bainite in steels, 3rd ed. Institute of Materials, Cambridge

43. Aaronson HI, Wells C (1956) Sympathetic nucleation of ferrite. Trans AIME 206:1216–1223.

44. Wu KM, Inagawa Y, Enomoto M (2004) Three-dimensional morphology of ferrite formed in association with inclusions in low-carbon steel. Mater Charact 52:121–127. doi: 10.1016/j.matchar.2004.04.004

45. Nishiyama Z (1978) Martensitic Transformation. Academic Press Inc., London

46. Kurdjumov G, Sachs G (1930) Over the mechanisms of steel hardening. Z Phys 64:325–343.

47. Gourgues A-F, Flower HM, Lindley TC (2000) Electron backscattering diffraction study of acicular ferrite, bainite, and martensite steel microstructures. Mater Sci Technol 16:26–40. doi: 10.1179/026708300773002636

48. Gourgues A-F (2002) Electron Backscatter Diffraction and Cracking. Mater Sci Technol 18:119–133.

49. Seo JS, Kim HJ, Lee C (2013) Effect of Ti Addition on Weld Microstructure and Inclusion Characteristics of Bainitic GMA Welds. ISIJ Int 53:880–886. doi: 10.2355/isijinternational.53.880

50. Beidokhti B, Kokabi a. H, Dolati a. (2014) A comprehensive study on the microstructure of high strength low alloy pipeline welds. J Alloys Compd 597:142–147. doi: 10.1016/j.jallcom.2014.01.212

51. Chang LC, Bhadeshia HKDH (1996) Microstructure of lower bainite formed at large undercoolings below bainite start temperature. Mater Sci Technol 12:233–236. doi: 10.1179/mst.1996.12.3.233

52. Keehan E, Karlsson L, Bhadeshia HKDH, Thuvander M (2008) Electron backscattering diffraction study of coalesced bainite in high strength steel weld metals. Mater Sci Technol 24:1183–1188. doi: 10.1179/174328407X226572

53. Keehan E, Karlsson L, Bhadeshia HKDH, Thuvander M (2008) Three-dimensional analysis of coalesced bainite using focused ion beam tomography. Mater Charact 59:877–882. doi: 10.1016/j.matchar.2007.07.011

54. Keehan E, Karlsson L, Andrén H-O, Bhadeshia HKDH (2006) Influence of carbon, manganese and nickel on microstructure and properties of strong steel weld metals, Part 2 - Impact toughness gain resulting from manganese reductions. Sci Technol Weld Join 11:9–18.

55. Keehan E, Karlsson L, Andrén H-O (2006) Influence of carbon, manganese and nickel on microstructure and properties of strong steel weld metals, Part 1 - Effect of nickel content. Sci Technol Weld Join 11:1–8.

56. Wansheng D, Yun P, Hongjun X, et al (2010) Microstructure and Toughness of 1000 MPa High Strength Weld Metal. Mater Sci Forum 638–642:3441–3446.

57. Hrivnak I, Matsuda F, Li Z, et al (1992) Investigation of Metallography and Behaviour of Ma Constituent in Weld HAZ of HSLA Steel. Trans JWRI 21:241–250.

58. Jorge JC., Souza LF., Rebello JM. (2001) The effect of chromium on the microstructure/toughness relationship of C–Mn weld metal deposits. Mater Charact 47:195–205. doi: 10.1016/S1044-5803(01)00168-1

59. Mintz B (1997) The influence of martensite on the strength and impact behavior of steel. Metall Mater Trans A 28:2073–2084. doi: 10.1007/s11661-997-0164-9

60. Francis JA, Stone HJ, Kundu S, et al (2009) The Effects of Filler Metal Transformation Temperature on Residual Stresses in a High Strength Steel Weld. J Press Vessel Technol 131:41401. doi: 10.1115/1.3122036

61. Ooi SW, Garnham JE, Ramjaun TI (2014) Review: Low transformation temperature weld filler for tensile residual stress reduction. Mater Des 56:773–781. doi: 10.1016/j.matdes.2013.11.050

62. Dixneit J, Kromm A, Hannemann A, et al (2016) In-situ load analysis in multi-run welding using LTT filler materials. Weld World 60:1159–1168. doi: 10.1007/s40194-016-0373-1

63. Feng Z-Y, Di X-J, Wu S-P, et al (2017) Comparison of two types of low-transformation-temperature weld metals based on solidification mode. Sci Technol Weld Join 1718:1–8. doi: 10.1080/13621718.2017.1376792

64. Harati E, Karlsson L, Svensson LE, Dalaei K (2017) Applicability of low transformation temperature welding consumables to increase fatigue strength of welded high strength steels. Int J Fatigue 97:39–47. doi: 10.1016/j.ijfatigue.2016.12.007

65. Graville BA (1976) Cold cracking in welds in HSLA steels. In: Weld. HSLA Struct. steels. American Society for Metals, pp 85–101

66. Evans GM (1986) Effects of silicon on the microstructure and properties of C-Mn all-weld-metal deposits. Met Constr 18:438r–444r.

67. Isheim D, Kolli RP, Fine ME, Seidman DN (2006) An atom-probe tomographic study of the temporal evolution of the nanostructure of Fe-Cu based high-strength low-carbon steels. Scr Mater 55:35–40. doi: 10.1016/j.scriptamat.2006.02.040

68. Ramirez JE, Liu S, Olson DL (1996) Dual precipitation strengthening effect of copper and niobium in high strength steel weld metal. Mater Sci Eng A 216:91–103. doi: 10.1016/0921-5093(96)10398-1

69. Avazkonandeh-Gharavol MH, Haddad-Sabzevar M, Haerian A (2009) Effect of copper content on the microstructure and mechanical properties of multipass MMA, low alloy steel weld metal deposits. Mater Des 30:1902–1912. doi: 10.1016/j.matdes.2008.09.023

70. Wang H, Yu X, Isheim D, et al (2013) High strength weld metal design through nanoscale copper precipitation. Mater Des 50:962–967. doi: 10.1016/j.matdes.2013.03.093

71. Wang HH, Tong Z, Hou TP, et al (2017) Effects of evolution of nanoscale copper precipitation and copper content on mechanical properties of high-strength steel weld metal. Sci Technol Weld Join 22:191–197. doi: 10.1080/13621718.2016.1213583

72. Surian E, Ramini de Rissone M, De Vedia L (2005) Influence of Molybdenum on Ferritic High- Strength SMAW All-Weld-Metal Properties. Weld J 84:53–62.

73. Schulze G (2010) Die Metallurgie des Schweißens. Springer Verlag, Berlin Heidelberg

74. Gladman T (1997) The physical metallurgy of microalloyed steels. The Institute of Materials, London

75. Lagneborg R, Siwecki T, Zajac S, Hutchinson B (1999) The Role Of Vanadium In Microalloyed Steels. Scand. J. Metall.

76. Medina SF, Chapa M, Valles P, et al (1999) Influence of Ti and N Contents on Austenite Grain Control and Precipitate Size in Structural Steels. ISIJ Int 39:930–936.

77. Sasaki M, Ohsasa K, Kudoh M, Matsuura K (2008) Refinement of Austenite Grain in Carbon Steel by Addition of Titanium and Boron. ISIJ 48:340–343.

78. Sasaki M, Matsuura K, Ohsasa K, Ohno M (2009) Effects of Addition of Titanium and Boron on Columnar Austenite Grain in Carbon Steel. ISIJ Int 49:1367–1371. doi: 10.2355/isijinternational.49.1367

79. Nöhrer M (2013) Precipitation behavior of different micro-alloyed 0.2 wt% C steels. Montanuniversität Leoben

80. Perez M, Courtois E, Acevedo D, et al (2007) Precipitation of niobium carbonitrides in ferrite: chemical composition measurements and thermodynamic modelling. Philos Mag Lett 87:645–656. doi: 10.1080/09500830701427003

81. Bäcke L (2010) Modeling the Effect of Solute Drag on Recovery and Recrystallization during Hot Deformation of Nb Microalloyed Steels. ISIJ Int 50:239–247. doi: 10.2355/isijinternational.50.239

82. Radis R, Kozeschnik E (2012) Numerical simulation of NbC precipitation in microalloyed steel. Model Simul Mater Sci Eng 20:55010. doi: 10.1088/0965-0393/20/5/055010

83. Batte AD, Honeycombe RWK (1973) Precipitation of vanadium carbide in ferrite. J Iron Steel Inst 284–289.

84. Baker TN (2009) Processes, microstructure and properties of vanadium microalloyed steels. Mater Sci Technol 25:1083–1107. doi: 10.1179/174328409X453253

85. Nöhrer M, Zamberger S, Primig S, Leitner H (2013) Atom probe study of vanadium interphase precipitates and randomly distributed vanadium precipitates in ferrite. Micron 54–55:57–64. doi: 10.1016/j.micron.2013.08.008

86. Yen H-W, Chen P-Y, Huang C-Y, Yang J-R (2011) Interphase precipitation of nanometer-sized carbides in a titanium–molybdenum-bearing low-carbon steel. Acta Mater 59:6264–6274. doi: 10.1016/j.actamat.2011.06.037

87. Dolby RE (1983) Advances in welding metallurgy of steel. Met Technol 10:349–362. doi: 10.1179/030716983803291172

88. He K, Edmonds D V. (2002) Formation of acicular ferrite and influence of vanadium alloying. Mater Sci Technol 18:289–296. doi: 10.1179/026708301225000743

89. Trindade VB, Mello RST, Payao JC, Paranhos RPR (2006) Influence of Zirconium on Microstructure and Toughness of Low-Alloyed Steel Weld Metals. J Mater Eng Perform 15:284–286.

90. Narayanan BK, Kovarik L, Sarosi PM, et al (2010) Effect of microalloying on precipitate evolution in ferritic welds and implications for toughness. Acta Mater 58:781–791. doi: 10.1016/j.actamat.2009.09.056

91. Gerlich AP, Izadi H, Bundy J, Mendez PF (2014) Characterization of High-Strength Weld Metal Containing Mg-Bearing Inclusions. Weld J 93:15–22.

92. Petzow G (1999) Metallographic Etching, 2nd ed. ASM International, Materials Park, Ohio

93. Powell GLF, Herfurth G (1998) Charpy V-notch properties and microstructures of narrow gap ferritic welds of a quenched and tempered steel plate. Metall Mater Trans A Phys Metall Mater Sci 29:2775–2784. doi: 10.1007/s11661-998-0318-4

94. Aguiar IV, Escobar DP, Santos DB, Modenesi PJ (2015) Microstructure characterization of a duplex stainless steel weld by electron backscattering diffraction and orientation imaging microscopy techniques. Rev Mater 20:212–226.

95. López-Martínez E, Vázquez-Gómez O, Vergara-Hernández HJ, et al (2016) Mechanical characterization of the welding of two experimental HSLA steels by microhardness and nanoindentation tests. Met Mater Int 22:987–994. doi: 10.1007/s12540-016-6271-7

96. Baumgartner S, Posch G, Mayr P (2013) Welding Advanced Martensitic Creep-Resistant Steels With Boron Containing Filler Metal. Weld World 56:2–9. doi: 10.1007/BF03321359

97. Stoschka M, Leitner M, Fössl T, Posch G (2013) Effect of High-Strength Filler Metals on Fatigue. Weld World 56:20–29. doi: 10.1007/BF03321332

98. Seo K, Kim Y, Kim HJ, Lee C (2015) IIW Document IX-L-1143-15: Quantitative Evaluation of Nucleation Potency of Ti-containing Inclusions for Acicular Ferrite. Int. Inst. Weld.

99. Vitek JM, Babu SS (2011) Multiscale characterisation of weldments. Sci Technol Weld Join 16:3–11. doi: 10.1179/1362171810Y.0000000003

100. Stoschka M, Leitner M, Posch G, Eichlseder W (2012) Effect of high-strength filler metals on the fatigue behaviour of butt joints. Weld World 57:85–96. doi: 10.1007/s40194-012-0010-6

101. Yongyuth P, Ghosh PK, Gupta PC, et al (1992) Influence of Macro/Microstructure on the Toughness of “All Weld” Multipass Submerged Arc Welded C-Mn Steel Deposits. ISIJ Int 32:771–778.

102. Mythili R, Thomas Paul V, Saroja S, et al (2003) Microstructural modification due to reheating in multipass manual metal arc welds of 9Cr-1Mo steel. J Nucl Mater 312:199–206. doi: 10.1016/S0022-3115(02)01680-X

103. Kikuta Y, Araki T, Yoneda M, et al (1982) The Reheated Zone Toughness of Multipass Weld Metal (Report 1). J Japan Weld Soc 51:359–365. doi: 10.2207/qjjws1943.51.359

104. Thewlis G (1994) Transformation kinetics of ferrous weld metals. Mater Sci Technol 10:110–125. doi: 10.1179/mst.1994.10.2.110

105. Evans GM (1998) Effect of Nitrogen on C-Mn Steel Welds Containing Titanium and Boron. Weld J 77:239–248.

106. Pargeter RJ, Dolby RE (1986) Guidelines for the classification of ferritic steel weld metal and microstructural constituents using the light microscope. Weld World, Le Soudage Dans Le Monde 24:144–149.

107. Thewlis G (2004) Classification and quantification of microstructures in steels. Mater Sci Technol 20:143–160. doi: 10.1179/026708304225010325

108. Banaschik R, Brätz O, Henkel K-M (2017) Systematic Expansion of the Microstructural Characterization of Ferritic Weld Metals. Pract Metallogr 54:669–684. doi: 10.3139/147.110466

109. Humphreys FJ (2001) Grain and subgrain characterisation by electron backscatter diffraction. J Mater Sci 36:3833–3854. doi: 10.1023/A:1017973432592

110. Schwartz AJ, Kumar M, Adams BL, Field DP (2009) Electron Backscatter Diffraction in Materials Science, 2nd ed. doi: 10.1007/978-0-387-88136-2

111. Stojakovic D (2012) Electron backscatter diffraction in materials characterization. Process Appl Ceram 6:1–13.

112. Wilkinson AJ, Britton TB (2015) Strains, planes, and EBSD in materials science. Mater Today 15:366–376.

113. Ryde L (2006) Application of EBSD to analysis of microstructures in commercial steels. Mater Sci Technol 22:1297–1306. doi: 10.1179/174328406X130948

114. Morito S, Tanaka H, Konishi R, et al (2003) The morphology and crystallography of lath martensite in Fe-C alloys. Acta Mater 51:1789–1799. doi: 10.1016/j.actamat.2006.07.009

115. Morito S, Huang X, Furuhara T, et al (2006) The morphology and crystallography of lath martensite in alloy steels. Acta Mater 54:5323–5331. doi: 10.1016/j.actamat.2006.07.009

116. Morito S, Yoshida H, Maki T, Huang X (2006) Effect of block size on the strength of lath martensite in low carbon steels. Mater Sci Eng A 438–440:237–240. doi: 10.1016/j.msea.2005.12.048

117. Furuhara T, Kawata H, Morito S, Maki T (2006) Crystallography of upper bainite in Fe–Ni–C alloys. Mater Sci Eng A 431:228–236. doi: 10.1016/j.msea.2006.06.032

118. Morito S, Adachi Y, Ohba T (2009) Morphology and Crystallography of Sub-Blocks in Ultra-Low Carbon Lath Martensite Steel. Mater Trans 50:1919–1923. doi: 10.2320/matertrans.MRA2008409

119. Shibata A, Nagoshi T, Sone M, et al (2010) Evaluation of the block boundary and sub-block boundary strengths of ferrous lath martensite using a micro-bending test. Mater Sci Eng A 527:7538–7544. doi: 10.1016/j.msea.2010.08.026

120. Ungár T, Harjo S, Kawasaki T, et al (2017) Composite Behavior of Lath Martensite Steels Induced by Plastic Strain, a New Paradigm for the Elastic-Plastic Response of Martensitic Steels. Metall Mater Trans A 48:159–167. doi: 10.1007/s11661-016-3845-4

121. Galindo-Nava EI, Rivera-Díaz-del-Castillo PEJ (2015) A model for the microstructure behaviour and strength evolution in lath martensite. Acta Mater 98:81–93. doi: 10.1016/j.actamat.2015.07.018

122. Greninger AB, Troiano AR (1949) The mechanism of martensite formation. Trans AIME 185:590–598.

123. Miyamoto G, Takayama N, Furuhara T (2009) Accurate measurement of the orientation relationship of lath martensite and bainite by electron backscatter diffraction analysis. Scr Mater 60:1113–1116. doi: 10.1016/j.scriptamat.2009.02.053

124. Bernier N, Bracke L, Malet L, Godet S (2014) An alternative to the crystallographic reconstruction of austenite in steels. Mater Charact 89:23–32. doi: 10.1016/j.matchar.2013.12.014

125. Gomes E, Kestens LAI (2015) Fully automated orientation relationship calculation and prior austenite reconstruction by random walk clustering. IOP Conf Ser Mater Sci Eng 82:12059. doi: 10.1088/1757-899X/82/1/012059

126. Abbasi M, Wei L, Nelson TW (2009) Prior Austenite reconstruction in Friction Stir Processe d API X65 Steel using OIM TM. Mater. Sci. Technol. 09

127. Abbasi M, Nelson TW, Sorensen CD, Wei L (2012) An approach to prior austenite reconstruction. Mater Charact 66:1–8. doi: 10.1016/j.matchar.2012.01.010

128. Abbasi M, Kim DI, Nelson TW, Abbasi M (2014) EBSD and reconstruction of pre-transformation microstructures, examples and complexities in steels. Mater Charact 95:219–231. doi: 10.1016/j.matchar.2014.06.023

129. Germain L, Gey N, Mercier R, et al (2012) An advanced approach to reconstructing parent orientation maps in the case of approximate orientation relations: Application to steels. Acta Mater 60:4551–4562. doi: 10.1016/j.actamat.2012.04.034

130. Cayron C, Artaud B, Briottet L (2006) Reconstruction of parent grains from EBSD data. Mater Charact 57:386–401. doi: 10.1016/j.matchar.2006.03.008

131. Cayron C (2007) ARPGE: A computer program to automatically reconstruct the parent grains from electron backscatter diffraction data. J Appl Crystallogr 40:1183–1188. doi: 10.1107/S0021889807048777

132. Cayron C (2007) GenOVa: A computer program to generate orientational variants. J Appl Crystallogr 40:1179–1182. doi: 10.1107/S0021889807048741

133. Cayron C (2014) EBSD imaging of orientation relationships and variant groupings in different martensitic alloys and Widmanstätten iron meteorites. Mater Charact 94:93–110. doi: 10.1016/j.matchar.2014.05.015

134. Cerezo A, Godfrey TJ, Smith GDW (1988) Application of a position-sensitive detector to atom probe microanalysis. Rev Sci Instrum 59:862–866. doi: 10.1063/1.1139794

135. Miller MK, Forbes RG (2014) Atom-Probe Tomography: The Local Electrode Atom Probe. doi: 10.1007/978-1-4899-7430-3

136. Kelly TF, Miller MK (2007) Invited review article: Atom probe tomography. Rev Sci Instrum 78:1–20. doi: 10.1063/1.2709758

137. Miller MK, Forbes RG (2009) Atom probe tomography. Mater Charact 60:461–469. doi: 10.1016/j.matchar.2009.02.007

138. Larson DJ, Prosa TJ, Ulfig RM, et al (2013) Local Electrode Atom Probe Tomography - A User's Guide. Springer Science+Business Media, New York

139. Marquis EA, Hyde JM (2010) Applications of atom-probe tomography to the characterisation of solute behaviours. Mater Sci Eng R Reports 69:37–62. doi: 10.1016/j.mser.2010.05.001

140. Murayama M, Hono K (1999) Pre-precipitate clusters and precipitation processes in Al-Mg-Si alloys. Acta Mater 47:1537–1548. doi: 10.1016/S1359-6454(99)00033-6

141. Miller MK, Pareige P, Burke MG (2000) Understanding pressure vessel steels: an atom probe perspective. Mater Charact 44:235–254. doi: 10.1016/S1044-5803(99)00056-X

142. Kapoor M, O'Malley R, Thompson GB (2016) Atom Probe Tomography Study of Multi-microalloyed Carbide and Carbo-Nitride Precipitates and the Precipitation Sequence in Nb-Ti HSLA Steels. Metall Mater Trans A Phys Metall Mater Sci 47:1984–1995. doi: 10.1007/s11661-016-3398-6

143. Enloe CM, Findley KO, Parish CM, et al (2013) Compositional evolution of microalloy carbonitrides in a Mo-bearing microalloyed steel. Scr Mater 68:55–58. doi: 10.1016/j.scriptamat.2012.09.027

144. Xie KY, Zheng T, Cairney JM, et al (2012) Strengthening from Nb-rich clusters in a Nb-microalloyed steel. Scr Mater 66:710–713. doi: 10.1016/j.scriptamat.2012.01.029

145. Craven AJ, MacKenzie M, Cerezo A, et al (2008) Spectrum imaging and three-dimensional atom probe studies of fine particles in a vanadium micro-alloyed steel. Mater Sci Technol 24:641–650. doi: 10.1179/174328408X270347

146. Babu SS, David SA, Vitek JM, Miller MK (1995) Atom probe field ion microscopy of type 308 CRE stainless steel welds. Appl Surf Sci 87–88:207–215. doi: 10.1016/0169-4332(94)00495-1

147. Andrén H-O, Cai G, Svensson L-E (1995) Microstructure of heat resistant chromium steel weld metals. Appl Surf Sci 87–88:200–206. doi: 10.1016/0169-4332(94)00491-9

148. Pareige P, Radiguet B, Suvorov a., et al (2004) Three-dimensional atom probe study of irradiated, annealed and re-irradiated VVER 440 weld metals. Surf Interface Anal 36:581–584. doi: 10.1002/sia.1705

149. Miller MK, Russell KF (2007) Embrittlement of RPV steels: An atom probe tomography perspective. J Nucl Mater 371:145–160. doi: 10.1016/j.jnucmat.2007.05.003

150. Edmondson PD, Miller MK, Powers KA, Nanstad RK (2016) Atom probe tomography characterization of neutron irradiated surveillance samples from the R. E. Ginna reactor pressure vessel. J Nucl Mater 470:147–154. doi: 10.1016/j.jnucmat.2015.12.038

151. Svoboda J, Fischer FD, Fratzl P, Kozeschnik E (2004) Modelling of kinetics in multi-component multi-phase systems with spherical precipitates I: Theory. Mater Sci Eng A 385:166–174. doi: 10.1016/j.msea.2004.06.018

152. Kozeschnik E, Svoboda J, Fratzl P, Fischer FD (2004) Modelling of kinetics in multi-component multi-phase systems with spherical precipitates II: Numerical solution and application. Mater Sci Eng A 385:157–165. doi: 10.1016/j.msea.2004.06.016

153. LePera FS (1980) Improved Etching Technique to Emphasize Martensite and Bainite in High-Strength Dual-Phase Steel. JOM 32:38–39. doi: 10.1007/BF03354553

154. Schnitzer R, Zügner D, Haslberger P, et al (2017) Influence of alloying elements on the mechanical properties of high-strength weld metal. Sci Technol Weld Join 22:536–543. doi: 10.1080/13621718.2016.1274095

155. Holly S, Haslberger P, Zügner D, et al (2018) Development of high-strength welding consumables using calculations and microstructural characterization. Accepted for Publication in Weld World.

156. Mine Y, Hirashita K, Takashima H, et al (2013) Micro-tension behaviour of lath martensite structures of carbon steel. Mater Sci Eng A 560:535–544. doi: 10.1016/j.msea.2012.09.099

157. Kim M-C, Jun Oh Y, Hwa Hong J (2000) Characterization of boundaries and determination of effective grain size in Mn-Mo-Ni low alloy steel from the view of misorientation. Scr Mater 43:205–211. doi: 10.1016/S1359-6462(00)00392-4

Part B

Paper I

Haslberger P, Ernst W, Schnitzer R (2016)

Mikrostrukturielle Charakterisierung von ultra-hochfesten Schweißgütern

Berg- und Hüttenmännische Monatshefte 61: 321-324

DOI: 10.1007/s00501-016-0494-2

Mikrostrukturielle Charakterisierung von ultra-hochfesten Schweißgütern

Phillip Haslberger[a], Wolfgang Ernst[b], Ronald Schnitzer[a,c]

[a] Department Metallkunde und Werkstoffprüfung, Montanuniversität Leoben, Österreich

[b] voestalpine Stahl Linz GmbH, Österreich

[c] voestalpine Böhler Welding Austria GmbH, Kapfenberg, Österreich

Kurzfassung

Hochfeste Schweißkonstruktionen sind entscheidend für die Realisierung von Leichtbaukonstruktionen für verschiedenste Industriesegmente. Unterschiedliche Methoden wurden verwendet, um die Mikrostruktur von ultra-hochfesten Schweißgütern mit unterschiedlicher chemischer Zusammensetzung zu charakterisieren. Dadurch sollte es möglich sein, die Korngröße mit der Zähigkeit zu korrelieren.

Abstract

(English title: Microstructural characterization of ultra-high strength all-weld metal)

Welded steel structures are a crucial part of lightweight constructions in several industrial segments. The filler metal plays a vital role in optimizing the properties of welded joints. In this study different methods were used to characterize the microstructure of ultra-high strength all-weld metal samples with different chemical compositions. It was evaluated which method can be used to link the grain size of a sample to its toughness.

1 Einleitung

In der Stahl verarbeitenden Industrie besteht ein ständiger Bedarf an Schweißkonstruktionen mit reduziertem Gewicht bei zumindest gleichbleibender Tragfähigkeit. Je nach Schweißverfahren spielt auch der Schweißzusatz eine entscheidende Rolle bei der Bestimmung der mechanischen Eigenschaften des geschweißten Bauteils. Eine nachträgliche Wärmebehandlung des Schweißguts ist dabei oft aus Kostengründen unerwünscht. Besonders das auf den Grundwerkstoff abgestimmte Legierungskonzept des Schweißzusatzes soll deswegen dazu beitragen, ein optimales Verhältnis von Festigkeit und Zähigkeit einzustellen [1].

Für hochfeste, thermomechanisch behandelte oder vergütete Bleche wird zurzeit ein martensitisch erstarrender Schweißzusatz mit einer Festigkeit > 1100 MPa entwickelt. Eine tiefgehende mikrostrukturielle Charakterisierung des Schweißguts ist dabei unerlässlich, um die Beziehung zwischen Mikrostruktur und Eigenschaften zu verstehen. Neben der klassischen Lichtmikroskopie sind hier auch Methoden mit höherer Auflösung wie Raster-Elektronenmikroskopie (REM) oder Elektronen-Rückstreubeugung (= „Electron Backscatter Diffraction“, kurz: EBSD) hilfreich.

Vor allem die Anwendung von EBSD vertiefte das Verständnis des mikrostrukturiellen Aufbaus von Martensit [2–7]. Es wurde festgestellt, dass ein Austenitkorn in sog. „packets“ unterteilt werden kann, das wiederum in „blocks“ unterteilt wird. Diese „blocks“ enthalten mehrere einzelne Martensitlatten mit geringer kristallographischer Missorientierung.

Viele martensitische Stähle wurden in dieser Hinsicht ausführlich untersucht, es gibt aber wenig Literatur zur Charakterisierung von martensitischem Schweißgut. W. Vanovsek lieferte hier Ansätze, die primäre dendritische Struktur mithilfe einer Pikrinsäure-Ätzung sichtbar zu machen und die ehemaligen Austenitkörner nach einer Nital-Ätzung auszuwerten [8,9].

Im Rahmen dieser Arbeit soll weiterführend untersucht werden, welche Methoden eine optimale Charakterisierung der vorliegenden Mikrostruktur in martensitischem Schweißgut ermöglichen.

2 Experimentelle Durchführung

Für die Versuche wurden Proben aus reinem Schweißgut mit unterschiedlichen Legierungsgehalten verwendet. Diese wurden durch MAG-Schweißen mit Vergütungslagen-Aufbau hergestellt. Abb. 1 zeigt den Querschliff einer solchen Probe im geätzten Zustand. Alle mikrostrukturiellen Untersuchungen wurden in der zuletzt aufgetragenen Schweißlage gemacht, um Effekte durch die Wärmeeinbringung von danach aufgebrachten Schweißlagen ausschließen zu können. Für die Lichtmikroskopie wurden die metallographischen Schliffe mit Diamantsuspension poliert und gemäß Tab. 1 geätzt [10]. Für die EBSD Messungen wurden die Schliffe nach den herkömmlichen Polierschritten zusätzlich zwei Stunden in OPS-Suspension vibropoliert. Die bei den Messungen verwendeten Parameter sind in Tab. 2 zusammengefasst. Bei der Auswertung wurden „inverse pole figure maps“ erstellt mit zusätzlicher Anzeige der Bildqualität. Eine ausführliche Erklärung der angewendeten Charakterisierungsmethode EBSD kann in [11] nachgelesen werden.

Es wurde versucht, Ergebnisse aus den Untersuchungen der Mikrostruktur mit der Kerschlagarbeit der Proben zu korrelieren. Für die Kerbschlagbiegeversuche wurden Proben mit V-Kerbe nach Norm DIN EN ISO 15792-1 derart entnommen, dass die Kerbe in der Mitte des Schweißguts liegt. Die Proben wurden gemäß DIN EN ISO 148-1 bei unterschiedlichen Temperaturen geprüft.

Abbildung 1: Querschliff einer Schweißgutprobe im geätzten Zustand. Mit einem Pfeil ist die zuletzt aufgetragene Schweißlage markiert.

Tabelle 1: Chemische Zusammensetzung der verwendeten Ätzmittel [10].

Ätzmittel	**Zusammensetzung**	**Ätzzeit**
Pikrinsäure	100 ml kaltgesättigte Pikrinsäure, 5 ml Agepon, 10 ml Xylol, 0,5 ml HCl	60 s
Nital	3% HNO_3 in Ethanol	3 s

Tabelle 2: Verwendete Parameter für EBSD Messungen.

Spannung	20 kV
Strom	10 nA
Binning	4x4
Tilt angle	70°
Background	Standard
Hough Pattern Type	Classic
Hough Resolution	Low
Convolution Mask	9x9
Binned pattern size	120
Theta step size	0,5

3 Ergebnisse und Diskussion

3.1 Lichtmikroskopie

Nach einer Ätzung mit Pikrinsäure war eine dendritische Struktur sichtbar (Abb. 2). Diese entsteht während der Erstarrung. Aufgrund der Legierungszusammensetzung und der damit erwarteten Erstarrungsbedingungen konnte geschlossen werden, dass es sich hierbei um die primär entstehenden δ-Ferrit Dendriten und nicht um die danach entstehende γ-Austenit Struktur handelt.

Eine Aufnahme derselben Stelle nach einer Nital-Ätzung ist in Abb. 3 dargestellt. Die Nital-Ätzung wird bei bainitischen und martensitischen Stählen üblicherweise zur Sichtbar-machung der Lattenstruktur verwendet. Im Falle des Schweißguts entstand allerdings bei Betrachtung der geätzten Probe mit kleiner Vergrößerung zusätzlich ein deutlicher Kontrast durch Grau-Schattierungen. Eine genauere Untersuchung der unterschiedlich schattierten Bereiche ergab,

dass die Schattierung mit der ehemaligen Austenitstruktur in Verbindung gebracht werden kann. So erstreckte sich z.B. eine Martensitlatte niemals über eine Grenze zwischen zwei unterschiedlich schattierten Bereichen. Die längliche Form der Austenitkörner lässt auf eine gerichtete Erstarrung aufgrund eines großen Temperaturgradienten schließen.

Diese zwei Methoden boten sich somit an, um unterschiedlich legierte Proben hinsichtlich der jeweiligen Korngröße auszuwerten und diese danach mit den mechanischen Eigenschaften zu vergleichen. Zuvor wurden jedoch noch EBSD-Messungen durchgeführt, um diese mit den lichtmikroskopischen Versuchen zu korrelieren.

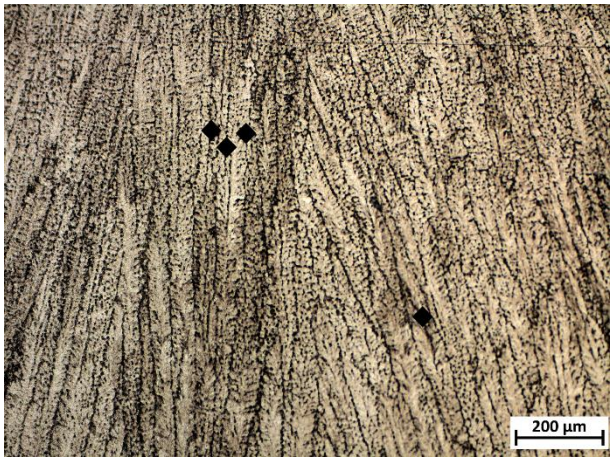

Abbildung 2: Dendritische Mikrostruktur nach Ätzung mit Pikrinsäure, aufgenommen im Lichtmikroskop. Die Härteeindrücke dienen zur Markierung der betrachteten Stelle für weiterführende Untersuchungen.

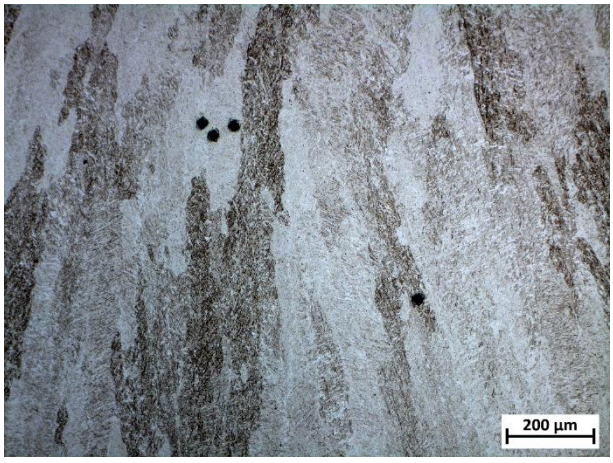

Abbildung 3: Lichtmikroskopische Aufnahme der Probe nach einer Nital-Ätzung. Die entstandenen Grau-Schattierungen können mit der ehemaligen Austenitstruktur in Verbindung gebracht werden.

3.2 EBSD

Der EBSD Scan von der mit Härteeindrücken markierten Stelle ist in Abb. 4 zu sehen. Jedem gemessenen Punkt wurde gemäß seiner kristallografischen Orientierung nach dem Farbdreieck links unten im Bild eine Farbe zugeordnet („inverse pole figure map“). Die typische Lattenstruktur des Martensits ist deutlich erkennbar. Diese „inverse pole figure map“ wurde über eine lichtmikroskopische Aufnahme nach Nital-Ätzung gelegt. Charakteristische Formen im EBSD-Bild passten exakt zu denen im Nital-Bild. Es kam also zu keinen nennenswerten Verzerrungen mit fortschreitender Dauer des EBSD Scans.

Aufgrund der Orientierungs-Beziehung zwischen Austenit und Martensit [4] können innerhalb eines ehemaligen Austenitkorns immer nur ähnliche Farben auftreten. Ein Vergleich der Grau-Schattierungen in Abb. 3 und der Farbbereiche in Abb. 4 zeigte, dass zwar einige ehemalige Austenitkörner durch die Grau-Schattierungen wiedergegeben werden, dass aber in den EBSD Scans zusätzliche ehemalige Austenitkörner sichtbar sind. Eine Nital-Ätzung reicht also nicht aus, das ehemalige Austenitgefüge vollständig zu enthüllen.

Vergleicht man Abb. 4 mit Abb. 2, kann man einen Zusammenhang der Wachstumsrichtung der primären Dendriten und der sekundären Austenitkörner feststellen. Es besteht aber sonst keine Abhängigkeit der Morphologie der Austenitkörner von der Form der primären Dendriten, weshalb die dendritische Struktur und die Austenitkornstruktur getrennt voneinander zu betrachten sind.

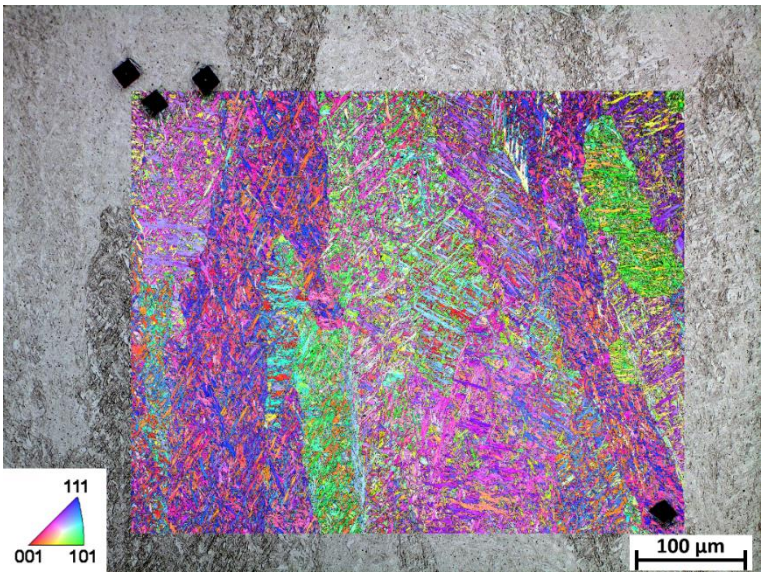

Abbildung 4: Bild nach Nital-Ätzung und „inverse pole figure map“ eines EBSD Scans übereinander gelegt.

3.3 Korngrößen und mechanische Eigenschaften

Abb. 5 zeigt die gemessenen primären und sekundären Dendritenabstände mehrerer Proben mit unterschiedlichem Legierungsgehalt. Zusätzlich ist die Kerbschlagarbeit bei Raumtemperatur und bei -40 °C aufgetragen. Der primäre Dendritenabstand ist in allen Fällen größer als der sekundäre Dendritenarmabstand. Es besteht jedoch keine Verbindung zwischen den Dendritenabständen und der Kerbschlagarbeit. Betrachtet man zum Beispiel die Proben S1 und S4, so sind die Dendritenabstände kaum unterschiedlich, die Kerbschlagarbeiten sind aber sehr unterschiedlich. Daraus kann man schließen, dass die Dendritengröße und die damit verbundene interdendritische Seigerung keinen Einfluss auf die Kerbschlagarbeit des Schweißguts haben.

Es muss somit ein anderer Faktor ausschlaggebend sein für die mechanischen Eigenschaften. Es ist altbekannt, dass in martensitischen Stählen die ehemalige Austenitkorngröße maßgeblich für die Kerbschlagarbeit ist. Neuere Untersuchungen zeigten zusätzlich, dass die ehemalige Austenitkorngröße linear von der Größe der „blocks“ und „packets“ abhängt [7]. Daher ist eine tiefgehende Untersuchung dieser mikrostrukturiellen Einheiten nötig. Es zeigte sich, dass dafür die Lichtmikroskopie mit Nital-Ätzung nicht ausreicht. EBSD lieferte hingegen ein kompletteres Bild der Mikrostruktur. In weiterer Folge soll deshalb mit EBSD gearbeitet werden, um die daraus gewonnenen Daten mit den mechanischen Eigenschaften korrelieren zu können.

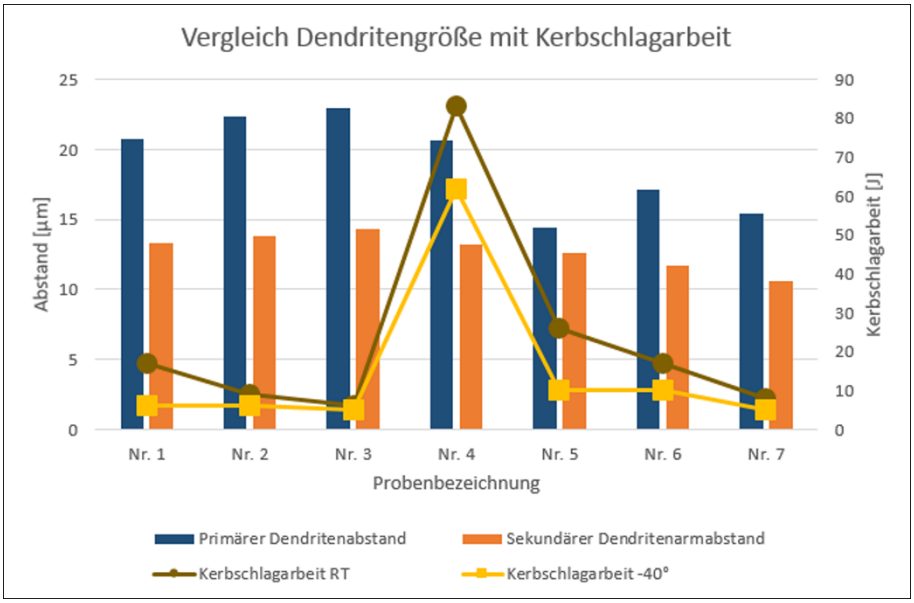

Abbildung 5: Vergleich der primären und sekundären Dendritenabstände mehrerer Proben mit ihrer Kerbschlagarbeit (Charpy-V).

4 Schlussfolgerungen

- Die Mikrostruktur von martensitischem Schweißgut wurde mit unterschiedlichen Methoden untersucht.
- Eine Ätzung mit Pikrinsäure bringt die primäre dendritische Struktur von der Erstarrung über δ-Ferrit zum Vorschein. Vergleich man die Dendritengröße mit den mechanischen Eigenschaften, lässt sich kein Zusammenhang erkennen.
- Nach Nital-Ätzung zeigt sich eine Grau-Schattierung, die mit der ehemaligen Austenitstruktur in Verbindung gebracht werden kann.
- EBSD-Untersuchungen zeigten, dass die Grau-Schattierung nach der Nital-Ätzung nicht ausreicht, um die ehemaligen Austenitkörner vollständig zu charakterisieren.
- Weiterführende Versuche mit EBSD sind daher notwendig, um die Mikrostruktur bestmöglich charakterisieren zu können. Danach wird eine neuerliche Korrelation mit den mechanischen Eigenschaften angestrebt.

5 Danksagung

Das K-Projekt Network of Excellence for Metal JOINing wird im Rahmen von COMET - Competence Centers for Excellent Technologies durch BMWFW, BMVIT, FFG, Land Oberösterreich, Land Steiermark, Land Tirol und SFG gefördert. Das Programm COMET wird durch die FFG abgewickelt.

6 Literatur

1. Rauch R, Kapl S, Posch G, Radlmayr K (2012) High Strength Low Alloy Steel Weldments with Accommodated Qualities to the Base Metal. BHM Berg- und Hüttenmännische Monatshefte 157:102–107. doi: 10.1007/s00501-012-0060-5
2. Bouyne E, Flower HM, Lindley TC, Pineau A (1998) Use of EBSD technique to examine microstructure and cracking in a bainitic steel. Scr Mater 39:295–300. doi: 10.1016/S1359-6462(98)00170-5
3. Gourgues A-F, Flower HM, Lindley TC (2000) Electron backscattering diffraction study of acicular ferrite, bainite, and martensite steel microstructures. Mater Sci Technol 16:26–40. doi: 10.1179/026708300773002636
4. Morito S, Tanaka H, Konishi R, et al (2003) The morphology and crystallography of lath martensite in Fe-C alloys. Acta Mater 51:1789–1799. doi: 10.1016/j.actamat.2006.07.009
5. Morito S, Huang X, Furuhara T, et al (2006) The morphology and crystallography of lath martensite in alloy steels. Acta Mater 54:5323–5331. doi: 10.1016/j.actamat.2006.07.009
6. Miyamoto G, Takayama N, Furuhara T (2009) Accurate measurement of the orientation relationship of lath martensite and bainite by electron backscatter diffraction analysis. Scr Mater 60:1113–1116. doi: 10.1016/j.scriptamat.2009.02.053
7. Galindo-Nava EI, Rivera-Díaz-del-Castillo PEJ (2015) A model for the microstructure behaviour and strength evolution in lath martensite. Acta Mater 98:81–93. doi: 10.1016/j.actamat.2015.07.018
8. Vanovsek W, Bernhard C, Fiedler M, Posch G (2013) Influence of aluminum content on the characterization of microstructure and inclusions in high-strength steel welds. Weld World 57:73–83. doi: 10.1007/s40194-012-0008-0
9. Vanovsek W, Bernhard C, Fiedler M, Schnitzer R (2013) Effect of titanium on the solidification and postsolidification microstructure of high-strength steel welds. Weld World 57:665–674. doi: 10.1007/s40194-013-0063-1
10. Petzow G (1976) Metallographisches Aetzen, 5th ed. Gebrueder Borntraeger, Berlin
11. Schwartz AJ, Kumar M, Adams BL, Field DP (2009) Electron Backscatter Diffraction in Materials Science, 2nd ed. doi: 10.1007/978-0-387-88136-2

Paper II

Haslberger P, Holly S, Ernst W, Schnitzer R (2017)

Microstructural characterization of martensitic all-weld metal samples

Practical Metallography 54: 513-532

DOI: 10.3139/147.110464

Microstructural characterization of martensitic all-weld metal samples

Phillip Haslberger[a], Sylvia Holly[b], Wolfgang Ernst[c], Ronald Schnitzer[a]

[a] Department Physical Metallurgy and Materials Testing, Montanuniversität Leoben, Austria

[b] voestalpine Böhler Welding Austria GmbH, Kapfenberg, Austria

[c] voestalpine Stahl Linz GmbH, Austria

Abstract

The development of welding consumables is permanently challenged with matching the increasing strength and toughness of thermomechanically treated or quenched and tempered steels. A martensitic microstructure offers promising prospects to guarantee such requirements in the all-weld metal as well. A thorough characterization of the microstructure is indispensable to understand its effects on the mechanical properties. This paper shall summarize how light optical microscopy and electron backscatter diffraction can be used to deepen the understanding of fully martensitic weld metal. It was found that electron backscatter diffraction offers a variety of information that light optical microscopy cannot deliver, particularly regarding the prior austenite grain structure. Grain sizes of the primary dendrites, the prior austenite grains and the martensitic structure can be measured with a combination of these techniques.

Anmerkung: Die deutsche Übersetzung dieses Artikels mit dem Titel „Gefügecharakterisierung martensitischer Proben aus reinem Schweißgut“ ist in der Zeitschrift abgedruckt.

1 Introduction

Steel development is confronted with the permanent need for lightweight structures with maximum load capacity. Nowadays the alloying concept and thermomechanical processing of steel sheets can be more or less easily adjusted to achieve a very high strength and toughness. For further processing, a part of these sheets needs to be welded. This leads to a profound challenge for the welding consumables manufacturer because the welding consumable must match the strength and toughness of the base material. Currently, much effort is being made to reach a sufficiently high strength by designing the filler metal as well as the welding process to produce a martensitic microstructure in the weld, while keeping the toughness at an acceptable level. In this process, the understanding of the relationship between the microstructure and the resulting mechanical properties is a key factor. The focus of this paper shall therefore be set on the methods for a thorough characterization of the martensitic weld metal microstructure, especially compared to the used methods for commercially available high strength weld metals.

High strength weld metals with a tensile strength in the range of 600 – 900 MPa usually consist of mixed microstructures [1–7]. As the fractions of microstructural constituents can drastically influence the mechanical properties, much work has been put into the identification of the different constituents, all the way from polygonal ferrite to martensite. While the amount of polygonal or globular ferrite and acicular ferrite can be assessed quite easily [2,4,5,8], a distinction between martensite and different bainitic structures is more difficult and mostly based on the carbide distribution [3,6,7]. In all these cases, the method of choice is etching the sample with nital and investigating the sample by light optical microscopy (LOM) or scanning electron microscopy (SEM), depending on the resolution needed. If a more detailed characterization of lath-like structures like bainite and martensite was necessary, transmission electron microscopy was carried out [2,7,9].

In the current study, weld metal with a strength of 1000 MPa or higher and a fully martensitic microstructure is investigated. Therefore, a determination of constituent fractions is not applicable and a different approach must be used to analyze the martensitic microstructure and its influences on the mechanical properties.

The martensitic microstructure in steel and its characterization have been extensively studied over the past few decades [10–14]. The use of light optical microscopy and scanning electron microscopy has delivered a vast amount of information regarding partly and fully martensitic microstructures. Nevertheless, with the advance of characterization techniques the understanding of martensite got refined. Electron backscatter diffraction (EBSD) in particular

was used to gain deep insight into the crystallographic properties of needle-shaped microstructures like acicular ferrite, bainite and martensite [15–19]. After verifying the existence of an orientation relationship between martensite and the prior austenite, the hierarchic structure of martensite was investigated more closely [20,21]. It is now accepted that a prior austenite grain (PAG) can be divided into packets, blocks, sub-blocks and laths [22,23]. In order to link the present microstructure to the mechanical properties of a martensitic steel, a close look at all microstructural features is hence necessary.

Although a great variety of martensitic steels have been investigated in this manner, only little work has been done on martensitic weld metal. Due to its different thermal history, the microstructure of weld metal is significantly different from the microstructure of steel sheets. This leads to additional challenges in its characterization, which will be discussed in the following pages.

2 Materials and methods

All investigations were carried out on all-weld metal samples fabricated by gas metal arc welding in accordance with DIN EN ISO 15792-1. The approximate amount of the main alloying elements of the weld is stated in table 1.

The samples for investigation in the LOM were mounted in resin, ground with SiC papers and polished with 3 µm and 1 µm diamond suspension. For cleaning after each polishing step no water was used in order to avoid corrosion. Different etchants were used for contrasting the microstructure. The composition and etching procedure of the etchants used is given in table 2. The first etching attempts were based on the work of Vanovsek et al., who used picric acid to reveal the primary dendritic structure [24], and both picric acid and nital etching to reveal the (secondary) PAG structure [24,25]. In addition to the picric acid agent in table 2, several modifications (e.g. Bechet-Beaujard) were tried, but showed no improvement regarding the visibility of the PAG structure. Because the results were in general unsatisfactory (see section 3), the LePera etchant [26] was applied for comparison as well.

Table 1: Alloying element contents of the weld [m.%].

C	Si	Mn	Cr	Mo	Ni	Fe
0.09	0.80	2.5	0.75	0.70	3.0	Rest

Table 2: Used etchants for investigations in the LOM.

Name	Composition	Procedure
Nital	3% HNO_3 in ethanol	Etching for 2-3 seconds
Picric acid	100 ml saturated picric acid, 10 ml Xylol, 0.5 ml HCl, a few drops of liquid soap as a wetting agent	Etching for ca. 60 seconds, immersing in hot water before cleaning
LePera	Two parent solutions [26], mixed 1:1	Mixing of parent solutions directly before wetting the surface with ethanol and etching for ca. 30 seconds

As pointed out in the introduction, EBSD is a valuable source of information regarding martensitic microstructures. Therefore, it was used complementarily to LOM to investigate the crystallographic features in the weld metal samples.

For the EBSD measurements the polished samples were additionally vibropolished for 2 h in an OPS suspension, and subsequently the mounting resin was removed. They were examined in a FIB Versa 3D DualBeam equipped with an EDAX Hikari XP EBSD system. The working principle of EBSD can be found in [27,28]. The samples were tilted to 70° and placed at a working distance of 15 mm. The parameters for the EBSD scans are listed in table 3. The patterns were collected and analyzed using EDAX OIM Software.

Table 3: Parameters for the EBSD measurements.

Parameter	Value
Voltage	30 kV
Current	10 nA
Binning	4x4
Step size	100 – 500 nm
Background	Standard
Hough p. type	Classic
Hough resolution	Low
Convolution mask	9x9
Binned pattern size	120
Theta step size	0.5°

3 Results and discussion

3.1 Light optical microscopy

3.1.1 Picric acid

An overview of a specimen etched with picric acid is shown in figure 1. The morphology of the welding beads is clearly visible. The top bead remelted some of the material of the previously deposited layers. In each welding bead most of the structure inside the beads is oriented parallel to the temperature gradient during welding because of a pronounced directional solidification. A columnar or dendritic structure is revealed at higher magnifications (figure 2). The dendrites are arranged in groups with the same growing direction and are narrowly spaced.

Figure 1: Low magnification image of specimen etched with picric acid, revealing the morphology of the welding beads and the directional growth of the microstructure.

Figure 2: Specimen etched with picric acid (see figure 1). The dendritic structure formed during solidification is visible at this magnification.

The appearance of the primary dendritic structure after etching with picric acid is surprising at first sight, as picric acid is specifically known as a PAG structure etchant [29,30]. However, the all-weld metal can be compared to a cast steel with very fast cooling times. During solidification, the alloying elements and impurities can segregate to the solidification front, which leads to interdendritic segregation. Afterwards, the material is in the austenitic state for a very short time, which limits the amount of segregation of impurities to the austenite grain boundaries. With picric acid, areas with high contents of impurities are etched due to their difference in chemical potential compared to the matrix. In the case of all-weld metal this leads to the revelation of the dendritic structure instead of the PAG structure.

3.1.2 Nital

After nital etching again two different contrasts are visible. At higher magnifications the final martensitic microstructure is revealed (figure 3), including some PAG boundaries which are indicated by arrows. Some of the different austenite grains seem to have a different grey shading. At low magnifications this effect becomes more prominent, with figure 4 showing a columnar PAG structure. This grey shading appears due to an orientation contrast, which was qualitatively explained in [31]. In some areas, however, the difference in grey shading is too small in order to be used for an evaluation of the PAG size.

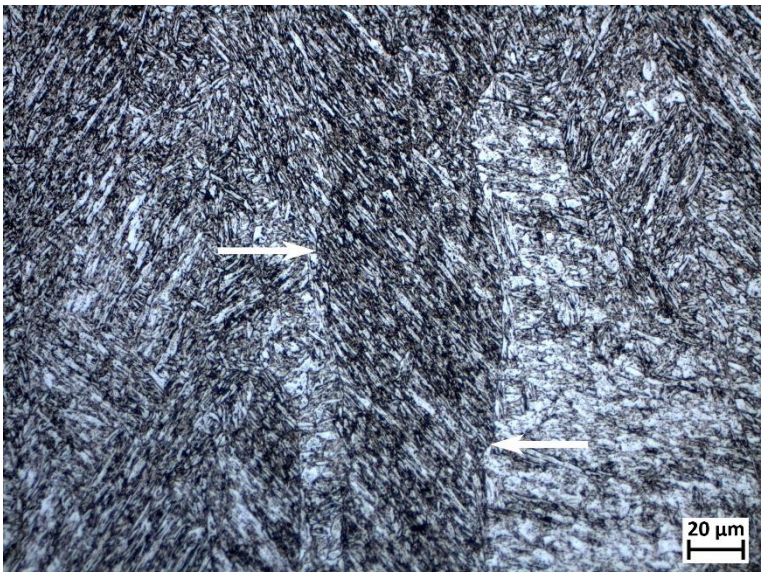

Figure 3: Specimen etched with nital. Some PAG boundaries can be identified in addition to the martensitic microstructure, as indicated by white arrows.

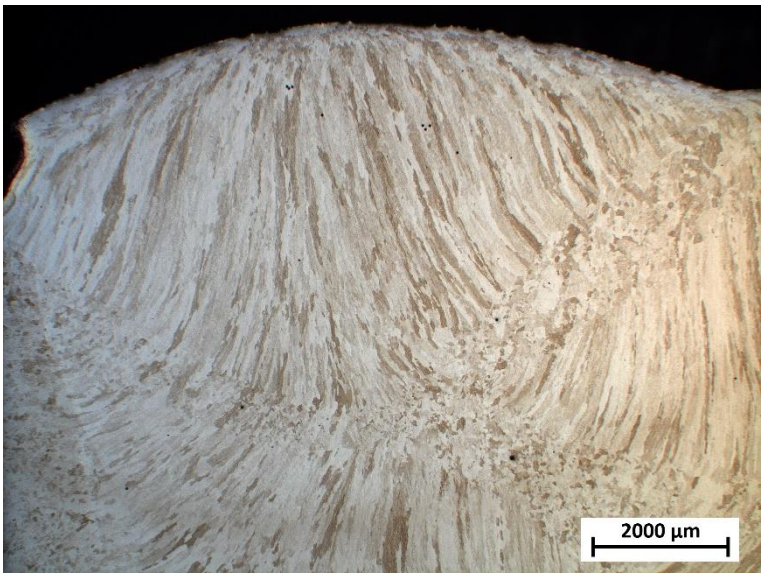

Figure 4: Specimen etched with nital. At low magnifications a grey or brown shading illustrates the elongated morphology of the PAG structure.

3.1.3 LePera

For steel the LePera agent is usually used for mixed microstructures to identify the existence and amount of multiple phases within one sample [26]. However, in the case of the present sample and its solely martensitic microstructure, etching with LePera yields similar results as etching with picric acid. At low magnifications the morphology of the welding beads can be identified (figure 5). Nevertheless, some additional features can be seen compared to figure 1. Elliptical dark zones appear (indicated by arrows in figure 5), each of which originates from reheating of the material by the subsequent welding bead. The patchy appearance of the microstructure can be linked to groups of dendrites growing in the same direction. Figure 6 shows a boundary between two welding beads (indicated by arrows). In general, a columnar or dendritic structure is once again visible. Additionally, in some areas the martensitic needle-shaped microstructure can be identified. There is a distinct difference in size of the dendrites of the top bead and the bottom bead. This is related to the local cooling rates after depositing the weld metal. The cooling rate is fastest at the bottom of the bead because of the direct contact to the metal the bead is deposited on. The resulting cooling rate gradient over the welding bead is responsible for a dendritic grain size gradient.

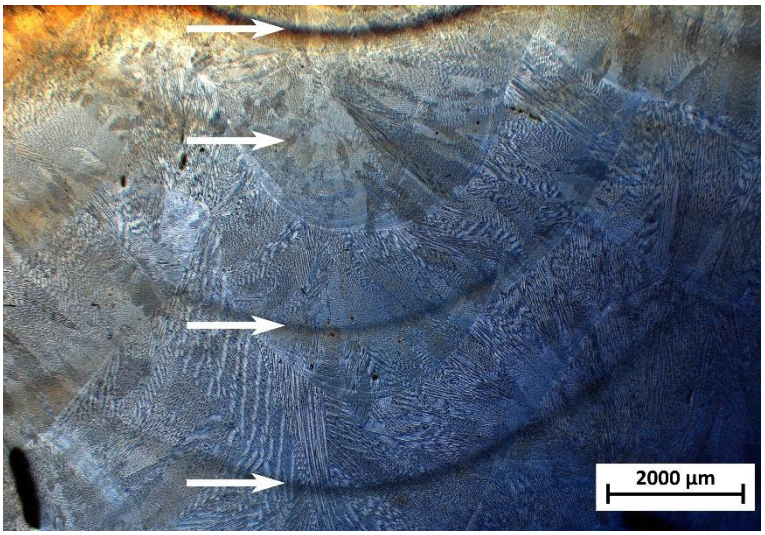

Figure 5: Specimen etched with LePera. The morphology of the welding beads can be seen. White arrows indicate elliptical dark zones originating from reheating of the material by the subsequently deposited welding bead.

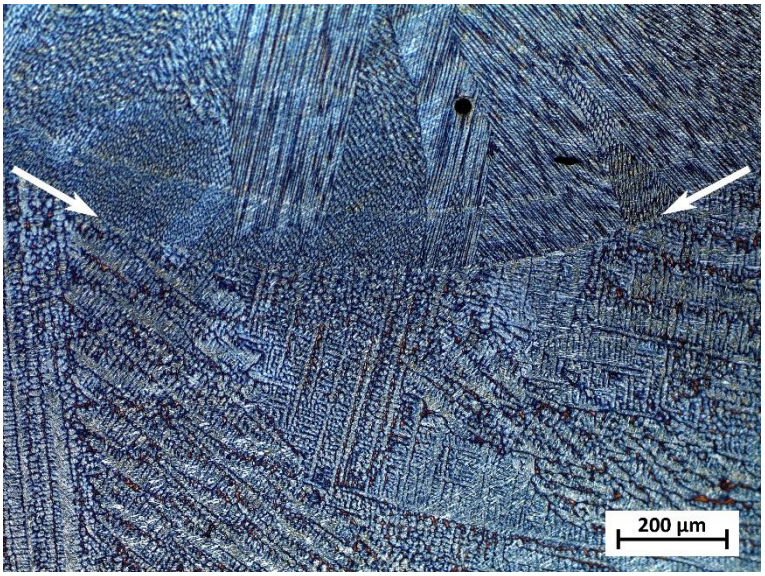

Figure 6: Specimen etched with LePera. The primary dendritic structure is clearly resolved. White arrows indicate a boundary between two welding beads.

3.1.4 Which etchant for which purpose?

In figures 7a and 7b the exact same sample position is shown after etching with nital and with picric acid, respectively. Although the growth direction of the dendrites and the PAGs is the same, there is no direct morphological correspondence between the grey shading after nital etching and the dendritic structure after etching with picric acid. Therefore, every etchant has

its own purpose for the characterization of the microstructure of martensitic all-weld steel samples. Picric acid can be used to have a look at the primary dendritic structure and for an evaluation of the primary and secondary dendrite spacing [24]. Nital etching provides some indications of the PAG structure at low magnifications and the martensitic microstructure itself at higher magnifications. LePera etching delivers both the primary dendritic structure and the final martensitic microstructure, as well as additional information on the morphology of the beads and their heat affected zone. So, although the LePera etchant cannot serve its usual purpose of revealing different phases because of the solely martensitic microstructure, it produces a broad spectrum of information.

Unfortunately, none of the etchants described could be used to assess a reliable PAG size. For this purpose, EBSD investigations were carried out.

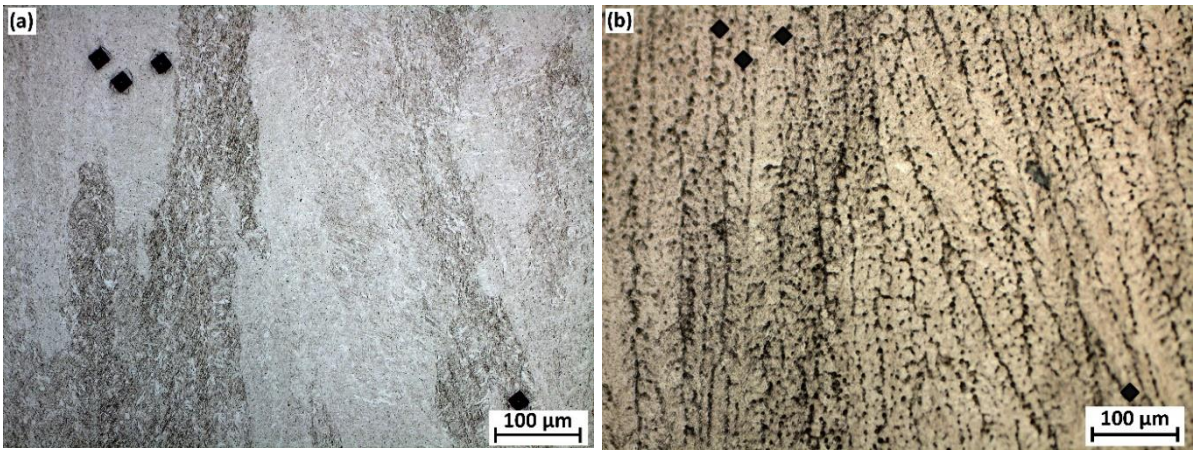

Figure 7: The same sample position, as marked by hardness indents, was etched with (a) nital and (b) picric acid. A correlation between the growth direction of the differently shaded PAGs in (a) and the dendrites in (b) can be detected. However, no direct relationship between the morphologies of the PAGs and dendrites can be identified.

3.2 Electron backscatter diffraction

3.2.1 Qualitative observations

At first, a random position in the weld metal was measured with EBSD. An image quality (IQ) map overlaid with an inverse pole figure (IPF) map of this trial EBSD measurement is shown in figure 8. Each point has a brightness value linked to the image quality of the Hough pattern

from the EBSD measurement. Additionally, each point in the map is colored according to its measured crystallographic orientation in the IPF triangle in the bottom right of figure 8. The blocks of the martensitic microstructure are clearly resolved.

It is generally accepted, that there exists an orientation relationship between martensitic blocks and their PAGs [20]. Therefore, in figure 8 regions with similarly colored blocks can be interpreted as PAGs. Nevertheless, a clear distinction of two adjacent PAGs is only possible, if the austenite grains had a large misorientation before the martensite transformation and the color sets of their martensitic structure are very different. This qualitative approach is insufficient for a precise determination of the PAGs. Instead, the actual EBSD data has to be analyzed.

3.2.2 PAG reconstruction with method by Abbasi [32]

An effective way to divide the PAGs is to use pole figures, as was suggested by Abbasi [32]. Due to the orientation relationship between prior austenite and martensite, highly symmetric shapes appear in the pole figures. These can be used to identify the PAGs step by step. As shown in figure 9, the scan from figure 8 was cut into several small pieces, and for each of these pieces the PAGs were identified via highlighting in the respective pole figures. Subsequently, the PAG boundaries were mapped in white in the original IQ+IPF map.

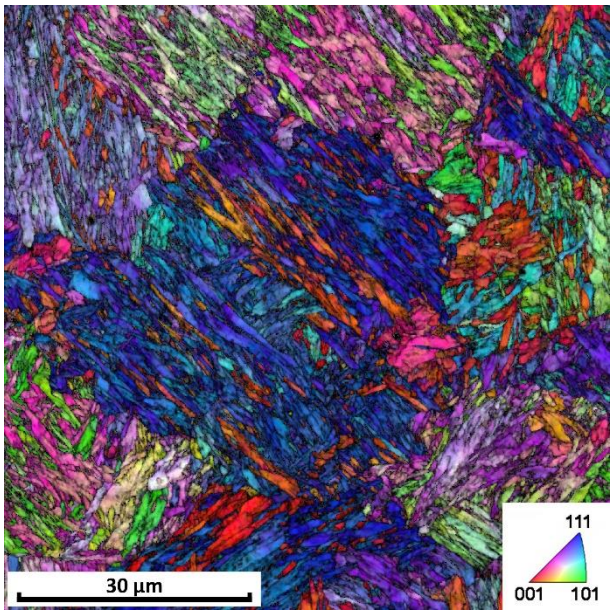

Figure 8: Image quality + image pole figure map of an EBSD scan at a random position in the middle of the weld sample. The smallest microstructural feature resolved in this scan is the martensitic block.

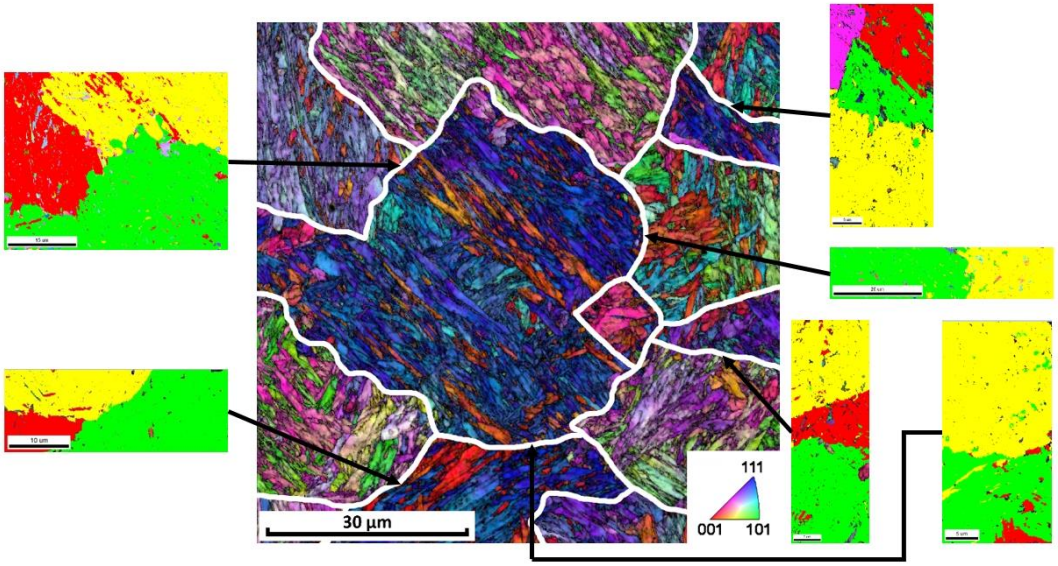

Figure 9: Manually reconstructed PAG structure of the scan from figure 8. The scan was cut in several pieces, in which the different PAGs were highlighted in different colors.

As expected, most of the PAGs show a significant difference in the colors of their blocks. However, the exact pathway of the PAG boundaries would be difficult to find by eye, which is why a reconstruction method based on the actual crystallographic data is recommended. Also, compared to conventional methods, the verification of the existence of PAG boundaries with the use of pole figures offers a certainty, that light optical microscopy and conventional scanning electron microscopy just cannot match.

The reconstruction using the pole figures and the mapping were carried out manually. Although this is feasible for such a small scan, for larger scans an automated method is recommended. This was necessary in order to identify a large enough number of PAGs for the determination of the PAG size.

3.2.3 PAG reconstruction with method by Cayron [33]

For an automated reconstruction of the PAGs of the trial scan (figure 8) the program ARPGE by Cayron et al. was used [33,34]. In general, reconstructions with the Greninger-Troiano relationship [35] and with the standard values from the program showed the best results regarding both the orientational accuracy and the expected morphology of the PAGs. The usage of quadruplets instead of triplets for the reconstruction showed only little effect. In figure 10 the resulting PAG reconstruction is depicted. Although many PAG boundaries correspond to the manual reconstruction in figure 9, ARPGE finds some more PAGs. This

discrepancy results from inaccuracies in both methods. However, both methods seem to reconstruct the PAG structure reasonably well. A verification of ARPGE reconstructions on a thermomechanically treated steel was also carried out by Weyand et al. [36], who used nital etched samples for comparison. In their case, the visual appearance of the reconstructed PAGs fitted very well to the nital images. Due to reconstruction artifacts, the PAG size from ARPGE was slightly smaller compared to the nital evaluation. These results comply with the results of the current paper. After verifying the ARPGE reconstructions of several scans by additional manual reconstruction, it was decided to proceed with the automated method and reconstruct a larger scan that could be used for PAG size evaluation. Figure 11a shows the initial IPF map and figure 11b the reconstructed PAGs of such a larger scan. The PAG structure is columnar, as was already described in section 3.1.2 and figure 4. Contrary to a nital etched sample, figure 11b can be used for PAG size evaluation because all PAGs can clearly be separated.

3.2.4 Which method for which purpose?

This question arises because EBSD requires a more elaborate sample preparation and a SEM compared to a LOM. Additionally, the time of acquisition and PAG reconstruction is rather extensive for EBSD scans of the size and resolution needed. Many different etchants have been developed for revealing different microstructures in steel [29]. In the case of martensitic weld metal, some of them could be used to investigate the primary dendritic structure, while others showed the final needle-shaped martensitic microstructure. However, one big piece in the puzzle of the microstructure of martensitic steel was missing: the PAG structure. LOM with nital etched samples may give some indications of the PAG structure (figures 3 and 4), but this grey shading coming from an orientation contrast is far too vague to serve as a foundation for a PAG size evaluation. In this case, EBSD has to be carried out. The automatic reconstruction with ARPGE is the fastest way to reconstruct the PAGs and gives reasonably accurate results (figures 10 and 11). After the reconstruction, a PAG size evaluation by the linear intercept method can be carried out. This intercept method is a good way to characterize the column width of this columnar grain structure. However, as is evident in figure 11b, the majority of the PAGs does not fit in one scan in longitudinal direction. Therefore, morphological parameters like area or aspect ratio, which would be needed for a complete description of the microstructure, cannot be evaluated.

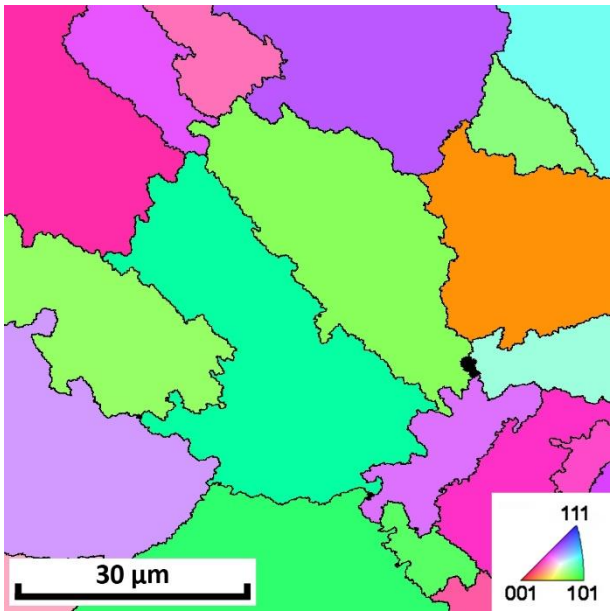

Figure 10: PAG structure of the scan from figure 8, reconstructed with ARPGE.

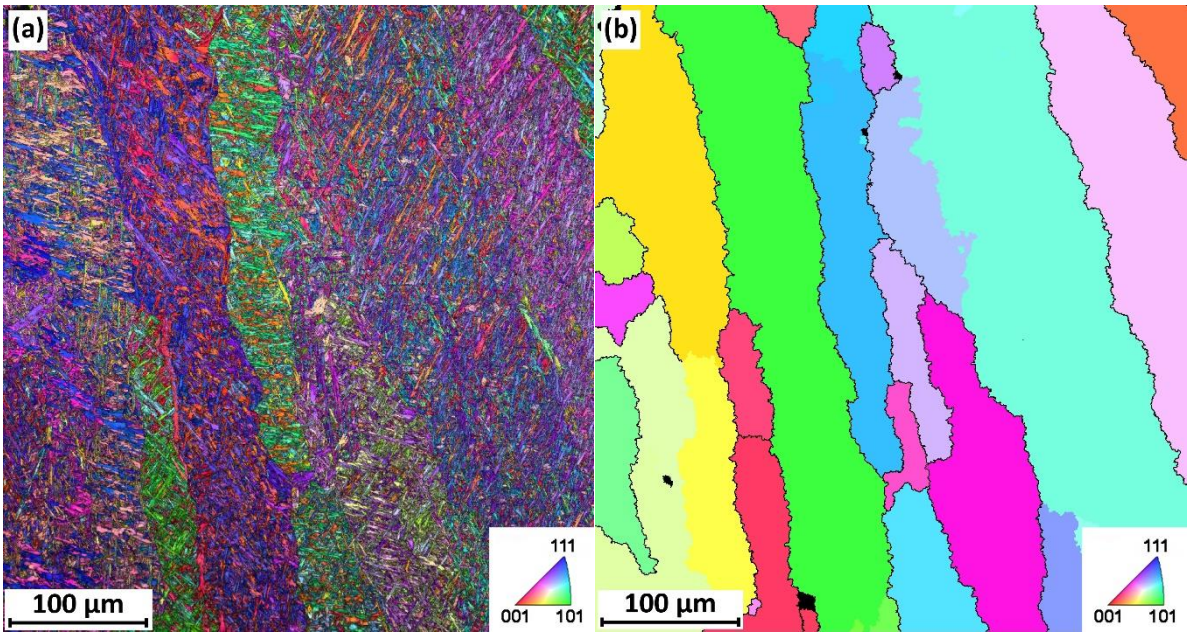

Figure 11: (a) IPF map of random sample position. (b) Corresponding IPF map of PAG reconstruction with ARPGE.

3.2.5 Grain size evaluation on all hierarchic levels

With the microscopic methods described above, a grain size of the primary dendritic structure and the final martensitic structure as well as a column width of the PAGs can be evaluated. In every case several images from different locations were investigated in order to measure a feasible number of grains.

An evaluation of the primary dendritic structure comprises the spacing of the dendritic trunks (λ_1) as well as the spacing of the dendritic arms (λ_2). This evaluation is described in [24]. In the current weld sample, the average spacings were measured after etching with picric acid, because in the LePera images the dendritic structure is obscured to some extent by the additional contrast of the final martensitic microstructure. The measured spacings were λ_1 = 20.6 ± 5.4 µm and λ_2 = 13.2 ± 1.4 µm.

The columnar PAG structure was evaluated from several EBSD scans after the reconstruction with ARPGE using the linear intercept method. The lines were set perpendicular to the longitudinal axis of the columns. An average intercept length of 51.9 ± 11.2 µm was measured.

Finally, from the original EBSD scans a grain size similar to the martensitic block size can be evaluated by measuring the average equivalent diameter of grains with a tolerance angle of 10.5 degrees. This method is explained in more detail in [37]. The average grain size of the scan in figure 11a was 7.5 ± 6.8 µm. The high standard deviation comes from the inherently irregular grain structure.

These grain sizes can be compared to the mechanical properties of the martensitic weld metal in order to identify the controlling mechanisms for strength and toughness.

4 Conclusions

- The microstructure of martensitic all-weld steel samples produced by gas metal arc welding was investigated with light optical microscopy and electron backscatter diffraction.
- Etching with picric acid or LePera revealed the primary dendritic structure. LePera additionally resolved the final martensitic microstructure.
- With nital etching the prior austenite grains were differently shaded. However, it was difficult to distinguish all prior austenite grains.
- A reliable characterization of the prior austenite grain size is not possible with light optical microscopy in the case of martensitic gas metal arc welds.
- Because of the collected crystallographic information, EBSD measurements can be used to reconstruct the prior austenite grain structure.
- Both methods by Abbasi and Cayron yield reasonably accurate results. For large scans the method by Cayron is much faster.
- With a combination of light optical microscopy and electron backscatter diffraction a grain size evaluation on all hierarchic levels of the martensitic microstructure in weld metals is possible.

5 Acknowledgement

The K-Project Network of Excellence for Metal JOINing is fostered in the frame of COMET - Competence Centers for Excellent Technologies by BMWFW, BMVIT, FFG, Land Oberösterreich, Land Steiermark, Land Tirol and SFG. The program COMET is handled by FFG.

6 References

1. Johnson MO, Evans GM, Edwards G (1995) The Influence of Titanium Additions and Interpass Temperature on the Microstructures and Mechanical Properties of High Strength SMA Weld Metals. ISIJ Int 35:1222–1231.
2. Bose-Filho WW, Carvalho ALM, Strangwood M (2007) Effects of alloying elements on the microstructure and inclusion formation in HSLA multipass welds. Mater Charact 58:29–39. doi: 10.1016/j.matchar.2006.03.004
3. Keehan E, Zachrisson J, Karlsson L (2010) Influence of cooling rate on microstructure and properties of high strength steel weld metal. Sci Technol Weld Join 15:233–238. doi: 10.1179/136217110X12665048207692
4. Bajic N, Sijacki-Zeravcic V, Bobic B, et al (2011) Filler Metal Influence on Weld Metal Structure of Microalloyed Steel. Weld J 90:55s–62s.
5. Jiang QL, Li YJ, Wang J, Zhang L (2011) Effects of inclusions on formation of acicular ferrite and propagation of crack in high strength low alloy steel weld metal. Mater Sci Technol 27:1565–1569. doi: 10.1179/026708310X12815992418535
6. Sumi H, Oi K, Yasuda K (2015) Effect of chemical composition on microstructure and mechanical properties of laser weld metal of high-tensile-strength steel. Weld World 59:173–178. doi: 10.1007/s40194-014-0191-2
7. Zhang T, Li Z, Ma S, et al (2016) High strength steel (600–900 MPa) deposited metals: microstructure and mechanical properties. Sci Technol Weld Join 21:186–193. doi: 10.1179/1362171815Y.0000000079
8. Evans GM (1998) Effect of Nitrogen on C-Mn Steel Welds Containing Titanium and Boron. Weld J 77:239–248.
9. Wansheng D, Yun P, Hongjun X, et al (2010) Microstructure and Toughness of 1000 MPa High Strength Weld Metal. Mater Sci Forum 638–642:3441–3446.
10. Bhadeshia HKDH, Honeycombe RWK (2006) Steels: Microstructure and Properties, 3rd ed. Butterworth-Heinemann, Oxford
11. Nishiyama Z (1978) Martensitic Transformation. Academic Press Inc., London
12. Krauss G, Marder AR (1971) The morphology of martensite in iron alloys. Metall Trans 2:2343–2357.
13. Krauss G (1999) Martensite in steel: strength and structure. Mater Sci Eng A 273–275:40–57. doi: 10.1016/S0921-5093(99)00288-9
14. Cohen M (1962) The strengthening of steel. Trans TMS - AIME 224:638–657.
15. Kluken AO, Grong Ø, Hjelen J (1991) The origin of transformation textures in steel weld metals containing acicular ferrite. Metall Trans A 22:657–663. doi: 10.1007/BF02670288
16. Dingley DJ, Randle V (1992) Microtexture determination by electron back-scatter diffraction. J Mater Sci 27:4545–4566.
17. Hall MG, Aaronson HI (1994) Formation of invariant plane-strain and tent-shaped surface reliefs by the diffusional ledge mechanism. Metall Mater Trans A 25:1923–1931.
18. Bouyne E, Flower HM, Lindley TC, Pineau A (1998) Use of EBSD technique to examine microstructure and cracking in a bainitic steel. Scr Mater 39:295–300. doi: 10.1016/S1359-6462(98)00170-5
19. Gourgues A-F, Flower HM, Lindley TC (2000) Electron backscattering diffraction study of acicular ferrite, bainite, and martensite steel microstructures. Mater Sci Technol 16:26–40. doi: 10.1179/026708300773002636
20. Morito S, Tanaka H, Konishi R, et al (2003) The morphology and crystallography of lath martensite in Fe-C alloys. Acta Mater 51:1789–1799. doi: 10.1016/j.actamat.2006.07.009

21. Furuhara T, Kawata H, Morito S, Maki T (2006) Crystallography of upper bainite in Fe–Ni–C alloys. Mater Sci Eng A 431:228–236. doi: 10.1016/j.msea.2006.06.032

22. Morito S, Adachi Y, Ohba T (2009) Morphology and Crystallography of Sub-Blocks in Ultra-Low Carbon Lath Martensite Steel. Mater Trans 50:1919–1923. doi: 10.2320/matertrans.MRA2008409

23. Du C, Hoefnagels JPM, Vaes R, Geers MGD (2016) Block and sub-block boundary strengthening in lath martensite. Scr Mater 116:117–121. doi: 10.1016/j.scriptamat.2016.01.043

24. Vanovsek W, Bernhard C, Fiedler M, Posch G (2013) Influence of aluminum content on the characterization of microstructure and inclusions in high-strength steel welds. Weld World 57:73–83. doi: 10.1007/s40194-012-0008-0

25. Vanovsek W, Bernhard C, Fiedler M, Schnitzer R (2013) Effect of titanium on the solidification and postsolidification microstructure of high-strength steel welds. Weld World 57:665–674. doi: 10.1007/s40194-013-0063-1

26. LePera FS (1980) Improved Etching Technique to Emphasize Martensite and Bainite in High-Strength Dual-Phase Steel. JOM 32:38–39. doi: 10.1007/BF03354553

27. Schwartz AJ, Kumar M, Adams BL, Field DP (2009) Electron Backscatter Diffraction in Materials Science, 2nd ed. doi: 10.1007/978-0-387-88136-2

28. Humphreys FJ (2001) Grain and subgrain characterisation by electron backscatter diffraction. J Mater Sci 36:3833–3854. doi: 10.1023/A:1017973432592

29. Petzow G (1999) Metallographic Etching, 2nd ed. ASM International, Materials Park, Ohio

30. Schacht E, Richter J (1998) Erfahrung mit Ätzmittel zum Nachweis der ehemaligen Austenitkorngrenzen in Stählen. Prakt Met 35:384–395.

31. Haslberger P, Ernst W, Schnitzer R (2016) Mikrostrukturelle Charakterisierung von ultra-hochfesten Schweißgütern. BHM Berg- und Hüttenmännische Monatshefte 161:321–324. doi: 10.1007/s00501-016-0494-2

32. Abbasi M, Nelson TW, Sorensen CD, Wei L (2012) An approach to prior austenite reconstruction. Mater Charact 66:1–8. doi: 10.1016/j.matchar.2012.01.010

33. Cayron C, Artaud B, Briottet L (2006) Reconstruction of parent grains from EBSD data. Mater Charact 57:386–401. doi: 10.1016/j.matchar.2006.03.008

34. Cayron C (2007) ARPGE: A computer program to automatically reconstruct the parent grains from electron backscatter diffraction data. J Appl Crystallogr 40:1183–1188. doi: 10.1107/S0021889807048777

35. Greninger AB, Troiano AR (1949) The mechanism of martensite formation. Trans AIME 185:590–598.

36. Weyand S, Britz D, Rupp D, Mücklich F (2015) Investigation of Austenite Evolution in Low-Carbon Steel by Combining Thermo-Mechanical Simulation and EBSD Data. Mater Perform Charact 4:MPC20150010. doi: 10.1520/MPC20150010

37. Haslberger P, Ernst W, Schnitzer R (2017) High resolution imaging of martensitic all-weld metal. Sci Technol Weld Join 22:336–342. doi: 10.1080/13621718.2016.1240980

Paper III

Haslberger P, Ernst W, Schnitzer R (2017)

High resolution imaging of martensitic all-weld metal

Science and Technology of Welding and Joining 22: 336-342

DOI: 10.1080/13621718.2016.1240980

High resolution imaging of martensitic all-weld metal

Phillip Haslberger[a], Wolfgang Ernst[b], Ronald Schnitzer[a,c]

[a] Department Physical Metallurgy and Materials Testing, Montanuniversität Leoben, Austria

[b] voestalpine Stahl Linz GmbH, Austria

[c] voestalpine Böhler Welding Austria GmbH, Kapfenberg, Austria

Abstract

Martensitic steel welds show promising results regarding their strength whilst they may tend to be brittle. As martensite is a quite complex microstructure, high resolution techniques like Electron Backscatter Diffraction (EBSD) and Atom Probe Tomography (APT) are valuable tools for an in-depth characterisation. In this study the average block size and misorientation distribution of martensitic all-weld samples were evaluated with EBSD. A lower carbon content led to a smaller block size and consequently a higher toughness of the all-weld sample. Furthermore, APT revealed a concentration fluctuation of the main alloying elements and particles with a high carbon content. It is discussed how these methods can be used in the future to design the microstructure to achieve optimum properties.

1 Introduction

Welded steel structures are a crucial part of lightweight constructions in several industry segments. There is a permanent need for reducing the weight of structural components while keeping the load capacity at least at a constant level. Although light metals can be used in some applications, high strength steels still offer some advantages for lightweight constructions and are therefore continually improved. Many base metals with excellent mechanical properties are available. However, for welded joints also the welding process as well as the used filler metal play a vital role in optimising their properties. Especially the alloying concept of the filler material is developed to enhance the strength and toughness of the steel weld.

Acicular ferrite was found to be a beneficial microstructure compared to bainite in high strength steel welds [1–4]. The intragranular nucleation of ferrite laths on inclusions leads to a refined, interlocked microstructure [5,6], which combines high strength and high toughness. The amount of acicular ferrite in the weld metal can be maximised by adding titanium and nitrogen e.g., thus increasing the number density of active inclusions [7–10]. Nevertheless, for applications with a required strength of 1100 MPa the strength of weld metal consisting of acicular ferrite is insufficient. By a specific addition of solid solution strengtheners and other alloying elements retarding the austenite/ferrite transformation martensitic welds with the required high strength can be produced.

The microstructural characterisation of martensitic steel is an indispensable tool in order to understand its properties. Light Optical Microscopy and Scanning Electron Microscopy (SEM) on polished or etched metallographic samples have been used for several decades to characterise the ferritic as well as the prior austenitic microstructure. These methods are still used on a daily basis, also in the field of high strength weld metals [11–14]. However, the advance of high resolution techniques like Electron Backscatter Diffraction (EBSD) and Atom Probe Tomography (APT) considerably improved the knowledge of martensite in steels.

The crystallographic information gained from EBSD measurements revealed a complex substructure in martensite. It was shown that a prior austenite grain is divided into packets, which is built up by several blocks [15,16]. Further investigations showed, that these blocks are comprised of pairs of sub-blocks containing one specific variant from the Kurdjumov-Sachs orientation relationship, which are separated by low-angle boundaries [17]. Each sub-block is made up by multiple martensite laths. All these findings initiated a debate on the effective grain size for strength and crack propagation in martensitic steels. Further investigations proved that the toughness of martensite is inversely proportional to the packet and block size

because of their grain misorientation angle being greater than 15° [18–22]. Recently the results from several authors were summarised, indicating that block size and packet size are linearly dependent on the prior austenite grain size [23]. Thus all three hierarchic levels should be correlatable with the toughness of steel. Nevertheless, this paper will focus on the block size as effective grain size.

Besides grain size and grain boundary misorientation, the segregation of alloying elements can affect strength and toughness. In addition to the interdendritic segregation during solidification of the weld metal, especially nanometer-scale segregation can occur in martensitic materials during cooling and during reheating. As a method with nearly atomic resolution APT can be used to identify the nanoscale segregation behaviour of different alloying elements and the formation of clusters and particles in the material. Results from APT measurements suggest that carbon shows a complex segregation behaviour during tempering [23–27]. The carbon atoms diffuse towards lath boundaries and dislocation cores forming Cottrell atmospheres [23,28]. In later tempering stages carbides can form in these carbon-enriched zones. Furthermore, many alloying elements segregate to different types of grain boundaries during tempering. Typically, elevated manganese and silicon contents enhance the diffusion of phosphorus to the grain boundaries. This can cause severe embrittlement of the material [29–33]. Other alloying elements preferentially form clusters in early stages of precipitation before growing into a complete precipitate with a defined crystal structure and stoichiometry [34–39].

The aim of this work is to use high resolution methods in order to evaluate the morphologic, crystallographic, and chemical properties of ultra-high strength martensitic weld metal. The gained information from the powerful combination of EBSD for grain size evaluation and APT for studying nanoscale segregation effects can be used to design the microstructure to achieve optimum properties.

2 Materials and methods

For the investigations all-weld metal samples were prepared by Gas Metal Arc Welding according to DIN EN ISO 15792. The welding parameters are shown in tab. 1. Two samples of filler metals with different carbon contents and comparable amounts of alloying elements were used. Their chemical composition is specified in tab. 2. The oxygen content is in the range of 400 – 500 ppm for both alloys. The impact toughness at -20°C was 34 J for sample A and 22 J for the sample B. A cross-section of a weld sample treated with LePera etchant [40] is

depicted in fig. 1. After applying buffer layers directly onto the base material to avoid dilution, the joint was filled by multipass welding.

In this multilayer structure the microstructure of a weld bead is significantly altered due to the deposition of subsequent layers. The thermal history of every single point in the all-weld sample is different and cannot be fully reconstructed because of the complexity of the welding process itself. Only the last deposited weld bead stays unchanged after cooling. Consequently, the EBSD measurements were performed on the last deposited bead (as indicated by arrows in fig. 1) to find a correlation between the initial microstructure directly after cooling and the toughness of the whole weld.

The basic EBSD setup in a SEM is outlined in [41]. The samples were vibropolished for ca. 1 h before mounting in the SEM 'FEI Versa 3D DualBeam' equipped with an 'EDAX Hikari XP' EBSD system. For the actual measurement the software 'TSL OIM Data Collection 7' was used. A summary of the applied experimental parameters is listed in tab. 3. The crystallographic properties of the sample were evaluated with the software 'TSL OIM Analysis 7'.

Table 1: Used welding parameters for the production of all-weld metal samples.

Parameter	**Value**
Current	250 A
Voltage	30 V
Welding speed	50 cm/min
Heat input per unit length	9 kJ/cm
Interpass temperature	150 °C
$t_{8/5}$	8 s

Table 2: Chemical composition of the investigated materials [m%].

	C	**Si**	**Mn**	**Cr**	**Mo**	**Ni**	**Fe**	**M_S [°C]**
Sample A	0.08	0.74	2.38	0.63	0.73	2.55	Rest	376
Sample B	0.10	0.84	2.48	0.72	0.76	3.10	Rest	363

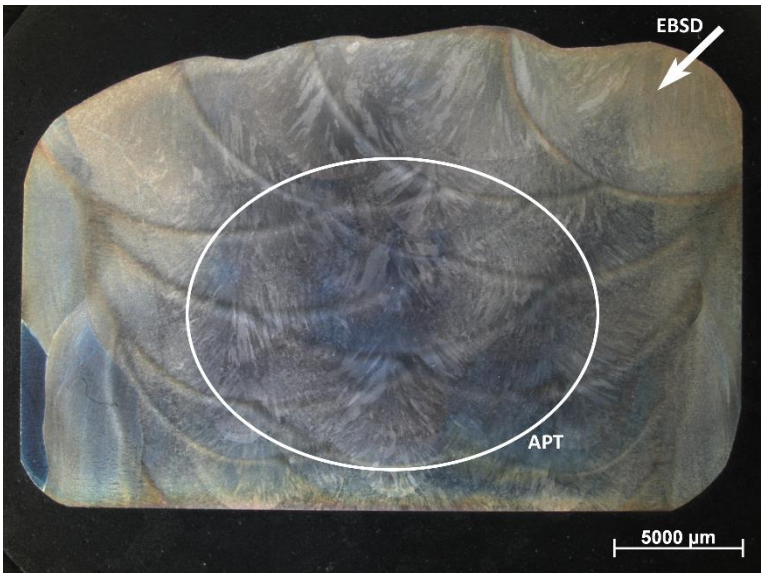

Figure 1: Cross-sectional view of a weld sample treated with LePera etchant. EBSD scans were carried out in the last deposited weld bead, which is indicated with an arrow. APT measurements were performed at random locations inside the marked area.

Table 3: Measurement parameters for all EBSD experiments.

Parameter	**Value**
Voltage	20 kV
Current	10 nA
Binning	4x4
Specimen tilt angle	70°
Step size	300 nm
Background	Standard
Hough Pattern Type	Classic
Hough resolution	Low
Convolution Mask	9x9
Binned pattern size	120
Theta step size	0.5

Atom Probe Tomography was used to examine the element distributions in the centre region of the all-weld metal sample (fig. 1). Therefore, in contrast to the EBSD measurements, in this case tempering effects by subsequently deposited weld beads were taken into account because the segregation contents were expected to be higher in reheated regions of the weld metal. Rods with a cross section of 0.3 x 0.3 mm² were cut in longitudinal direction from the

material at random positions within the centre region. The tips were subsequently prepared by electropolishing [42] and mounted in a 'Cameca LEAP 3000X HR'. The functional principle and applications of Atom Probe Tomography can be looked up in [43,44]. All samples were measured in laser mode, at a temperature of 60 K, with a laser energy of 0.3 nJ, a pulse rate of 250 kHz, and a target evaporation rate of 1 %. A reconstruction software 'Cameca IVAS 3.6.8' was used to evaluate the Atom Probe measurements and allocate the atoms to their original positions in the tip.

3 Results

3.1 EBSD

An inverse pole figure (IPF) map overlaid with an image quality (IQ) map of sample A is shown in fig. 2. Every data point was coloured to represent its measured crystallographic orientation according to the inverse pole figure colouring triangle in the bottom right corner. An additional grey shading indicating the quality of the observed diffraction pattern generated an enhancement of the morphologic grain structure. The lath-like martensitic microstructure is clearly visible. Furthermore, vertically elongated areas containing the same set of specific colours were found. Because of the orientation relationship between martensite and prior austenite [15] these similarly coloured areas could be identified as prior austenite grains.

The crystallographic information from the EBSD measurements was used to calculate a distribution of the crystallographic grain size and the misorientation distribution. For the grain size it was chosen to use an equivalent diameter, which was found to be least prone to artefacts in the EBSD evaluation software. A comparison of the grain size distributions of the samples A and B is depicted in fig. 3. The peak is shifted to a bigger grain size for the sample B. This corresponds to the calculated average grain size values, which are 11.5 µm for sample A and 23.0 µm for sample B. The misorientation distributions in fig. 4 reveal a greater relative amount of small angle boundaries in sample B compared to sample A. As a direct consequence the relative amount of high angle boundaries is higher in sample A. The average misorientation angle is 28.5° in sample A and 25.0° in sample B.

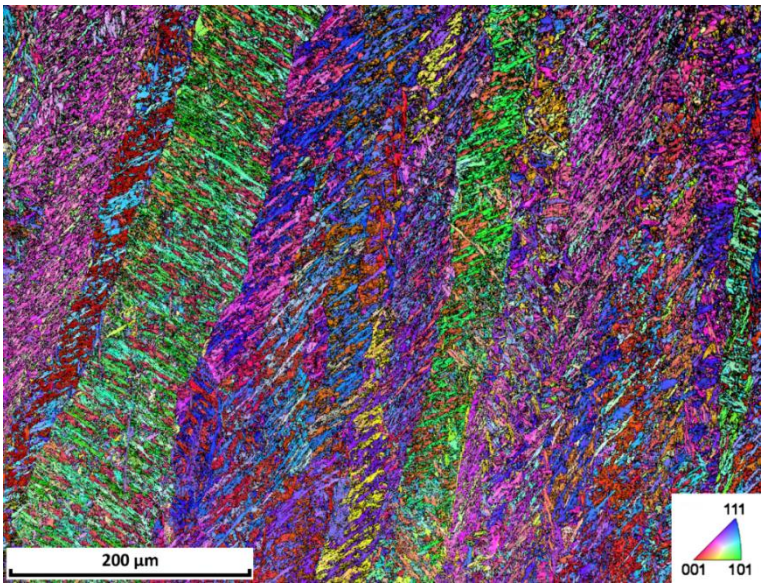

Figure 2: Inverse pole figure and image quality map of sample A. Each data point is coloured according to its measured crystallographic orientation, and its brightness is adjusted according to the image quality of the observed diffraction pattern.

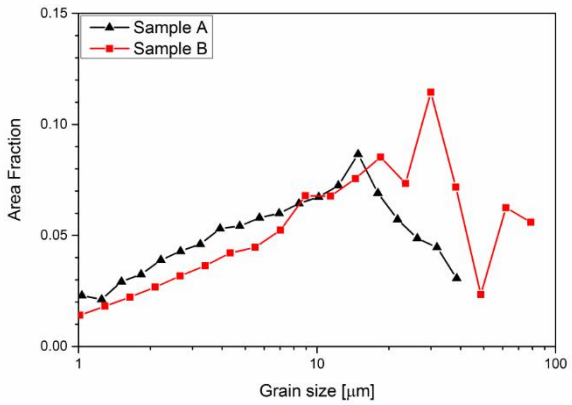

Figure 3: Crystallographic grain size distribution of samples A and B.

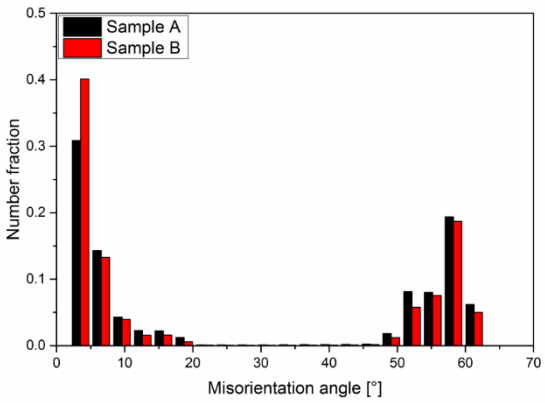

Figure 4: Grain misorientation distribution of samples A and B.

3.2 APT

A reconstructed tip of sample A is shown in fig. 5. In this 2D-projection of a 3D-reconstruction every point corresponds to one single atom. However, for each element only a fraction of the actually measured atoms is drawn for clear visualisation. The atomic distribution of C revealed a transition from a carbon-depleted zone into a carbon-enriched zone. Also Mn and Mo seemed to be slightly enriched at the interface between the two zones. The Fe atoms appeared to be equally distributed. In order to quantitatively characterise the atomic distributions, a 1D concentration profile perpendicular to the interface along the longitudinal axis of the cylinder shown in fig. 6a was calculated. The interface was highlighted by creating an isoconcentration surface with a C concentration of 1.6 at%. The concentration profile is depicted in fig. 6b. Not only C, but also Mn, Ni and Mo are slightly enriched in the lower part of the tip. Directly at the interface Mn and Ni show concentration peaks.

The reconstruction of a tip of sample B is shown in fig. 7. From the atomic distributions it can be stated that again a carbon-enriched area was measured. All other alloying elements seemed to be equally distributed and are therefore not explicitly shown. The isoconcentration surface with 3 at% in fig. 8a represents the carbon-enriched zone. A cylinder was again placed perpendicular to the interface and a 1D concentration profile was calculated (fig. 8b). The C content of the enriched zone is similar to that of sample A. However, in this case no enrichment of Ni, Mn or Mo was observed.

By increasing the isoconcentration value to 12 at% a particle could be identified (fig. 9a). The particle was exported and in fig. 9b all its Fe and C atoms are visible. An analysis of the chemical composition of the particle yielded a C concentration of 17 at%, whereas all other alloying elements resembled their matrix content. As there were no significant amounts of carbide forming elements in this particle, it was identified as cementite.

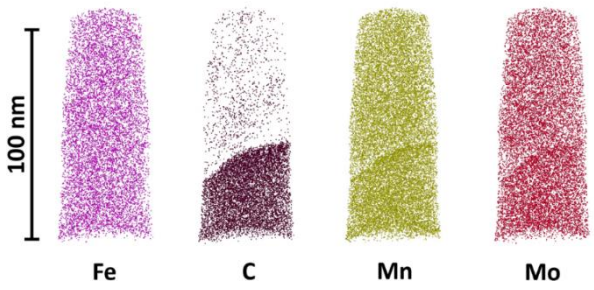

Figure 5: Reconstructed APT measurement of sample A. One point corresponds to one single atom. In these 2D-projections the positions of the atoms of different alloying elements are shown separately.

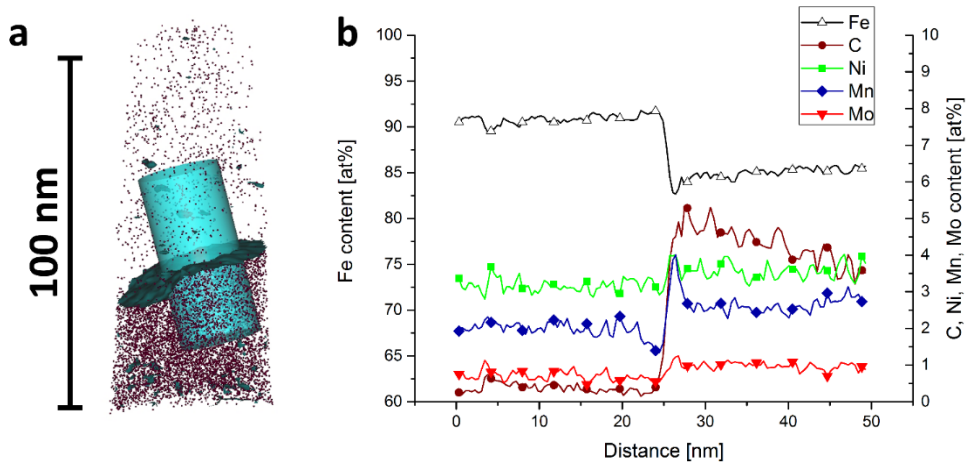

Figure 6: **a** Cylinder placed perpendicular to the interface found in sample A. **b** Concentration profile along the longitudinal axis of the cylinder.

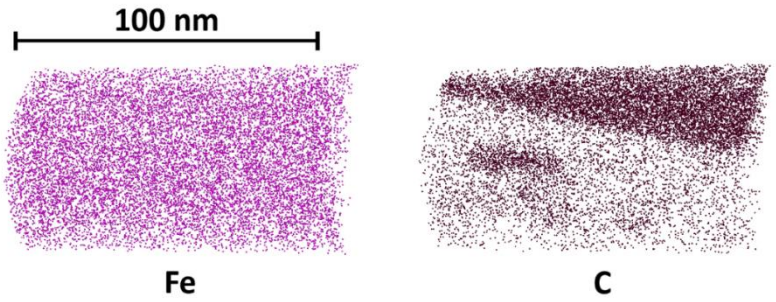

Figure 7: Reconstructed APT measurement of sample B. One point corresponds to one single atom. In these 2D-projections the positions of the atoms of different alloying elements are shown separately.

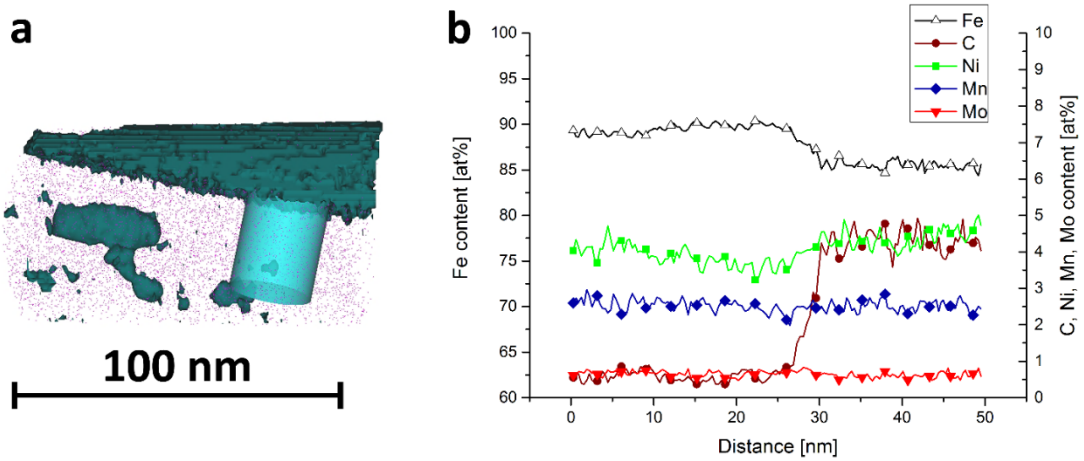

Figure 8: **a** Cylinder placed perpendicular to the interface found in sample B. **b** Concentration profile along the longitudinal axis of the cylinder.

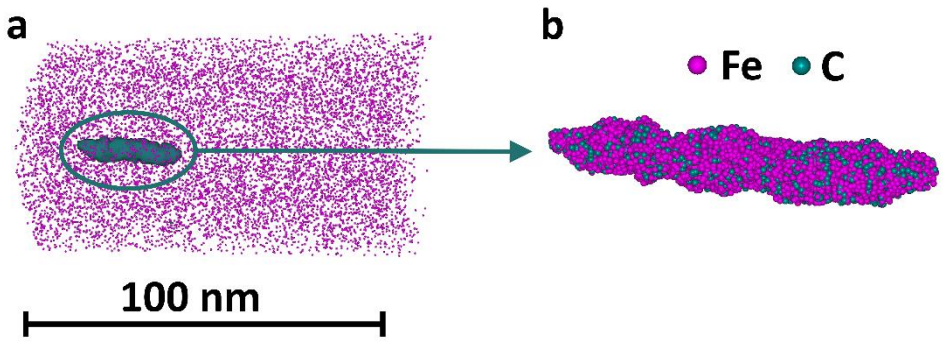

Figure 9: **a** Reconstructed APT measurement of sample B. Fe atoms are shown with an enveloped C-rich particle, which is magnified in **b**.

4 Discussion

Owing to the complexity of multilayer welding regarding reheating processes and local heat inputs, the microstructure of an all-weld sample is a mixture of a variety of differently heat affected areas. Grain sizes and shapes are changed because of high peak temperatures and possible reaustenitisation. The only area, which is not reheated and where a reliable assessment of the grain structure and size is possible, is the last deposited weld bead. It was therefore attempted to determine a grain size of this initial microstructure and correlate this grain size with the toughness of the whole all-weld sample.

EBSD was chosen, as it delivers a broad spectrum of data regarding the morphology and crystallography of the microstructure. A correct interpretation of the EBSD data is essential for valid and reliable results. Literature shows that the crystallographic grain size measured by EBSD is actually the martensitic block size if the tolerance angle is chosen correctly [15,19]. Investigations by several authors demonstrated that the block size is linearly dependent on the prior austenite grain size. Galindo-Nava and Rivera-Diaz-del-Castillo [23] summarised and extended these results. The block size can therefore be used as an indicator for the prior austenite grain size, which has always been linked to the toughness in steel. Additionally, recent micromechanical investigations showed, that during mechanical failure cracks are deflected at block boundaries, whereas they can propagate through sub-block boundaries [22]. As a consequence, it is not surprising that sample A with a smaller average block size (fig. 3) shows a higher impact toughness. Blocks are the smallest microstructural units in martensite separated by high angle boundaries, whereas single martensite laths and sub-blocks are separated by low angle boundaries. The generally higher fraction of high angle

boundaries in the reference sample (fig. 4) is one further promoter of a higher toughness, as was concluded by several groups [19,45].

It is generally accepted, that in steels the martensitic block size decreases with increasing carbon content, which was first shown in [15]. Surprisingly, the current study produced contradictory results. After evaluating other samples with different chemical compositions, which are not shown in this paper, a trend emerged that the block size is mainly dependent on the martensite start temperature. Further investigations are necessary in order to prove why in steel weld metal the block size decreases with increasing martensite start temperature.

The evaluation of the martensitic grain size in the last deposited weld bead and the attempt to correlate the measured grain size with the toughness of the weld metal neglects any effects of reheating on the microstructure. By contrast, tempering can lead to extensive redistribution of alloying elements in the microstructure, which can also affect the toughness of steel.

APT with its nearly atomic resolution allows the detection of very small amounts of alloying elements at their original position. It can be used to qualitatively and quantitatively assess the extent of nanometer-scale segregation of alloying elements in steel. In the present study the APT measurements were performed in repeatedly reheated regions of the all-weld metal because higher segregation contents were expected than in the last deposited weld bead. It was found that C-enriched zones are present in the weld metal (figs. 5 and 7). Also Mn and Ni segregated towards an interface in the steel and have slightly elevated contents in the C-enriched zone (figs. 5 and 6). These facts suggest the assumption of the C-enriched zones being films of retained austenite [46]. By comparing samples with different alloying contents the amount of segregation to grain boundaries and other segregation effects can be rated regarding their influence on the impact toughness of the weld.

Additionally, by evaluating chemical fluctuations and atomic distances from APT measurements particles can be found at the smallest possible scale. In the current results the chemical composition of the exported particle (fig. 9) points towards cementite. However, when carbide or nitride forming elements are added, these can affect size and shape of the precipitates, which are vital for the strength properties of steel. The chemical and size evolution of the particles depending on alloying composition and thermal history can be evaluated with APT.

Many factors play a role in determining the mechanical properties of the steel weld. The presented high resolution imaging methods can deliver a broad range of information about the microstructure at a small scale. The combination of characterising the initial martensitic microstructure directly after cooling by EBSD and studying segregation effects by APT poses a major advantage over conventional light and electron microscopy. In the future these

techniques will be used to judge the modification of the microstructure caused by alterations of the chemical composition of the weld samples. By purposefully adjusting the alloying concept of the weld an attempt is made to achieve optimum properties.

5 Conclusions

In the current study the microstructure of martensitic all-weld metal samples was investigated with high resolution imaging methods. In EBSD scans the martensitic microstructure was clearly visible. Additionally, the prior austenite grain structure was partly revealed. A comparison of the crystallographic properties of two samples showed that the sample with a higher carbon content had a bigger block size and a higher fraction of low angle boundaries. This led to a smaller impact energy compared to the reference sample. By APT analyses of the reference sample carbon-enriched regions were found. Also other alloying elements tended to segregate to a grain boundary. Furthermore, it was achieved to measure a small cementite particle. In the future these methods will be used to investigate several differently alloyed samples in order to assess the relationship between grain size and segregation contents and the mechanical properties in martensitic welds.

6 Acknowledgement

The K-Project Network of Excellence for Metal JOINing is fostered in the frame of COMET - Competence Centers for Excellent Technologies by BMWFW, BMVIT, FFG, Land Oberösterreich, Land Steiermark, Land Tirol and SFG. The program COMET is handled by FFG.

7 References

1. Bhadeshia HKDH (2001) Bainite in steels, 3rd ed. Institute of Materials, Cambridge
2. Grong O, Matlock DK (1986) Microstructural development in mild and low-alloy steel weld metals. Int Met Rev 31:27–48. doi: 10.1179/imtr.1986.31.1.27
3. Farrar RA, Harrison PL (1987) Acicular ferrite in carbon-manganese weld metals: An overview. J Mater Sci 22:3812–3820. doi: 10.1007/BF01133327
4. Abson DJ (1989) Non-metallic inclusions in ferritic steel weld metals - a review. Weld World, Le Soudage Dans Le Monde 27:76–101.

5. Sugden A, Bhadeshia H (1989) Lower acicular ferrite. Metall Trans A 20:1811–1818.

6. Babu SS, Bhadeshia HKDH (1991) Mechanism for the Transition from Bainite to Acicular Ferrite. Mater Trans 32:679–688.

7. Evans GM (1995) Microstructure and properties of ferritic steel welds containing Al and Ti. Weld J 74:249s–261s.

8. Evans GM (1998) Effect of Nitrogen on C-Mn Steel Welds Containing Titanium and Boron. Weld J 77:239–248.

9. Blais C, L'Espérance G, Evans G (1999) Characterisation of inclusions found in C–Mn steel welds containing titanium. Sci Technol Weld Join 4:143–150.

10. Seo JS, Seo K, Kim HJ, Lee C (2014) Effect of titanium content on weld microstructure and mechanical properties of bainitic GMA welds. Weld World 58:893–901. doi: 10.1007/s40194-014-0168-1

11. Keehan E, Zachrisson J, Karlsson L (2010) Influence of cooling rate on microstructure and properties of high strength steel weld metal. Sci Technol Weld Join 15:233–238. doi: 10.1179/136217110X12665048207692

12. Vanovsek W, Bernhard C, Fiedler M, Posch G (2013) Influence of aluminum content on the characterization of microstructure and inclusions in high-strength steel welds. Weld World 57:73–83. doi: 10.1007/s40194-012-0008-0

13. Vanovsek W, Bernhard C, Fiedler M, Schnitzer R (2013) Effect of titanium on the solidification and postsolidification microstructure of high-strength steel welds. Weld World 57:665–674. doi: 10.1007/s40194-013-0063-1

14. Sumi H, Oi K, Yasuda K (2015) Effect of chemical composition on microstructure and mechanical properties of laser weld metal of high-tensile-strength steel. Weld World 59:173–178. doi: 10.1007/s40194-014-0191-2

15. Morito S, Tanaka H, Konishi R, et al (2003) The morphology and crystallography of lath martensite in Fe-C alloys. Acta Mater 51:1789–1799. doi: 10.1016/j.actamat.2006.07.009

16. Kitahara H, Ueji R, Tsuji N, Minamino Y (2006) Crystallographic features of lath martensite in low-carbon steel. Acta Mater 54:1279–1288. doi: 10.1016/j.actamat.2005.11.001

17. Morito S, Adachi Y, Ohba T (2009) Morphology and Crystallography of Sub-Blocks in Ultra-Low Carbon Lath Martensite Steel. Mater Trans 50:1919–1923. doi: 10.2320/matertrans.MRA2008409

18. Kim HJ, Kim YH, Morris JW (1998) Thermal Mechanisms of Grain and Packet Refinement in a Lath Martensitic Steel. ISIJ Int 38:1277–1285. doi: 10.2355/isijinternational.38.1277

19. Kim M-C, Jun Oh Y, Hwa Hong J (2000) Characterization of boundaries and determination of effective grain size in Mn-Mo-Ni low alloy steel from the view of misorientation. Scr Mater 43:205–211. doi: 10.1016/S1359-6462(00)00392-4

20. Morito S, Yoshida H, Maki T, Huang X (2006) Effect of block size on the strength of lath martensite in low carbon steels. Mater Sci Eng A 438–440:237–240. doi: 10.1016/j.msea.2005.12.048

21. Wang C, Wang M, Shi J, et al (2007) Effect of Microstructure Refinement on the Strength and Toughness of Low Alloy Martensitic Steel. J Mater Sci Technol 23:659–664.

22. Du C, Hoefnagels JPM, Vaes R, Geers MGD (2016) Block and sub-block boundary strengthening in lath martensite. Scr Mater 116:117–121. doi: 10.1016/j.scriptamat.2016.01.043

23. Galindo-Nava EI, Rivera-Díaz-del-Castillo PEJ (2015) A model for the microstructure behaviour and strength evolution in lath martensite. Acta Mater 98:81–93. doi: 10.1016/j.actamat.2015.07.018

24. Miller MK, Beaven P a., Smith GDW (1981) A Study of the Early Stages of Tempering of Iron-carbon Martensites by Atom Probe Field Ion Microscopy. Metall Trans A 12:1197–1204. doi: 10.1007/BF02642333

25. Thomson RC, Miller MK (1995) The partitioning of substitutional solute elements during the tempering of martensite in Cr and Mo containing steels. Appl Surf Sci 87/88:185–193.

26. Zhu C, Cerezo A, Smith GDW (2009) Carbide characterization in low-temperature tempered steels. Ultramicroscopy 109:545–52. doi: 10.1016/j.ultramic.2008.12.007

27. Lerchbacher C, Zinner S, Leitner H (2012) Atom probe study of the carbon distribution in a hardened martensitic hot-work tool steel X38CrMoV5-1. Micron 43:818–826. doi: 10.1016/j.micron.2012.02.005

28. Wilde J, Cerezo A, Smith GDW (2000) Three-dimensional atomic-scale mapping of a Cottrell atmosphere around a dislocation in iron. Scr Mater 43:39–48. doi: 10.1016/S1359-6462(00)00361-4

29. Joshi A, Palmberg PW, Stein DF (1975) Role of Mn and Si in temper embrittlement of low alloy steels. Metall Trans A 6:2160–2161.

30. Smith JF, Reynolds JH, Southworth HN (1980) The role of Mn in the temper embrittlement of a 3.5 NiCrMoV steel. Acta Metall 28:1555–1564.

31. Yu J, McMahon J (1980) The effects of composition and carbide precipitation on temper embrittlement of 2.25Cr-1Mo steel: Part II. Effects of Mn and Si. Metall Trans A 11A:291–300.

32. Bodnar RL, Ohhashi T, Jaffee RI (1989) Effects of Mn Si and Purity on the design of 3.5NiCrMoV, 1CrMoV, and 2.25Cr-1Mo bainitic alloy steels. Metall Trans A 20A:1445–1460.

33. Heo NH, Nam JW, Heo Y, Kim S (2013) Grain boundary embrittlement by Mn and eutectoid reaction in binary Fe – 12Mn steel. Acta Mater 61:4022–4034. doi: 10.1016/j.actamat.2013.03.016

34. Gladman T (1997) The physical metallurgy of microalloyed steels. The Institute of Materials, London

35. Craven AJ, MacKenzie M, Cerezo A, et al (2008) Spectrum imaging and three-dimensional atom probe studies of fine particles in a vanadium micro-alloyed steel. Mater Sci Technol 24:641–650. doi: 10.1179/174328408X270347

36. Xie KY, Zheng T, Cairney JM, et al (2012) Strengthening from Nb-rich clusters in a Nb-microalloyed steel. Scr Mater 66:710–713. doi: 10.1016/j.scriptamat.2012.01.029

37. Isheim D, Kolli RP, Fine ME, Seidman DN (2006) An atom-probe tomographic study of the temporal evolution of the nanostructure of Fe-Cu based high-strength low-carbon steels. Scr Mater 55:35–40. doi: 10.1016/j.scriptamat.2006.02.040

38. Miller MK, Russell KF (2007) Embrittlement of RPV steels: An atom probe tomography perspective. J Nucl Mater 371:145–160. doi: 10.1016/j.jnucmat.2007.05.003

39. Wang H, Yu X, Isheim D, et al (2013) High strength weld metal design through nanoscale copper precipitation. Mater Des 50:962–967. doi: 10.1016/j.matdes.2013.03.093

40. LePera FS (1980) Improved Etching Technique to Emphasize Martensite and Bainite in High-Strength Dual-Phase Steel. JOM 32:38–39. doi: 10.1007/BF03354553

41. Humphreys FJ (2001) Grain and subgrain characterisation by electron backscatter diffraction. J Mater Sci 36:3833–3854. doi: 10.1023/A:1017973432592

42. Miller MK, Cerezo A, Hetherington MG, Smith GDW (1996) Atom probe field ion microscopy. Clarendon Press, Oxford

43. Kelly TF, Miller MK (2007) Invited review article: Atom probe tomography. Rev Sci Instrum 78:1–20. doi: 10.1063/1.2709758

44. Miller MK, Forbes RG (2009) Atom probe tomography. Mater Charact 60:461–469. doi: 10.1016/j.matchar.2009.02.007

45. Gourgues A-F, Flower HM, Lindley TC (2000) Electron backscattering diffraction study of acicular ferrite, bainite, and martensite steel microstructures. Mater Sci Technol 16:26–40. doi: 10.1179/026708300773002636

46. Caballero FG, Miller MK, Clarke AJ, Garcia-Mateo C (2010) Examination of carbon partitioning into austenite during tempering of bainite. Scr Mater 63:442–445. doi: 10.1016/j.scriptamat.2010.04.049

Paper IV

Haslberger P, Holly S, Ernst W, Schnitzer R (2018)

Precipitates in microalloyed ultra-high strength weld metal studied by atom probe tomography

Accepted for publication in Welding in the World

Precipitates in microalloyed ultra-high strength weld metal studied by atom probe tomography

Phillip Haslberger[a], Sylvia Holly[b], Wolfgang Ernst[c], Ronald Schnitzer[a]

[a] Department Physical Metallurgy and Materials Testing, Montanuniversität Leoben, Austria

[b] voestalpine Böhler Welding Austria GmbH, Kapfenberg, Austria; now with: voestalpine Wire Technology GmbH, Bruck/Mur, Austria

[c] voestalpine Stahl Linz GmbH, Austria

Abstract

Gas metal arc welding with metal-cored filler wires is frequently used to weld high strength steel constructions for lightweight and transportation applications. In the current study, microalloying is considered as strengthening concept for reaching the required mechanical properties by precipitation hardening. For this purpose, the typical microalloying elements Ti, Nb, V and Al were added to the filler metal in a comparatively high amount (up to 0.5 m.%). All-weld metal samples with a yield strength of 1000 MPa and more were produced by gas metal arc welding. Laser-pulsed atom probe tomography was used to evaluate the potential of these elements to form clusters or precipitates and strengthen the weld metal. While Al and Nb did not form clusters, a strong tendency for clustering was found for V- and Ti-alloyed samples. The cluster size evolution and changes in chemical composition depending on the microalloying contents are discussed. Furthermore, the challenges arising from local alloying element enrichments and local differences in thermal history in the all-weld metal are addressed regarding sample preparation and data evaluation.

1 Introduction

Welding of steels with matching filler materials promises a well-balanced property profile over the entire construction. High strength steels are currently used for cranes, cantilevers or lightweight applications. Sheets with a yield strength up to 1300 MPa are readily available, which results in the need for matching welding consumables. In the field of welding the trade-off between strength and toughness of the material is ubiquitous because of the limited applicability of thermomechanical processing after welding. Therefore, an elaborate alloy design is crucial for good service properties.

With high strength steel welds, the best results were achieved by using the well-known microalloying elements Al and Ti for modifications of the inclusions, which resulted in a high amount of acicular ferrite [1,2]. Acicular ferrite was established as a favored microstructure in steel welds [3–5]. However, the strength of acicular ferrite is limited. In order to create the next generation of steel welds, stronger microstructures like martensite mixed with bainitic constituents had to be considered. This yielded welds with a yield strength of approx. 1000 MPa [6,7].

Currently, experiments are running with the goal of developing a filler material with a yield strength of 1100 MPa. Several alloying systems were used in previous studies, leading to promising results regarding both strength and toughness [8,9]. In these studies high resolution imaging methods were applied to analyze the microstructure of the welds [9]. It was shown that microalloying can serve as an alternative concept for welds regarding strengthening [8]. A combination of Ti, Nb and Al increased the strength of the welds effectively, as was predicted by thermodynamic and kinetic simulations. However, the type and nature of the presumably existing precipitates was not described in detail.

The microalloying elements Ti, Nb, Al and V are well known for their beneficial effects in several types of materials [10–12]. Because of their low solubility in ferrite, microalloy carbides and nitrides are very stable. They can form in several temperature and phase regions and are usually of MX-type. Regarding strength, precipitates formed in a supersaturated ferrite during reheating of the material are most effective [12].

One way to characterize the particles resulting from microalloying is using atom probe tomography [13]. The combination of nearly atomic resolution and information on the chemical identity of the measured atoms can deliver deep insights in the precipitation behavior of a material [14]. This has been used to identify precipitates in steels microalloyed with the classical microalloying elements, like Ti, Nb, V or Al [15–19], but also to identify clusters resulting from Cu additions [20,21] or to investigate numerous other alloy systems.

Recently, a method was established to directly observe hydrogen trapping in a material [22], which could be of great value for the welding community.

Nevertheless, in the research field of welding only few investigations involving atom probe tomography can be found. A good overview of the early use of atom probe on weld metals was given by Vitek and Babu [23]. In the last few years, atom probe tomography was mainly used to characterize the precipitation behavior of Cu-bearing pressure vessel steel welds [21,24–27] or to study welds of more exotic materials like Y-rich Ti-5111 [28], friction stir welds of nanostructured ferritic alloys [29] or dissimilar metal welds [30].

The current paper intends to point out the potential of using atom probe tomography for weld metal. A procedure for sample preparation and data evaluation for the special case of multi-layer weld metal is suggested. The method is used to investigate several differently microalloyed samples regarding their cluster and precipitate populations. By comparing these microstructural features with the resulting strength of the weld metal, this should clarify, which microalloying elements have the highest strengthening potential for steel welds.

2 Materials and methods

The investigated all-weld metal samples were produced by gas metal arc welding according to DIN EN ISO 15792-1. A macro-etched cross section of such an all-weld metal is shown in figure 1. Two groups of alloys were designed to investigate the influence of different microalloying elements on the precipitation characteristics.

In the first group several microalloying elements were added to the reference filler material, namely Ti, Nb, V, Al, and N. The chemical composition of the alloys was measured by optical emission spectroscopy and is stated in table 1. The O content was 400-500 ppm in all alloys. With this first alloy group it was intended to test the general effect of microalloying on the weld metal properties.

In the second group the microalloying elements were separated to clarify, which elements were driving the precipitation process. Therefore, specimens were fabricated containing V and Al separately (table 2). Please note, that an inherent content of ca. 50 ppm N and 100 ppm Ti is also present in alloys without an intended N or Ti addition.

The tensile strength of the samples was determined by tensile tests at room temperature according to EN ISO 6892-1 after a soaking treatment at 150 °C for 16 h to remove residual H.

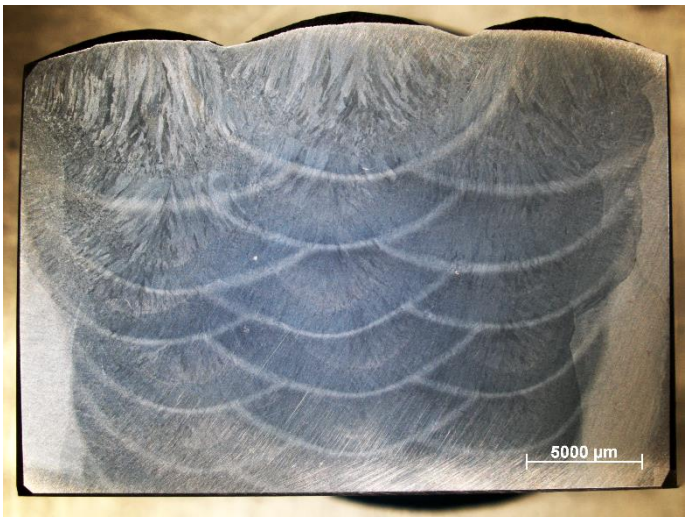

Figure 1: Cross-section of an all-weld metal sample, macro-etched with nital.

Table 1: Chemical composition of the alloys in group 1 and the reference alloy.

Group 1 – Ti-Nb-Al-V								
[m.%]	**C**	**Si**	**Mn**	**Ti**	**Nb**	**Al**	**V**	**N**
Reference	0.11	0.82	2.63	0.01	-	-	-	0.008
Ti-Nb-Al	0.10	0.91	2.67	**0.04**	**0.08**	**0.02**	-	**0.02**
Ti-Nb-Al-0.2V	0.10	0.92	2.65	**0.05**	**0.08**	**0.03**	**0.22**	**0.02**
Ti-Nb-Al-0.5V	0.10	0.89	2.63	**0.04**	**0.08**	**0.02**	**0.50**	**0.02**

Table 2: Chemical composition of the alloys in group 2.

Group 2 – Influence of single elements								
[m.%]	**C**	**Si**	**Mn**	**Ti**	**Nb**	**Al**	**V**	**N**
Al	0.08	0.76	2.40	0.01	-	**0.02**	-	0.005
0.3V	0.09	0.55	1.24	0.01	-	-	**0.31**	0.004
0.5V	0.08	0.57	1.27	0.01	-	-	**0.52**	0.005

For the characterization of the precipitates atom probe tomography was used. The atom probe measurements were performed in a Cameca LEAP 3000 X HR in laser mode with the following parameters: temperature 60 K, pulse repetition rate 250 kHz, laser energy 0.3 nJ, target evaporation rate 1 %. The specimens were prepared by cutting rods in welding direction with a cross section of 0.3 x 0.3 mm², followed by the well-known electrolytic two-step process [31] to generate sufficiently sharp tips. The specimen radius should be in the range of

10 to 50 nm. For an elaborate explanation of this two-step process and guidelines for the preparation of different materials please refer to [32].

Generally, all tips were prepared from random locations within the all-weld metal. Therefore, the thermal history of the tips cannot be specifically stated. Due to the multi-layer welding a bead is reheated shortly by the following welding beads. Per alloy 10 measurements at random locations were performed to gain statistically relevant results regarding the average precipitate population in the alloy.

In order to clarify, whether some of the precipitates formed during the initial cooling of the bead or all of them formed during reheating, additional samples of the last deposited bead (top middle bead in figure 1) were taken from alloy 0.5V, followed by the same measuring and evaluation protocol as for all other samples.

After the measurement the reconstructed tips were scanned for clusters or precipitates using isosurfaces and nearest neighbor distributions [33,34]. Both of these methods are used for visualizing local enrichments of atoms with the same chemical identity. Enriched areas were exported in separate files before analyzing the chemical composition of these exported clusters or precipitates.

3 Results

3.1 Alloy group 1

The tensile tests showed, that the combined addition of Ti, Nb and Al resulted in a significant strength increase compared to the reference sample (table 3), which was already shown in [8]. By adding V in a comparatively high amount (0.2 m.%) the strength could be improved further. Increasing the amount of V to 0.5 m.% again brought additional strength.

The microstructural investigations with the atom probe revealed precipitates in the order of 1 to 10 nm. An exemplary image of a reconstruction of a tip from the alloy Ti-Nb-Al-0.5V is shown in figure 2. The pink dots represent Fe atoms in the ferritic matrix. In blue isoconcentration surfaces are depicted, visualizing local enrichments of Ti, V, C and N with an added content of > 20 at.%. Therefore, in this case precipitates containing Ti, V, C and N were found. Size and chemistry varied within each alloy and within each measured tip, and also depended on the alloy system itself. These variations are addressed in section 4.

Table 3: Tensile properties of the samples from group 1.

Mechanical properties: Group 1 – Ti-Nb-Al-V		
[MPa]	**R_m**	**$R_{p0.2}$**
Reference	1128	1006
Ti-Nb-Al	1204	1082
Ti-Nb-Al-0.2V	1258	1139
Ti-Nb-Al-0.5V	1272	1164

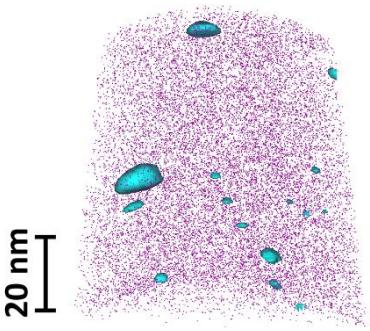

Figure 2: Exemplary image of a reconstruction of an atom probe measurement of a microalloyed sample. Pink dots represent iron atoms. The blue isoconcentration surfaces show enrichments in Ti, V, C and N and represent the precipitates.

The evolution of the average precipitate chemistry and size depending on the alloy composition is shown in table 4. In the sample Ti-Nb-Al the precipitates contain mainly Ti and C. There is still much Fe dissolved in the precipitates, whereas only little Nb and N was found in the precipitates. Al is completely missing in table 4 because it was always homogeneously distributed in the atom probe sample (exemplarily shown in figure 3). The precipitates had a size from 1 to 5 nm. An addition of V changed the average precipitate chemistry fundamentally. The precipitates contained approximately equal amounts of Ti, V, N, and C. Only little Fe was measured, most of which was close to the shell of the precipitates. An increase from 0.2V to 0.5V resulted in no changes in precipitate chemistry but enhanced the average size of the precipitates from 5 nm to approx. 10 nm.

The remaining V content in the steel matrix was investigated by exporting and analyzing a cylindrical region of interest which did not contain any precipitates (figure 4). Although a significant amount of V was incorporated in the precipitates, 80 to 90 % of all V atoms were still dissolved in the steel matrix in both alloys.

Table 4: Evolution of the average chemical composition in at.% and size of the precipitates in the alloys of group 1. The rest to 100 at.% in each average chemical composition accounts for matrix elements, which were neglected for the interpretation of the results.

Element	Ti-Nb-Al	Ti-Nb-Al-0.2V	Ti-Nb-Al-0.5V
Ti	**22** ± 10	**15** ± 4	**17** ± 4
Nb	**6** ± 2	**8** ± 4	**7** ± 1
V	-	**18** ± 2	**19** ± 6
N	**7** ± 4	**15** ± 4	**20** ± 4
C	**15** ± 13	**19** ± 4	**17** ± 4
Fe	**40** ± 8	**14** ± 3	**12** ± 4
Precipitate size	1-5 nm	5 nm	10 nm

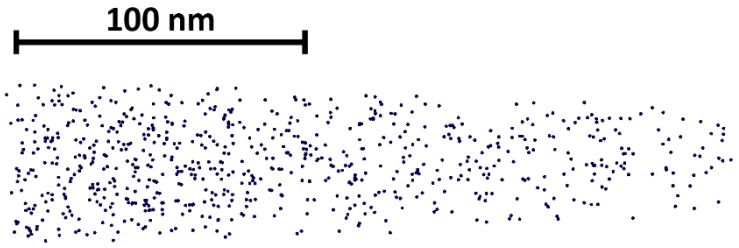

Figure 3: Example of Al atoms in an Al alloyed sample. The Al atoms are homogeneously distributed and showed no sign of clustering.

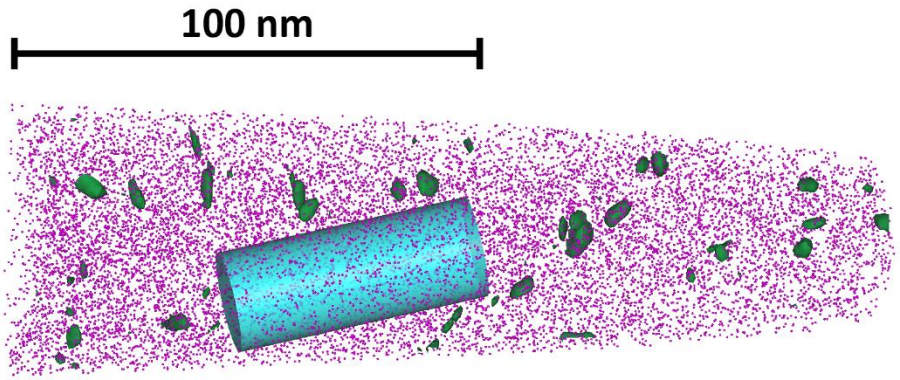

Figure 4: Reconstruction of an atom probe measurement of a V alloyed sample. The existence of small V-rich precipitates is evident. The cylindrical region of interest was exported to analyze the remaining V content in the steel matrix.

3.2 Alloy group 2

In table 5 the tensile properties of the samples from group 2 are compared to the reference sample. The Al sample did not show any improvement in strength. Contrarily, an addition of V led to a strength increase, similarly to the V samples in group 1. Especially the yield strength was drastically improved. In all cases the formed precipitates were investigated with the atom probe.

The atom probe measurements of the Al alloyed sample revealed, that Al is again homogeneously distributed and does not show any signs of clustering (figure 3).

In the 0.3V sample early clustering signs were identified. From nearest neighbor distributions it can be seen, that V starts to cluster first, before attracting C and N to form nm-sized precipitates. The average chemical composition of these V(C,N) clusters is shown in table 6.

The increase from 0.3V to 0.5V led to significant changes in amount, size and chemistry of the clusters (table 6). Many more clusters occurred in the 0.5V sample, which were also bigger in size. The amount of N dissolved in the clusters dropped drastically due to the limited amount of N available in the alloy, resulting in V-C precipitates. In both cases a high amount of Fe was measured in the clusters and precipitates, coming again mainly from the shell regions of the clusters and precipitates.

Also in this group the V content in the steel matrix was evaluated. In the 0.3V sample 80 to 90 % of all V atoms remained in the matrix. This value drops to approx. 65 % for the 0.5V sample.

4 Discussion

The main objective of this paper was to clarify, if microalloying induces precipitation and therefore strengthening in all-weld metal samples. Furthermore, it was evaluated which microalloying elements were most effective in strengthening. Microalloy carbides and nitrides are known to be very stable and generally have a positive effect on the mechanical properties in a variety of steels [10]. Nevertheless, the amount of precipitates found in the samples and their effect on the mechanical properties in the case of the all-weld metal was unknown so far.

Table 5: Tensile properties of the samples from group 2.

Mechanical properties: Group 2 – Single el.		
[MPa]	**R_m**	**$R_{p0.2}$**
Reference	1128	1006
Al	1109	998
0.3V	1155	1100
0.5V	1181	1128

Table 6: Evolution of the average chemical composition in at.% and size of the clusters in the alloys of group 2. The rest to 100 at.% in each average chemical composition accounts for matrix elements, which were neglected for the interpretation of the results.

Element	**0.3V**	**0.5V**
V	**34** ± 3	**30** ± 2
N	**14** ± 2	**2** ± 0.4
C	**11** ± 3	**26** ± 2
Fe	**31** ± 6	**25** ± 4
Precipitate size	1-3 nm	5 nm

Before the effectiveness of the different microalloying elements is discussed, some methodological issues should be elaborated. The all-weld metal is a multi-layer structure, in which every layer has its own reheated zone. The temperature profile measured with thermocouples in [35] suggests three reheating peaks with temperatures ranging from 300 to 600 °C for a weld bead coming from the subsequently deposited beads. The time of reheating is only a few seconds for each peak.

Firstly, the moment of formation of the precipitates had to be determined. Thermodynamic and kinetic simulations predicted, that the majority of precipitates will not form during the initial cooling of the weld bead, but will form during reheating above 500 °C in the ferrite temperature range [35]. In order to validate this prediction, samples were taken from the top bead of the 0.5V alloy, which did not undergo any reheating by subsequently deposited beads. The soaking treatment should not affect the precipitation state because of its low temperature. Several atom probe measurements of these top bead samples confirmed the prediction from the simulations: No signs of clustering or precipitation of V were found, allowing the conclusion that, if precipitates form, they will form during reheating.

Secondly, the irregularity of the thermal history inside the all-weld metal has to be considered. The temperature profile in [35] can only serve as an example regarding both the number of peaks and the peak temperatures. Due to the occurring temperature fluctuations and gradients during welding of every bead, any arbitrarily chosen location in the weld metal will have a unique thermal history with a different number of reheating peaks and different peak temperatures ranging from 200 °C up to the melting point. Atom probe tomography is a locally very restricted method. The measured sample volume is very small (usually less than 1/1000 μm^3). Because it is impossible to predict the exact thermal history of a specific point in the all-weld metal, it was decided to capture the overall precipitation behavior of an alloy by taking 10 samples from random locations and averaging the gained results. As expected, the precipitate population was different for every sample of the same alloy. This also explains the occasionally high standard deviation in the average chemical composition of the precipitates.

However, the thermal history is not the only influence causing irregularities in the precipitation population. During solidification of the weld, interdendritic segregation of several alloying elements (especially Mn, Cr, Mo, but also V) occurs, leading to locally changing chemical compositions. Microprobe maps in figure 5 show elemental distributions of Mn, which segregates the most, and V. These segregations change the premises for precipitation of microalloy carbides or nitrides.

Despite these difficulties, a general trend of the precipitation behavior of differently microalloyed samples could be observed by averaging several measurements of every alloy. A combined addition of Ti, Nb and Al resulted in the formation of Ti-rich carbonitrides (table 4). Although Nb and Al can both induce precipitation in some steels [10], they played minor roles in this case (see also [35]).

The tendency of precipitate formation was strongly enhanced by additionally alloying V to this Ti-Nb-Al sample, causing bigger precipitates to form (table 4). Much V was incorporated in the precipitates. This fact initiated the production of alloys containing only V as a microalloying element.

Very small clusters were observed in the 0.3V alloy, with V clustering first before attracting C and N to form very small precipitates. As the N content was very low in the samples alloyed only with V, it is no surprise that the precipitates in the 0.5V alloy, which were bigger in size, contained mainly C rather than N (table 6).

At this point it has to be mentioned, that with an addition of up to 0.5 m.% V, the term “microalloying” may not be feasible anymore. Nevertheless, this large amount of typical microalloying elements is necessary to increase the potential for clustering and precipitate

formation, because the reheating peaks are very short. To some extent, it is surprising that precipitates up to 10 nm are formed during this short time after all.

The mechanical properties changed drastically with the addition of microalloying elements. Due to the precipitate formation a strength increase of 100 MPa and more was achieved. However, an increase in V content from 0.2 m.% or 0.3 m.% to 0.5 m.% brought only little additional strength in both alloy groups, although the found precipitates were larger in both cases. Therefore, the first formation of many small clusters due to a moderate addition of V has much more effect on the strength than their growth.

Of course, with this strength increase the remaining toughness of the alloy becomes an issue. Also microalloying reduced the toughness of the investigated all-weld metals. However, with some adjustments in the alloy system the toughness decrease can be kept to a minimum.

Overall, the concept of using the multi-layer design of the all-weld metal for precipitation of microalloy carbides and nitrides was successfully applied. The short reheating peaks were sufficient for precipitates to form, strengthening the all-weld metal significantly.

This proposed filler metal is intended for constructions in the as-welded condition. A post weld heat treatment is assumed to be not applicable because of the high V content which might lead to severe precipitate growth and therefore deterioration of the toughness.

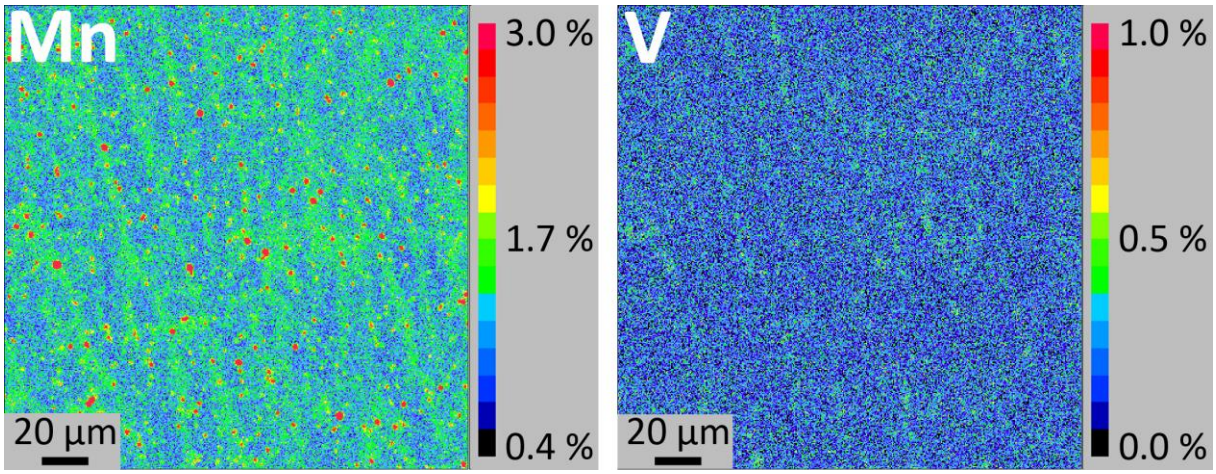

Figure 5: Microprobe mapping of Mn and V in the all-weld metal showing interdendritic segregation. The red dots in the Mn mapping are Mn-rich inclusions, which do not affect the precipitate formation.

5 Conclusions

The effect of microalloying on ultra-high strength weld metal produced by gas metal arc welding was investigated regarding the existence of precipitates and their influence on the mechanical properties. The following conclusions can be drawn:

- Microalloying of all-weld metal with Ti, Nb, V and Al yielded a significant strength increase.
- With atom probe tomography it was shown, that the strength increase resulted from nm-sized precipitates. Severe fluctuations in number density, size and chemical composition of the precipitates were observed within every alloy.
- Ti and V showed a strong tendency for clustering. Nb was limitedly incorporated in the TiV-precipitates. Al showed no signs of clustering in the all-weld metal.
- The precipitates did not form during the initial cooling of the weld, but during reheating by subsequently deposited weld beads.
- Due to inherent fluctuations in local thermal history and local chemical composition in the all-weld metal, an average precipitation state has to be evaluated from several measurements.

6 Acknowledgement

The K-Project Network of Excellence for Metal JOINing is fostered in the frame of COMET - Competence Centers for Excellent Technologies by BMWFW, BMVIT, FFG, Land Oberösterreich, Land Steiermark, Land Tirol and SFG. The program COMET is handled by FFG.

7 References

1. Evans GM (1995) Microstructure and properties of ferritic steel welds containing Al and Ti. Weld J 74:249s–261s.
2. Vanovsek W, Bernhard C, Fiedler M, Schnitzer R (2013) Effect of titanium on the solidification and postsolidification microstructure of high-strength steel welds. Weld World 57:665–674. doi: 10.1007/s40194-013-0063-1
3. Farrar RA, Harrison PL (1987) Acicular ferrite in carbon-manganese weld metals: An overview. J Mater Sci 22:3812–3820. doi: 10.1007/BF01133327
4. Sugden A, Bhadeshia H (1989) Lower acicular ferrite. Metall Trans A 20:1811–1818.
5. Babu SS, Bhadeshia HKDH (1991) Mechanism for the Transition from Bainite to Acicular Ferrite. Mater Trans 32:679–688.
6. Keehan E, Karlsson L, Thuvander M, Bergquist E (2007) Microstructural Characterisation of As-Deposited and Reheated Weld Metal — High Strength Steel Weld Metals. Weld World 51:44–49. doi: 10.1007/BF03266559
7. Keehan E, Zachrisson J, Karlsson L (2010) Influence of cooling rate on microstructure and properties of high strength steel weld metal. Sci Technol Weld Join 15:233–238. doi: 10.1179/136217110X12665048207692
8. Schnitzer R, Zügner D, Haslberger P, et al (2017) Influence of alloying elements on the mechanical properties of high-strength weld metal. Sci Technol Weld Join 22:536–543. doi: 10.1080/13621718.2016.1274095
9. Haslberger P, Ernst W, Schnitzer R (2017) High resolution imaging of martensitic all-weld metal. Sci Technol Weld Join 22:336–342. doi: 10.1080/13621718.2016.1240980
10. Gladman T (1997) The physical metallurgy of microalloyed steels. The Institute of Materials, London
11. Lagneborg R, Siwecki T, Zajac S, Hutchinson B (1999) The Role Of Vanadium In Microalloyed Steels. Scand. J. Metall.
12. Baker TN (2009) Processes, microstructure and properties of vanadium microalloyed steels. Mater Sci Technol 25:1083–1107. doi: 10.1179/174328409X453253
13. Miller MK, Forbes RG (2009) Atom probe tomography. Mater Charact 60:461–469. doi: 10.1016/j.matchar.2009.02.007
14. Marquis EA, Hyde JM (2010) Applications of atom-probe tomography to the characterisation of solute behaviours. Mater Sci Eng R Reports 69:37–62. doi: 10.1016/j.mser.2010.05.001
15. Craven AJ, MacKenzie M, Cerezo A, et al (2008) Spectrum imaging and three-dimensional atom probe studies of fine particles in a vanadium micro-alloyed steel. Mater Sci Technol 24:641–650. doi: 10.1179/174328408X270347
16. Xie KY, Zheng T, Cairney JM, et al (2012) Strengthening from Nb-rich clusters in a Nb-microalloyed steel. Scr Mater 66:710–713. doi: 10.1016/j.scriptamat.2012.01.029
17. Enloe CM, Findley KO, Parish CM, et al (2013) Compositional evolution of microalloy carbonitrides in a Mo-bearing microalloyed steel. Scr Mater 68:55–58. doi: 10.1016/j.scriptamat.2012.09.027
18. Nöhrer M, Zamberger S, Primig S, Leitner H (2013) Atom probe study of vanadium interphase precipitates and randomly distributed vanadium precipitates in ferrite. Micron 54–55:57–64. doi: 10.1016/j.micron.2013.08.008
19. Kapoor M, O'Malley R, Thompson GB (2016) Atom Probe Tomography Study of Multi-microalloyed Carbide and Carbo-Nitride Precipitates and the Precipitation Sequence in Nb-Ti HSLA Steels. Metall Mater Trans A Phys Metall Mater Sci 47:1984–1995. doi: 10.1007/s11661-016-3398-6

20. Isheim D, Kolli RP, Fine ME, Seidman DN (2006) An atom-probe tomographic study of the temporal evolution of the nanostructure of Fe-Cu based high-strength low-carbon steels. Scr Mater 55:35–40. doi: 10.1016/j.scriptamat.2006.02.040

21. Wang H, Yu X, Isheim D, et al (2013) High strength weld metal design through nanoscale copper precipitation. Mater Des 50:962–967. doi: 10.1016/j.matdes.2013.03.093

22. Chen Y-S, Haley D, Gerstl SSA, et al (2017) Direct observation of individual hydrogen atoms at trapping sites in a ferritic steel. Science (80-) 355:1196–1199. doi: 10.1126/science.aal2418

23. Vitek JM, Babu SS (2011) Multiscale characterisation of weldments. Sci Technol Weld Join 16:3–11. doi: 10.1179/1362171810Y.0000000003

24. Miller MK, Pareige P, Burke MG (2000) Understanding pressure vessel steels: an atom probe perspective. Mater Charact 44:235–254. doi: 10.1016/S1044-5803(99)00056-X

25. Miller MK, Russell KF (2007) Embrittlement of RPV steels: An atom probe tomography perspective. J Nucl Mater 371:145–160. doi: 10.1016/j.jnucmat.2007.05.003

26. Wang HH, Tong Z, Hou TP, et al (2017) Effects of evolution of nanoscale copper precipitation and copper content on mechanical properties of high-strength steel weld metal. Sci Technol Weld Join 22:191–197. doi: 10.1080/13621718.2016.1213583

27. Edmondson PD, Miller MK, Powers KA, Nanstad RK (2016) Atom probe tomography characterization of neutron irradiated surveillance samples from the R. E. Ginna reactor pressure vessel. J Nucl Mater 470:147–154. doi: 10.1016/j.jnucmat.2015.12.038

28. Kolli RP, Herzing AA, Ankem S (2016) Characterization of yttrium-rich precipitates in a titanium alloy weld. Mater Charact 122:30–35. doi: 10.1016/j.matchar.2016.10.014

29. Mazumder B, Yu X, Edmondson PD, et al (2016) Effect of friction stir welding and post-weld heat treatment on a nanostructured ferritic alloy. J Nucl Mater 469:200–208. doi: 10.1016/j.jnucmat.2015.11.061

30. Choi KJ, Kim T, Yoo SC, et al (2016) Fusion boundary precipitation in thermally aged dissimilar metal welds studied by atom probe tomography and nanoindentation. J Nucl Mater 471:8–16. doi: 10.1016/j.jnucmat.2015.12.047

31. Miller MK, Cerezo A, Hetherington MG, Smith GDW (1996) Atom probe field ion microscopy. Clarendon Press, Oxford

32. Miller MK, Forbes RG (2014) Atom-Probe Tomography: The Local Electrode Atom Probe. doi: 10.1007/978-1-4899-7430-3

33. Larson DJ, Prosa TJ, Ulfig RM, et al (2013) Local Electrode Atom Probe Tomography - A User's Guide. Springer Science+Business Media, New York

34. Chen Y, Chou PH, Marquis EA (2014) Quantitative atom probe tomography characterization of microstructures in a proton irradiated 304 stainless steel. J Nucl Mater 451:130–136. doi: 10.1016/j.jnucmat.2014.03.034

35. Schnitzer R, Zügner D, Haslberger P, et al (2016) IIW Document II-C-491-16: Influence of alloying elements on the mechanical properties of ultra-high strength weld metal.

Paper V

Haslberger P, Holly S, Ernst W, Schnitzer R (2018)

Microstructure and mechanical properties of high-strength steel welding consumables with a minimum yield strength of 1100 MPa

Journal of Materials Science 53: 6968-6979

DOI: 10.1007/s10853-018-2042-9

Microstructure and mechanical properties of high-strength steel welding consumables with a minimum yield strength of 1100 MPa

Phillip Haslberger[a], Sylvia Holly[b], Wolfgang Ernst[c], Ronald Schnitzer[a]

[a] Department Physical Metallurgy and Materials Testing, Montanuniversität Leoben, Austria

[b] voestalpine Böhler Welding Austria GmbH, Kapfenberg, Austria; now with: voestalpine Wire Technology GmbH, Bruck/Mur, Austria

[c] voestalpine Stahl Linz GmbH, Austria

Abstract

Welded high-strength steel components have great potential for use in lightweight constructions or highly loaded structures. Welding of steels with a yield strength of more than 1100 MPa is particularly challenging because of the toughness requirements for the weld metal. Currently, a new generation of welding consumables with a minimum yield strength of 1100 MPa has been developed. Based on electron backscatter diffraction and atom probe tomography a concept for toughening and strengthening of all-weld metal samples was deployed. Starting from a martensitic all-weld metal sample with an approximate yield strength of 1000 MPa, a reduction in manganese and silicon content resulted in a refined microstructure with a lower prior austenite grain size and effective grain size. Furthermore, a higher average grain boundary misorientation was measured, which influences the toughness positively. An addition of vanadium caused the formation of vanadium-rich clusters, which increased the strength of the all-weld metal significantly. With a combination of these two mechanisms it was possible to produce an all-weld metal sample with the required yield strength of more than 1100 MPa and an acceptable toughness.

1 Introduction

In lightweight constructions and for highly loaded components high-strength steels are frequently used. Welding plays a crucial role in manufacturing of these constructions. Due to the high demand a variety of steels with a strength in the range of 1000 to 1300 MPa is currently available. However, gas metal arc welding and other modern welding techniques require the use of a suitable filler material. Although it was shown that undermatching welding consumables can be sufficient for some welding processes and conditions [1–3], a new generation of welding consumables with a higher strength level is desirable, while keeping the toughness above 47 J at -20 °C.

Recently, an approach was made to add microalloying elements to a metal-cored wire to strengthen the weld metal [4]. This approach showed promising results and the outcomes of further experiments with vanadium alloying are discussed elsewhere [5]. Based on these investigations, the strengthening effect of vanadium was incorporated in the alloying concept of this study. Of course, the tradeoff between strength and toughness cannot be neglected, particularly in the field of welding of high-strength steels, where thermomechanical processing or heat treatments are inefficient or unwanted. Therefore, the main topic of this paper will be the influence of several alloying elements on the microstructure and consequently the toughness of the investigated weld metal.

A few studies on the influence of different alloying elements on the mechanical properties of high-strength weld metal have been performed in the last decades [6–12]. A comprehensive survey was performed by Keehan et al., who considered several influences on the mechanical behavior of steel welds produced by shielded metal arc welding with a strength in the range of 800 to 1000 MPa. They varied the contents of carbon, nickel and manganese and correlated the contents to strength and toughness [6–8]. The correlation was based on microstructural investigations, which showed the existence of a mixture of upper and lower bainite, coalesced bainite and martensite [9]. Additionally, an optimum cooling time between 800 and 500 °C of about 3 to 13 s was determined [10]. In this range a fine microstructure was observed, which was predominantly made responsible for the good strength and toughness. Also other groups investigated the microstructure of this class of material and found the same mixture of bainite and martensite with similar conclusions [11,12].

However, the desired strength level for the consumable in the current paper requires a fully martensitic microstructure also in the weld metal. A proper way to characterize martensitic all-weld metal was reported in [13] and [14]. The strength and toughness of martensite and the most probable crack propagation paths have been discussed intensely in the last few years

by interpreting electron backscatter diffraction (EBSD) results and fracture surfaces. On the one hand, it was concluded that block boundaries are effective grain boundaries for the strengthening of martensite because they hinder dislocation movement [15–17]. On the other hand, the issue of toughness was addressed from several points of view. The fracture path of cleavage crack experiments was investigated in several studies [17–22]. From these studies one can summarize that cracks can propagate through sub-block boundaries, but not through block boundaries. Therefore, the block size can be interpreted as the effective grain size for toughness and should be small to maximize crack deflection. The misorientation angle chosen for the effective grain size should be about 15°, as the misorientation between sub-blocks is in the range of 5 to 11° [16,18].

One further important influence regarding the toughness of steel is the prior austenite grain size (PAGS). High-strength weld metals in the as-welded condition usually exhibit a columnar PAG structure due to the temperature gradient existing [23–25]. The width of the PAG columns depends on the solidification path – which depends on the chemical composition of the liquid weld pool [25] – and the amount of existing inclusions [24]. In high-strength steel weld metal the width of the PAG columns was associated with the amount of acicular ferrite. Large PAGs promoted the formation of acicular ferrite which is beneficial for toughness [26,27]. Contrarily, in martensitic steels a small PAGS is generally thought to promote a high toughness. The block size is linearly dependent on the PAGS [28–30]. Therefore, a small PAGS will lead to a small block size, increasing the toughness of the material.

As a consequence, this paper will focus on the evaluation of the effective grain size and its correlation to toughness in martensitic all-weld metal samples. The PAG structure will be investigated regarding its influence on the block size. Grain size variations depending on the chemical composition of the weld metal will be addressed.

Furthermore, an optimized alloying concept will be presented for a new welding consumable with increased strength and adequate toughness.

2 Materials and methods

The study was carried out on all-weld metal samples which were fabricated according to DIN EN ISO 15792-1 by gas metal arc welding with metal-cored wires. These samples are built up by seven layers with three weld beads in each layer (figure 1). This weld metal design eliminates any influence of the base material on the chemical composition of the weld by dilution and is used to characterize the welding consumable itself. The $t_{8/5}$ cooling time for

this kind of sample was measured with thermocouples and is about 5 s for the used set of welding parameters in table 1.

The chemical composition of the investigated alloys was measured by optical emission spectroscopy and is stated in table 2. The approximate oxygen content is between 400 and 500 ppm for all samples. Alloy A generally contains the highest amount of alloying elements. Compared to alloy B particularly the carbon content is increased. The main difference between alloys A/B and alloys C/D is the reduced silicon and manganese content in the alloys C/D. Alloy D was additionally alloyed with vanadium for strengthening purposes.

Figure 1: Macro-etched all-weld metal sample.

Table 1: Applied welding parameters for the all-weld metal sample.

Current	Voltage	Welding speed	Heat input per unit length	Interpass temperature	Wire diameter	Contact tip to work distance
250 A	30 V	50 cm min^{-1}	9 kJ cm^{-1}	150 °C	1.2 mm	15-20 mm

Table 2: Chemical composition of the investigated alloys in wt.%.

	C	Si	Mn	P	S	Cr+Mo+Ni	V	N
Alloy A	0.12	0.81	2.4	0.012	0.009	4.6	0	0.005
Alloy B	0.08	0.74	2.4	0.009	0.009	3.9	0	0.010
Alloy C	0.08	0.46	1.1	0.008	0.010	4.8	0	0.005
Alloy D	0.09	0.52	1.6	0.012	0.009	4.3	0.22	0.010

One sample for tensile testing with d = 10 mm and l_0 = 50 mm, and three Charpy V-notch impact testing samples with a cross section of 10 x 10 mm² were machined out of the all-weld metal samples per alloy for determination of the mechanical properties. The V-notch was located in the middle of the all-weld metal according to DIN EN ISO 15792-1.

EBSD was used for the microstructural characterization of the weld metal. The sample was tilted to 70° and the scanning electron microscope was operated at 30 kV and a specimen current of ca. 10 nA. Other scan parameters can be found in [13]. The EBSD scans were performed on cross-sections of the welds and covered a large area (magnification from 300x to 800x) to maximize statistics. As a compromise between acquisition time and scan resolution a step size of 200 to 300 nm was chosen. The measurements were carried out in the last deposited bead because only there influences from reheating of the material can be ruled out. For evaluation of the effective grain size a tolerance angle of 15° was used. Based on the crystallographic orientation relationship between martensite and prior austenite, the PAG structure was reconstructed from the large EBSD scans using ARPGE [31]. The orientation relationship documented by Greninger and Troiano [32] yielded the highest reconstruction quality. The PAG column width was evaluated by applying the linear intercept method. The lines were drawn perpendicular to the longitudinal direction of the PAGs.

For characterization of precipitates atom probe tomography (APT) was carried out. Several tips were prepared electrolytically from random locations within the all-weld metal and were measured in laser mode at a temperature of 60 K with a laser energy of 0.3 nJ and a pulse repetition rate of 250 kHz.

3 Results

3.1 Mechanical testing

The results of the mechanical testing are summarized in table 3. Regarding tensile strength and yield strength no clear trend was observed for samples A, B and C. Contrarily, both tensile and yield strength of sample D are significantly higher. Alloys A/B have a lower impact toughness than alloys C/D, especially at -20°C.

Table 3: Mechanical properties of the investigated alloys.

	R_m [MPa]	$R_{p0.2}$ [MPa]	A_V at RT	A_V at -20 °C
Alloy A	1121	953	31 ± 7	21 ± 4
Alloy B	1089	1034	51 ± 1	34 ± 2
Alloy C	1054	993	83 ± 2	70 ± 4
Alloy D	1178	1119	50 ± 2	50 ± 2

3.2 Toughness improvement and microstructure – alloys A, B, C

At first, the influence of carbon, manganese and silicon on the microstructure of alloys A,B and C was determined. Alloy D is not shown at this point because of its elevated vanadium content and will be presented in section 3.3. The short cooling time and the alloying content resulted in a fully martensitic microstructure. Figures 2a-2c show inverse pole figure (IPF) + image quality (IQ) maps of locations in the last deposited weld bead of alloys A, B and C. The typical needle-shaped morphology of martensite can be identified in all three alloys. While the blocks in alloys A/B show mostly parallel arrangements, alloy C comprises a more chaotic arrangement of blocks with large areas with interlocked structures similar to acicular ferrite [26,33]. Additionally, the blocks seem to be refined in alloys B and C. The optical appearance of these microstructures was quantified by evaluating the effective grain size and the misorientation distribution from several EBSD scans.

In table 4 these values are compared with the martensite start temperature (Ms) calculated from the formula below [34].

$$M_S = 543 - (347C - 4C^2) - (10.4Ni + 0.5Ni^2) - (28.8Mn - 0.26Mn^2) + (9.7Co - 0.2Co^2) - (15.5Cr - 0.58Cr^2) + (4Si - 0.22Si^2) - (1.3Mo + 0.3Mo^2) + (4Ti - 0.38Ti^2) - C(27Ni + 27Mn + 20Co + 15Cr + 35Si + 12Mo + 90Ti)$$

The effective grain size decreases, and the average misorientation increases with rising Ms. This trend is graphically represented in figure 3. Furthermore, figure 4 shows the relationship between Ms and impact toughness at room temperature (Av RT) and at -20 °C (Av -20 °C). The impact toughness increases with rising Ms. The difference between room temperature and -20 °C remains nearly constant.

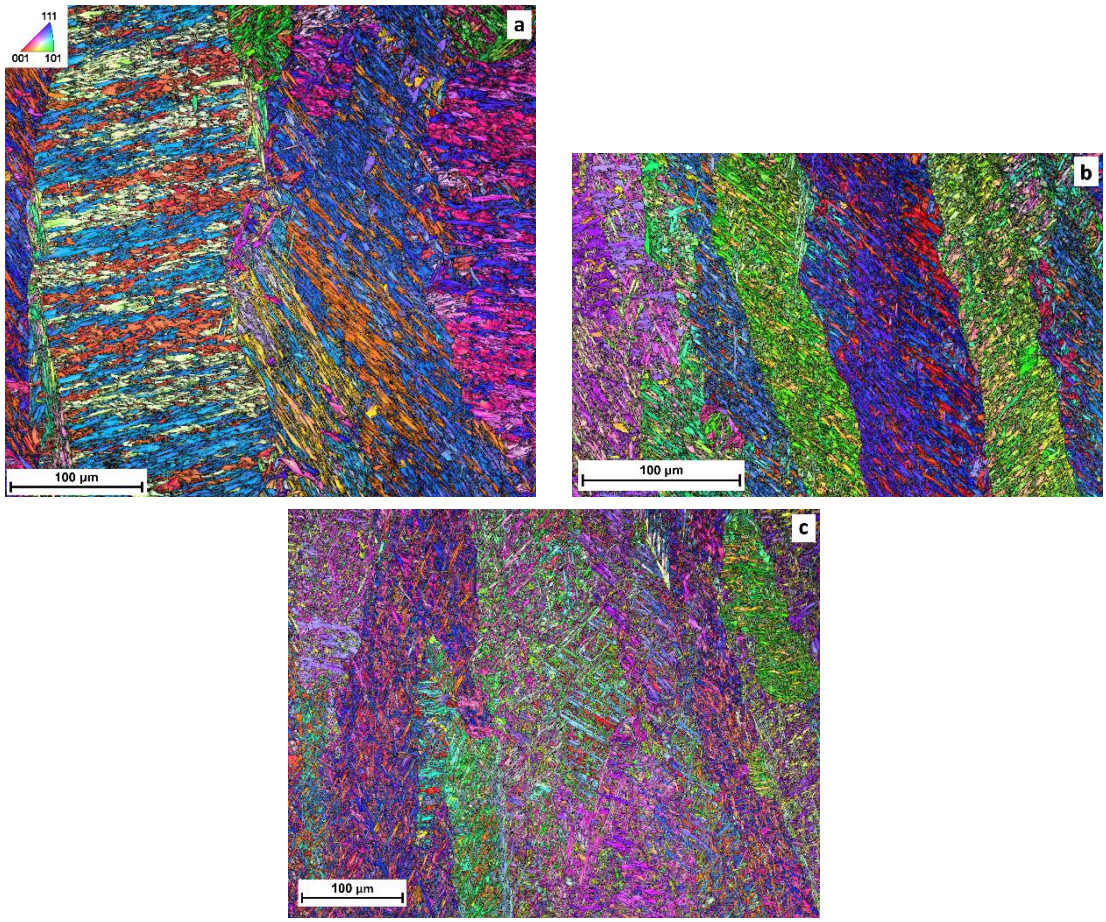

Figure 2: Results from EBSD Scans: IPF + IQ maps of locations in the last deposited bead of each alloy. **a** Alloy A, **b** alloy B, **c** Alloy C.

Table 4: Comparison of martensite start temperature (Ms) [34] and evaluated effective grain size (EGS) and average misorientation (avM) from EBSD measurements.

	Ms [°C]	**EGS [µm]**	**avM [°]**
Alloy A	362	8.34 ± 1.28	30.3
Alloy B	397	5.70 ± 1.13	34.4
Alloy C	421	4.59 ± 1.05	38.1

The PAG structure was reconstructed from the EBSD scans with ARPGE, resulting in the images in figures 5a-5c. Different PAGs are separated by black lines. The columnar nature of the PAGs is clearly visible. Comparing the three alloys, it is evident that the PAGs of alloy A are much coarser than in alloys B and C. The same situation was found at several different locations in the last deposited bead for each alloy. These scans from several locations per alloy were used to evaluate the corresponding PAGS. The determined values for the PAGS are listed in table 5

together with the effective grain size. A linear relationship between effective grain size and PAGS is evident, with a factor of approx. 0.11. This relationship is discussed in section 4.

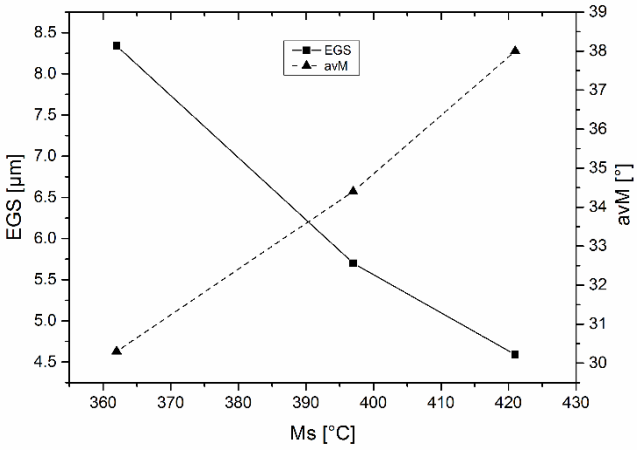

Figure 3: Martensite start temperature (Ms) versus effective grain size (EGS) and average misorientation (avM) of alloys A, B and C.

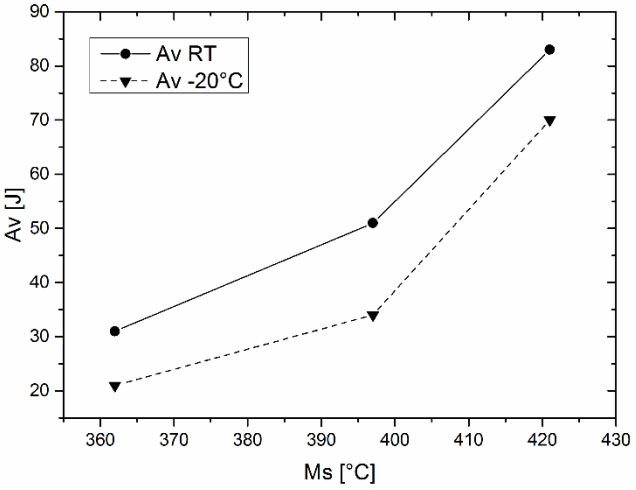

Figure 4: Martensite start temperature (Ms) versus impact toughness at room temperature (Av RT) and at -20 °C (Av -20 °C) of alloys A, B and C.

3.3 Combination of strength and toughness improvement – alloy D

For strengthening purposes alloy D contained 0.22 wt.% vanadium, which increased the corresponding mechanical values significantly. APT with its nearly atomic resolution was used to study signs of clustering or precipitation in the all-weld metal sample.

Primarily the nearest neighbor distributions (NND) of vanadium atoms were used to identify signs of clustering in the alloy. The NNDs in the reconstructed tips were significantly different

from the distributions of the randomized data sets. In most cases distinct peaks were visible with a closer distance of nearest neighbors than would be expected from the randomized data sets. The NND of one reconstruction of a sample of alloy D is depicted in figure 6. The peak at 1 nm is a clear sign for clustering of vanadium atoms. Furthermore the clusters were visualized by isoconcentration surfaces with a concentration value of 2 at.% (figure 7a), 4 at.% (figure 7b) and 10 at.% (figure 7c). The clusters were only visible at small concentration values, contained mostly vanadium, carbon and nitrogen and were still very rich in iron.

The microstructure of alloy D was also investigated with EBSD (figure 8) to verify the microstructural changes due to the manganese and silicon content reduction. The martensitic structure looked similar to alloy C, which means the martensite blocks were mostly interlocked and refined. The evaluated effective grain size was 3.34 ± 0.18 µm, the average misorientation was 39.7° and the PAGS was 49 ± 27 µm. These values are discussed in context with the Ms in section 4.

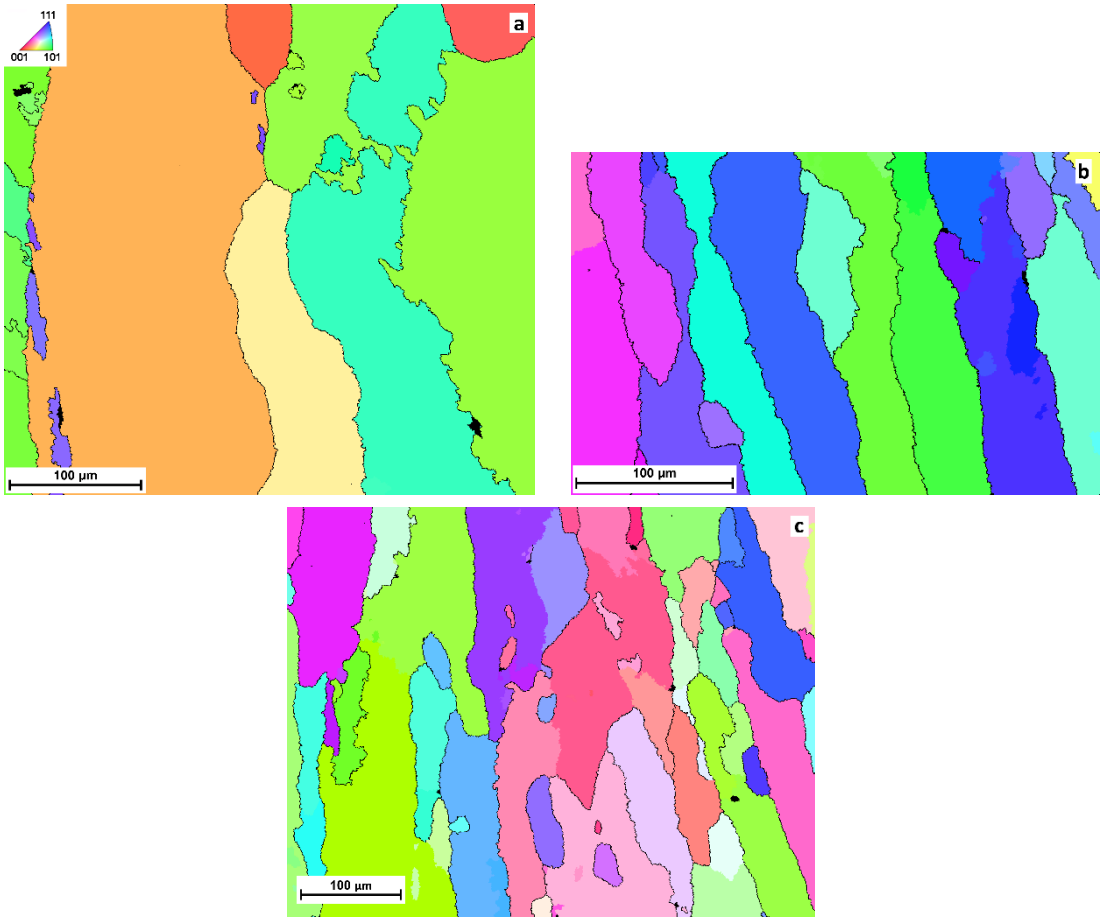

Figure 5: IPF maps of the PAG reconstructions of the scans in figure 2. **a** Alloy A, **b** alloy B, **c** alloy C.

Table 5: Evaluated PAGS of alloys A-C with comparison to effective grain size (EGS).

	PAGS [µm]	EGS [µm]
Alloy A	75 ± 50	8.34 ± 1.28
Alloy B	50 ± 29	5.70 ± 1.13
Alloy C	43 ± 22	4.59 ± 1.05

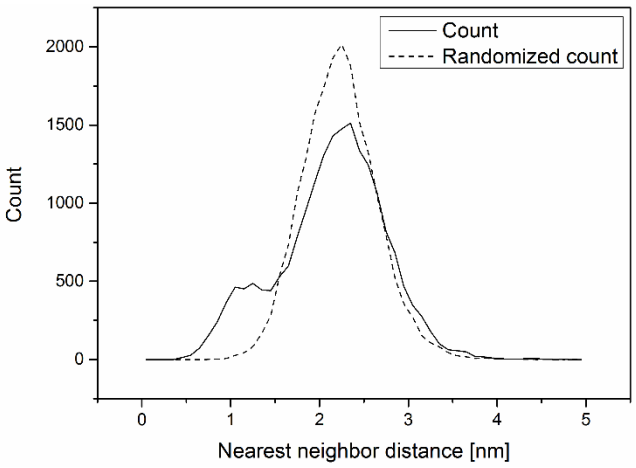

Figure 6: Nearest neighbor distribution of vanadium in an APT sample of alloy D. The peak at about 1 nm distance is a clear sign for clustering of vanadium atoms.

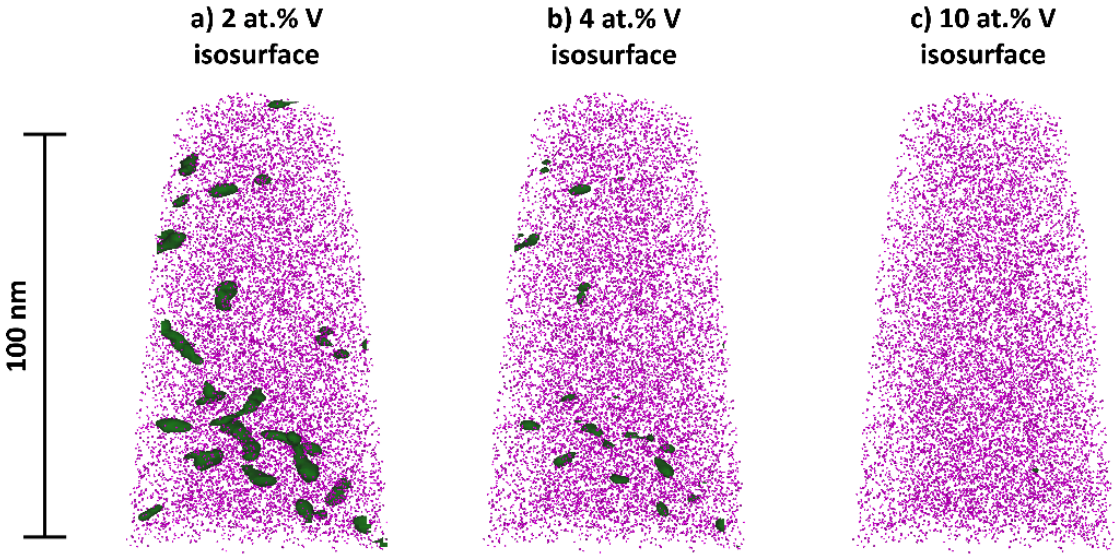

Figure 7: Reconstructed tip of an atom probe measurement of alloy D. The pink dots represent the iron matrix of the alloy. Vanadium isoconcentration surfaces with concentration values of **a** 2 at.%, **b** 4 at.% and **c** 10 at.% visualize the existence of vanadium-rich clusters.

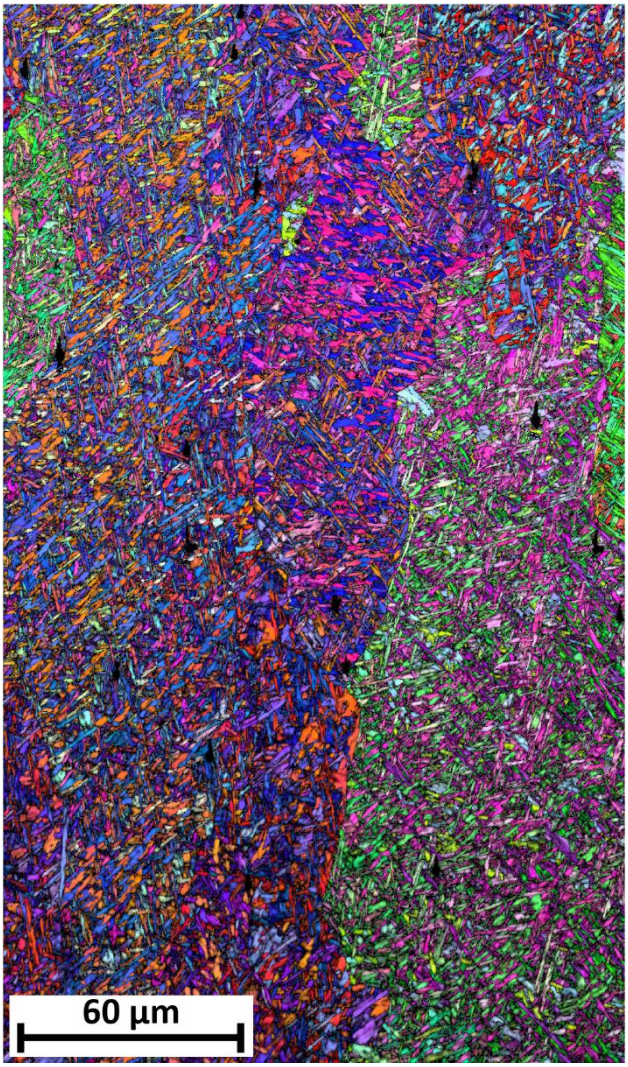

Figure 8: Result from EBSD scan: IPF + IQ map of location in the last deposited bead of alloy D.

4 Discussion

The aim of this study was to develop a new generation of welding consumables for welding of high-strength steels. The effects of adjustments in the alloying system on the microstructure and the mechanical properties were investigated using EBSD and APT.

Generally, the welding parameters (voltage, current, speed, etc.) have great influence on the resulting weld [35]. For example, they govern heat input and cooling time, dilution and geometry of the weld. However, when keeping the welding parameters constant, the chemical composition of the weld is the main influence on the microstructure and therefore the mechanical properties of all-weld metal samples.

Starting from a high-strength steel welding consumable with a guaranteed yield strength of 960 MPa the contents of carbon, manganese and silicon were varied to study their influence on the martensitic microstructure. A decrease in carbon content from 0.12 wt.% in alloy A to 0.08 wt.% in alloy B influenced the mechanical properties positively. The tensile strength was decreased, but both yield strength and impact toughness were increased. The optical appearance of the microstructure of the different alloys already indicated, that alloy C had a refined structure with a more chaotic arrangement of the martensitic blocks (figure 2c). This appearance was verified by showing, that alloy C had a smaller effective grain size (4.59 µm) and a higher average misorientation (38.1°) than alloys A and B (table 4). This higher amount of high angle boundaries and smaller size of martensitic blocks implies a higher probability for crack deviation and therefore a higher toughness of the material [18,21], which was confirmed in the current study.

The linear relationship between block size and PAGS in martensitic microstructures [28–30] was checked by reconstructing the EBSD scans with ARPGE and determining the column width of the PAGs with the linear intercept method. This column width was compared with the effective grain size, which is slightly higher than the block size of martensitic samples. The linear relationship was confirmed (table 5), meaning that the PAGS may govern the effective grain size and therefore the toughness of the material. However, figure 3 suggests a linear dependence of the effective grain size on the Ms, meaning that the Ms may be responsible for grain size changes in the material.

In fact, by comparing Ms and PAGS and their relationship (figure 9) one can assume that the Ms acts as indicator of the alloying content of the material. Changing the chemical composition of the weld to increase the Ms will result in a decrease of the PAGS and consequently the effective grain size, which will benefit the toughness of the weld. This theory should not be confused with the often reported phenomenon that the Ms depends on the PAGS [30,36–39], because that relationship is only valid for chemically identical materials with different PAGSs varied by different austenitization temperatures. The reasons for the dependency of the PAGS on the chemical composition of the weld are unclear and should be investigated. Also the reasons for the change from a more parallel arrangement of the martensitic blocks in alloys A and B to a more chaotic arrangement in alloy C are not identified yet and could be subject of further investigations.

Nevertheless, these beneficial changes in microstructure due to a lower manganese and silicon content were applied to the newly developed welding consumable to optimize the toughness.

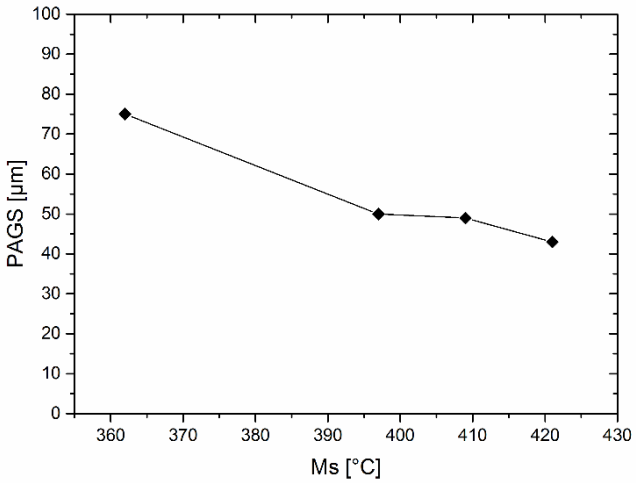

Figure 9: Martensite start temperature (Ms) versus prior austenite grain size (PAGS) of alloys A, B, C and D.

An addition of vanadium can be used to strengthen the all-weld metal sample in the as-welded condition. In other applications the addition of vanadium is typically lower than 0.1 wt.% (vanadium is a well-known microalloying element) [40]. However, in the investigated type of welded material an addition of min. 0.2 wt.% vanadium is necessary to attain significant strengthening [5]. Due to the welding process the material is reheated very shortly by subsequent welding passes. During this short time small clusters can form, if the vanadium concentration is high enough to guarantee a high clustering potential. Compared to other microalloying elements (Ti, Nb, Al), which were also tried in previous studies [4], vanadium showed the highest strengthening potential and was therefore chosen for this new generation of welding consumables. APT revealed small iron-rich vanadium carbonitride clusters in alloy D (figure 7) which increase the strength of the weld.

Alloy D combines the discussed concepts for strengthening and toughening of the welding consumable. For reference the microstructure parameters and impact toughness of alloy D were added to figure 3 and figure 4 in figure 10 and figure 11, respectively. Compared to the other alloys, alloy D had the lowest effective grain size and the highest average misorientation and therefore does not fit in the general trend (figure 10). Presumably, vanadium also plays a role in refining the martensitic block structure. He and Edmonds [41] proposed a mechanism in bainitic steels, that vanadium rich regions in the PAG promote intragranular nucleation of the ferrite plates, leading to the well-known acicular ferrite structure with a smaller grain size and a superior toughness compared to bainitic structures. A similar mechanism could be responsible for the refinement of the martensitic structure in alloy D of the current study. Nevertheless, this additional grain refinement can only act positively on the mechanical

properties and counteracts the toughness loss from the vanadium cluster formation. The resulting toughness (figure 11) is in an acceptable range. Particularly, the impact toughness at -20 °C does not seem to suffer from the vanadium cluster formation and fulfills the requirement of 47 J at -20 °C.

Overall, the combination of increasing the Ms by reducing the manganese and silicon content and adding vanadium to induce cluster formation resulted in a possible new generation of high-strength steel welding consumables with an increased strength and adequate toughness.

The fatigue performance of this welding consumable was not investigated so far. In the last few years the concept of low transformation temperature (LTT) filler wires emerged for welding of ultra-high strength steels because of the resulting compressive residual stresses and low welding distortion, which act positively on the fatigue strength [42–44]. From that point of view, the current study with its suggestion to increase the Ms worked in the opposite direction, and the resulting weld will probably have tensile residual stresses [42]. However, despite its much lower alloying content, the static strength of the current material is much higher than the static strength of LTT wires. Also, LTT wires typically contain high amounts of nickel and chromium, which makes them quite costly compared to the proposed low alloy filler wire. Consequently, the fatigue performance of the current material should be a focus of following studies.

In the intended applications the high-strength steel welds are usually deployed in the as-welded condition. That is also recommended for the current welding consumable, as the high vanadium content might induce severe precipitate formation and possibly deterioration of toughness after a post weld heat treatment.

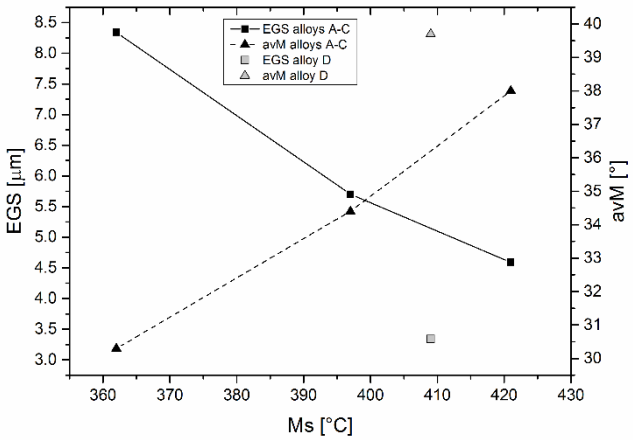

Figure 10: Martensite start temperature (Ms) versus effective grain size (EGS) and average misorientation (avM) of alloys A, B, C and D.

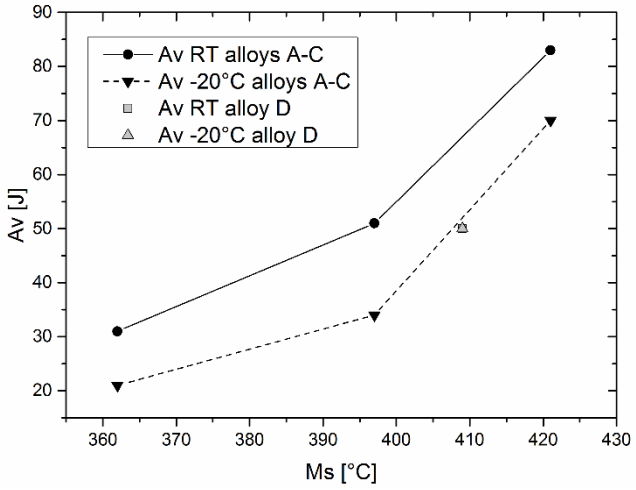

Figure 11: Martensite start temperature (Ms) versus impact toughness at room temperature (Av RT) and at -20 °C (Av -20 °C) of alloys A, B, C and D.

5 Conclusions

A new generation of welding consumables for high-strength steels was developed by changing the alloying contents of carbon, manganese, silicon and vanadium. The produced all-weld metal samples were characterized regarding their microstructure with EBSD and APT. The relationship between microstructure and mechanical properties was determined and directly applied to the new welding consumable. The following conclusions can be drawn from the investigations:

- Lowering the manganese and silicon content and consequently increasing the martensite start temperature resulted in a lower prior austenite grain size and effective grain size and a higher average grain boundary misorientation of the martensitic microstructure. These microstructural changes improved the impact toughness of the weld metal.
- Vanadium alloying strengthened the weld metal significantly due to the formation of vanadium-rich clusters. Furthermore, an additional refinement of the martensitic microstructure due to the vanadium alloying was observed.
- A combination of the toughening concept and the strengthening concept was used to produce an all-weld metal sample with a strength of more than 1100 MPa while keeping the impact toughness above 47 J at room temperature and at -20 °C.

6 Acknowledgement

The K-Project Network of Excellence for Metal JOINing is fostered in the frame of COMET - Competence Centers for Excellent Technologies by BMWFW, BMVIT, FFG, Land Oberösterreich, Land Steiermark, Land Tirol and SFG. The program COMET is handled by FFG.

7 References

1. Khurshid M, Barsoum Z, Mumtaz NA (2012) Ultimate strength and failure modes for fillet welds in high strength steels. Mater Des 40:36–42. doi: 10.1016/j.matdes.2012.03.048
2. Lan L, Kong X, Qiu C, Zhao D (2016) Influence of microstructural aspects on impact toughness of multi-pass submerged arc welded HSLA steel joints. Mater Des 90:488–498. doi: 10.1016/j.matdes.2015.10.158
3. Schneider C, Ernst W, Schnitzer R, et al (2018) Welding of S960MC with undermatching filler material. Submitted to Weld World.
4. Schnitzer R, Zügner D, Haslberger P, et al (2017) Influence of alloying elements on the mechanical properties of high-strength weld metal. Sci Technol Weld Join 22:536–543. doi: 10.1080/13621718.2016.1274095
5. Haslberger P, Holly S, Ernst W, Schnitzer R (2018) Precipitates in microalloyed ultra-high strength weld metal studied by atom probe tomography. Submitted to Weld World.
6. Keehan E, Karlsson L, Andrén H-O (2006) Influence of carbon, manganese and nickel on microstructure and properties of strong steel weld metals, Part 1 - Effect of nickel content. Sci Technol Weld Join 11:1–8.
7. Keehan E, Karlsson L, Andrén H-O, Bhadeshia HKDH (2006) Influence of carbon, manganese and nickel on microstructure and properties of strong steel weld metals, Part 2 - Impact toughness gain resulting from manganese reductions. Sci Technol Weld Join 11:9–18.
8. Keehan E, Karlsson L, Andrén H-O, Bhadeshia HKDH (2006) Influence of carbon, manganese and nickel on microstructure and properties of strong steel weld metals, Part 3 - Increased strength resulting from carbon additions. Sci Technol Weld Join 11:19–24.
9. Keehan E, Karlsson L, Thuvander M, Bergquist E (2007) Microstructural Characterisation of As-Deposited and Reheated Weld Metal — High Strength Steel Weld Metals. Weld World 51:44–49. doi: 10.1007/BF03266559
10. Keehan E, Zachrisson J, Karlsson L (2010) Influence of cooling rate on microstructure and properties of high strength steel weld metal. Sci Technol Weld Join 15:233–238. doi: 10.1179/136217110X12665048207692
11. Wansheng D, Yun P, Hongjun X, et al (2010) Microstructure and Toughness of 1000 MPa High Strength Weld Metal. Mater Sci Forum 638–642:3441–3446.
12. Zhang T, Li Z, Ma S, et al (2016) High strength steel (600–900 MPa) deposited metals: microstructure and mechanical properties. Sci Technol Weld Join 21:186–193. doi: 10.1179/1362171815Y.0000000079
13. Haslberger P, Ernst W, Schnitzer R (2017) High resolution imaging of martensitic all-weld metal. Sci Technol Weld Join 22:336–342. doi: 10.1080/13621718.2016.1240980
14. Haslberger P, Holly S, Ernst W, Schnitzer R (2017) Microstructural Characterization of Martensitic All-Weld Metal Samples. Pract Metallogr 54:513–532. doi: 10.3139/147.110464

15. Shibata A, Nagoshi T, Sone M, et al (2010) Evaluation of the block boundary and sub-block boundary strengths of ferrous lath martensite using a micro-bending test. Mater Sci Eng A 527:7538–7544. doi: 10.1016/j.msea.2010.08.026

16. Mine Y, Hirashita K, Takashima H, et al (2013) Micro-tension behaviour of lath martensite structures of carbon steel. Mater Sci Eng A 560:535–544. doi: 10.1016/j.msea.2012.09.099

17. Du C, Hoefnagels JPM, Vaes R, Geers MGD (2016) Block and sub-block boundary strengthening in lath martensite. Scr Mater 116:117–121. doi: 10.1016/j.scriptamat.2016.01.043

18. Kim M-C, Jun Oh Y, Hwa Hong J (2000) Characterization of boundaries and determination of effective grain size in Mn-Mo-Ni low alloy steel from the view of misorientation. Scr Mater 43:205–211. doi: 10.1016/S1359-6462(00)00392-4

19. Gourgues A-F, Flower HM, Lindley TC (2000) Electron backscattering diffraction study of acicular ferrite, bainite, and martensite steel microstructures. Mater Sci Technol 16:26–40. doi: 10.1179/026708300773002636

20. Wang C, Wang M, Shi J, et al (2007) Effect of Microstructure Refinement on the Strength and Toughness of Low Alloy Martensitic Steel. J Mater Sci Technol 23:659–664.

21. Morris JW, Kinney C, Pytlewski K, Adachi Y (2013) Microstructure and cleavage in lath martensitic steels. Sci Technol Adv Mater 14:14208. doi: 10.1088/1468-6996/14/1/014208

22. Wu Q, Zikry MA (2014) Microstructural modeling of crack nucleation and propagation in high strength martensitic steels. Int J Solids Struct 51:4345–4356. doi: 10.1016/j.ijsolstr.2014.08.021

23. Bhadeshia HKDH, Svensson LE, Gretoft B (1986) The austenite grain structure of low-alloy steel weld deposits. J Mater Sci 21:3947–3951. doi: 10.1007/BF00553451

24. Grong O, Matlock DK (1986) Microstructural development in mild and low-alloy steel weld metals. Int Met Rev 31:27–48. doi: 10.1179/imtr.1986.31.1.27

25. Zhang Z, Farrar RA (1995) Columnar grain development in C-Mn-Ni low-alloy weld metals and the influence of nickel. J Mater Sci 30:5581–5588. doi: 10.1007/BF00356690

26. Farrar RA, Harrison PL (1987) Acicular ferrite in carbon-manganese weld metals: An overview. J Mater Sci 22:3812–3820. doi: 10.1007/BF01133327

27. Babu SS, Bhadeshia HKDH (1991) Mechanism for the Transition from Bainite to Acicular Ferrite. Mater Trans 32:679–688.

28. Morito S, Saito H, Ogawa T, et al (2005) Effect of Austenite Grain Size on the Morphology and Crystallography of Lath Martensite in Low Carbon Steels. ISIJ Int 45:91–94. doi: 10.2355/isijinternational.45.91

29. Galindo-Nava EI, Rivera-Díaz-del-Castillo PEJ (2015) A model for the microstructure behaviour and strength evolution in lath martensite. Acta Mater 98:81–93. doi: 10.1016/j.actamat.2015.07.018

30. Hidalgo J, Santofimia MJ (2016) Effect of Prior Austenite Grain Size Refinement by Thermal Cycling on the Microstructural Features of As-Quenched Lath Martensite. Metall Mater Trans A Phys Metall Mater Sci 47:1–14. doi: 10.1007/s11661-016-3525-4

31. Cayron C (2007) ARPGE: A computer program to automatically reconstruct the parent grains from electron backscatter diffraction data. J Appl Crystallogr 40:1183–1188. doi: 10.1107/S0021889807048777

32. Greninger AB, Troiano AR (1949) The mechanism of martensite formation. Trans AIME 185:590–598.

33. Wan XL, Wang HH, Cheng L, Wu KM (2012) The formation mechanisms of interlocked microstructures in low-carbon high-strength steel weld metals. Mater Charact 67:41–51. doi: 10.1016/j.matchar.2012.02.007

34. Galindo-Nava EI (2017) On the prediction of martensite formation in metals. Scr Mater 138:6–11. doi: 10.1016/j.scriptamat.2017.05.026

35. Messler RW (1999) Principles of Welding. doi: 10.1002/9783527617487

36. Brofman PJ, Ansell GS (1983) On the effect of fine grain size on the Ms temperature in Fe-27Ni-0.025C alloys. Metall Trans A 14:1929–1931. doi: 10.1007/BF02645565

37. Guimarães JRC, Rios PR (2010) Martensite start temperature and the austenite grain-size. J Mater Sci 45:1074–1077. doi: 10.1007/s10853-009-4044-0

38. García-Junceda A, Capdevila C, Caballero FG, de Andrés CG (2008) Dependence of martensite start temperature on fine austenite grain size. Scr Mater 58:134–137. doi: 10.1016/j.scriptamat.2007.09.017

39. van Bohemen SMC, Morsdorf L (2017) Predicting the Ms temperature of steels with a thermodynamic based model including the effect of the prior austenite grain size. Acta Mater 125:401–415. doi: 10.1016/j.actamat.2016.12.029

40. Lagneborg R, Siwecki T, Zajac S, Hutchinson B (1999) The Role Of Vanadium In Microalloyed Steels. Scand. J. Metall.

41. He K, Edmonds D V. (2002) Formation of acicular ferrite and influence of vanadium alloying. Mater Sci Technol 18:289–296. doi: 10.1179/026708301225000743

42. Francis JA, Stone HJ, Kundu S, et al (2009) The Effects of Filler Metal Transformation Temperature on Residual Stresses in a High Strength Steel Weld. J Press Vessel Technol 131:41401. doi: 10.1115/1.3122036

43. Ooi SW, Garnham JE, Ramjaun TI (2014) Review: Low transformation temperature weld filler for tensile residual stress reduction. Mater Des 56:773–781. doi: 10.1016/j.matdes.2013.11.050

44. Harati E, Karlsson L, Svensson LE, Dalaei K (2017) Applicability of low transformation temperature welding consumables to increase fatigue strength of welded high strength steels. Int J Fatigue 97:39–47. doi: 10.1016/j.ijfatigue.2016.12.007

Paper VI

Haslberger P, Ernst W, Schneider C, Holly S, Schnitzer R (2018)

Influence of inhomogeneity on several length scales on the local mechanical properties in V-alloyed all-weld metal

Submitted to Science and Technology of Welding and Joining

Influence of inhomogeneity on several length scales on the local mechanical properties in V-alloyed all-weld metal

Phillip Haslberger[a], Wolfgang Ernst[b], Christian Schneider[c], Sylvia Holly[d], Ronald Schnitzer[a]

[a] Department Physical Metallurgy and Materials Testing, Montanuniversität Leoben, Austria

[b] voestalpine Stahl Linz GmbH, Austria

[c] voestalpine Stahl Linz GmbH, Austria, Institute of Materials Science, Joining and Forming, Graz University of Technolgy, Austria

[d] voestalpine Böhler Welding Austria GmbH, Kapfenberg, Austria; now with: voestalpine Wire Technology GmbH, Bruck/Mur, Austria

Abstract

The mechanical properties of welding consumables for gas metal arc welding are classified by producing and testing all-weld metal samples, which are typically a multipass weld. Chemical and microstructural fluctuations of a vanadium alloyed all-weld metal sample on a macro- and microscale and their influence on the local mechanical properties were investigated. On a macroscale, hardness mappings show a pattern of hard and soft zones which can differ up to 60 HV. Despite the existence of these fluctuations, undersized Charpy V-notch tests revealed no significant difference between the last weld bead and the underlying ones. It is explained, how vanadium and its tendency to form precipitates affects both the hardness inhomogeneity and the toughness homogeneity.

1 Introduction

High strength steels are frequently welded by gas metal arc welding with matching welding consumables to produce components with a high load bearing capacity and a comparatively low weight. These components can be found in e.g. vehicles or cranes, where a low component weight can save a significant amount of energy. The mechanical properties of the produced welds depend on their geometry, number of layers and the used welding parameters. Of course, also the choice of a suitable chemical composition of the welding consumable is crucial. In order to classify the mechanical properties of the welding consumable itself, the production of all-weld metal samples according to DIN EN ISO 15792-1 is required. In this procedure a large gap is buffered and then filled layer by layer with the welding consumable. The result is a multilayer structure similar to fig. 1 with a reproducible number of beads depending on the chosen welding parameters. This sample design (and especially the buffering) eliminates influences from the chemical composition of the base material and should lead to a chemical composition of the weld metal which is only influenced by the chemical composition of the filler wire.

Such a multipass weld contains several sources of inhomogeneity on different scales. At first, the bead will solidify in a cellular or dendritic manner, which generates interdendritic segregations of alloying elements [1,2]. These segregations can affect the formation of different ferritic constituents in the weld metal during further cooling. This was described by Keehan et al. [2] for high strength weld metals produced by shielded metal arc welding and by Powell and Herfurth [3] for gas metal arc welds. In another study Haslberger et al. pointed out that these segregations could also influence the formation of clusters and precipitates in V-alloyed weld metal [4].

After delta ferrite formation, austenite columns will form upon cooling. Their size and shape may change throughout the weld bead. This phenomenon was investigated by Zhang and Farrar [5], who showed that the width of austenite columns can change throughout one weld bead depending on the nickel content. These factors (segregation and column growth) may influence the microstructure from a microscopic point of view.

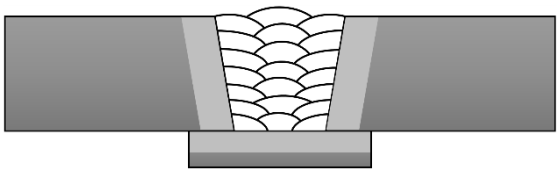

Figure 1: Schematic of an all-weld metal sample for the investigated type of welding consumables. The area shaded light grey is the buffer zone.

From a macroscopic point of view, every deposited bead is reheated by subsequent welding passes. Depending on the peak temperature this can effect remelting, reaustenitisation or tempering of the microstructure. As a result, zones with the original or altered microstructures exist in the weld, which was described in several studies [6–10]. The size of zones with different types of microstructure (i.e. columnar grains and refined equiaxed or recrystallized grains) is dependent on the used welding parameters [6]. The influence of the area fraction of columnar grains and recrystallized grains on the impact toughness is reported diversely [10]. While some indicated, that a high amount of reheated material is beneficial for impact toughness [11], others suggested that a low amount of reheated material is advantageous because of a higher homogeneity of the weld [12]. Another study claimed that the influence of the amount of reheated material is negligible [3]. Therefore, it can be summarized that the influence of the amount of reheated material on the impact toughness strongly depends on the investigated material and its microstructural condition.

Currently, a V-alloyed welding consumable with a yield strength of 1100 MPa was developed [4]. The produced all-weld metal samples were martensitic and contained V(C,N) precipitates [4,13]. The purpose of this study is to demonstrate the existence of chemical and microstructural inhomogeneities in this type of martensitic multipass weld metal and to clarify their influence on the mechanical properties of the weld. Special emphasis is put on the comparison between the last deposited bead and the middle of the all-weld metal due to their difference in thermal history. Hardness mappings and subsized Charpy V-notch tests are used to determine fluctuations of the local mechanical properties of the multipass weld. Microprobe investigations and microstructure comparisons are used to interpret the observed mechanical behaviour.

2 Materials and methods

The investigated all-weld metal samples were produced by gas metal arc welding according to DIN EN ISO 15792-1 using the welding parameters shown in tab. 1. In total, the weld metal consisted of 7 layers with 21 beads (fig. 1). The chemical composition of the weld metal is shown in tab. 2. The amount of alloying elements guarantees a fully martensitic weld metal for the expected cooling time between 800 and 500 °C of about 5 s. For an evaluation of the local mechanical behaviour of the weld metal hardness mappings and local Charpy V-notch tests were carried out. The Vickers hardness mappings were conducted with a load of 2 kg and a step size of 0.5 mm. Subsized Charpy V-notch samples with a cross section of 5 x 10 mm²

were prepared (fig. 2), dividing the all-weld metal sample in an upper, middle and lower area. In the upper samples a large part of the notch length was located in the last deposited bead, while the middle and lower samples contained a mixture of differently reheated material. Three samples were tested at each temperature according to DIN EN ISO 148-1, and the measured values were converted to the values for a 10 x 10 mm² sample by applying a geometric factor accounting for the size of the fractured area compared to a standard size sample [14].

For the investigations of interdendritic segregations electron probe micro analysis measurements were performed at an acceleration voltage of 15 keV and a probe current of 600 nA. A step size of 500 nm was chosen to ensure the ability to resolve the segregations. Light optical microscopy of the nital etched sample was used to identify zones with different microstructural appearance on a macro scale. EBSD measurements at 30 keV and 10 nA with a step size of 80 nm were used to determine local effective grain sizes inside the last deposited bead. The effective grains were defined by their misorientation tolerance angle of 15° [15] and their size was averaged by area. More information regarding sample preparation and EBSD parameters can be found in [13], which specifically addresses the microstructural characterization of all-weld metal samples with light optical microscopy and EBSD.

Table 1: Used welding parameters for the production of all-weld metal samples.

Current [A]	Voltage [V]	Welding speed [cm/min]	Heat input per unit length [kJ/cm]	Interpass temperature [°C]
250	30	50	9	150

Table 2: Chemical composition of the investigated material [m%].

C	Si	Mn	Cr	Mo	Ni	Cu	V	Fe
0.08	0.57	1.27	0.78	0.73	3.03	0.11	0.2-0.5	Rest

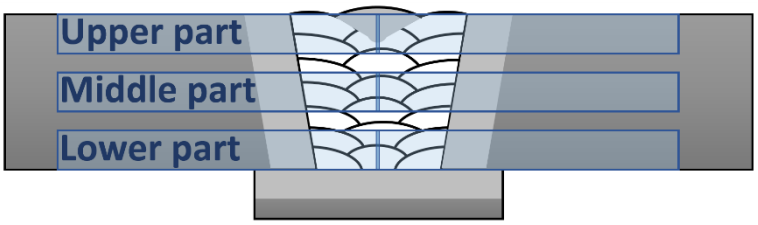

Figure 2: Schematic of the prepared subsized Charpy V-notch samples. The approximate shape of the last weld bead is outlined.

3 Results

3.1 Local impact toughness

The converted Charpy impact values from -60 to +20 °C for all three locations in the multipass weld are depicted in fig. 3. Generally, the impact toughness increases gradually with increasing temperature. There is no significant difference between upper, middle and lower part of the all-weld metal, and therefore no significant difference between top bead and tempered beads despite their diverse thermal history.

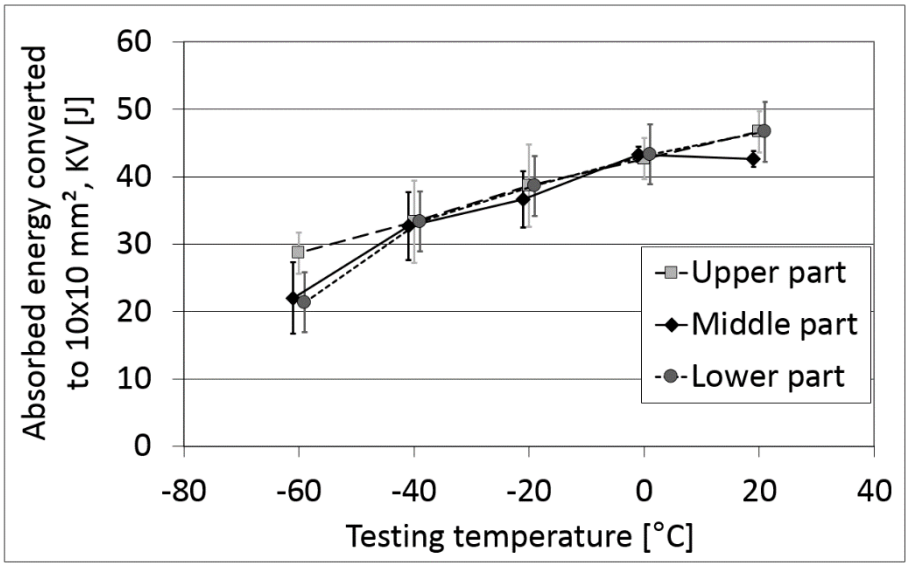

Figure 3: Results of the subsized Charpy V-notch tests from -60 to +20 °C.

3.2 Hardness mappings

For an assessment of hardness fluctuations in the multipass welds, hardness mappings were conducted over the whole weld metal. The hardness indents covered a large part of the sample, which is shown in fig. 4a, where also the position of the last, untempered bead is marked by a black line. The position of the last bead is different compared to the sample used for the Charpy V-notch tests. However, this should not affect the interpretation of the results. The resulting hardness map is shown in fig. 4b. Varying hardness values between 350 and 410 HV were observed. The yellow and orange colours (arrow in fig. 4b) in the last bead show that it is softer than the surrounding material. In the heat affected zone below the last bead a

harder area with ca. 410 HV and a soft zone with ca. 370 HV follow. Throughout the rest of the all-weld metal hard and soft zones appear in the shape of the corresponding weld beads and their heat affected zones, leading to an average hardness of ca. 380 HV.

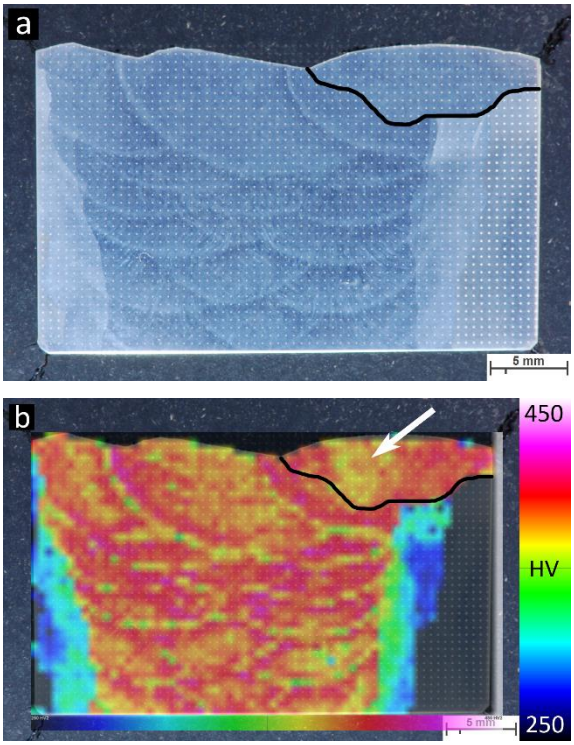

Figure 4: **a** Nital etched all-weld metal sample after hardness mapping. The melting line of the last deposited bead is indicated by a black line. **b** Color-coded hardness map of the V-alloyed sample superimposed on the image of the nital etched sample. The arrow points at the soft zone in the last weld bead.

3.3 Interdendritic segregations

Microprobe mappings of the elements Mn, Cr and V were conducted to assess the existence and the amount of interdendritic segregation in the material. All measured elements clearly segregated, which is visible in fig. 5. The red points in the Mn maps (fig. 5 a and b) originate from Mn-rich inclusions, which are homogeneously distributed over the whole weld metal. Consequently, they are not included in the further evaluation and interpretation of the interdendritic segregations visible in the map. Visually Mn segregates more than Cr (fig. 5 c and d) and V (fig. 5 e and f). The amount of segregation was evaluated by calculating the ratio

of the maximum local element concentration and the average concentration over the whole map. Both Mn and Cr showed maximum contents of about 120 % of the average value in the segregated regions. For V this value was even higher with 190 %. No difference between the top bead and the middle beads was observed, implying that reheating did not cause a redistribution of alloying elements on this length scale.

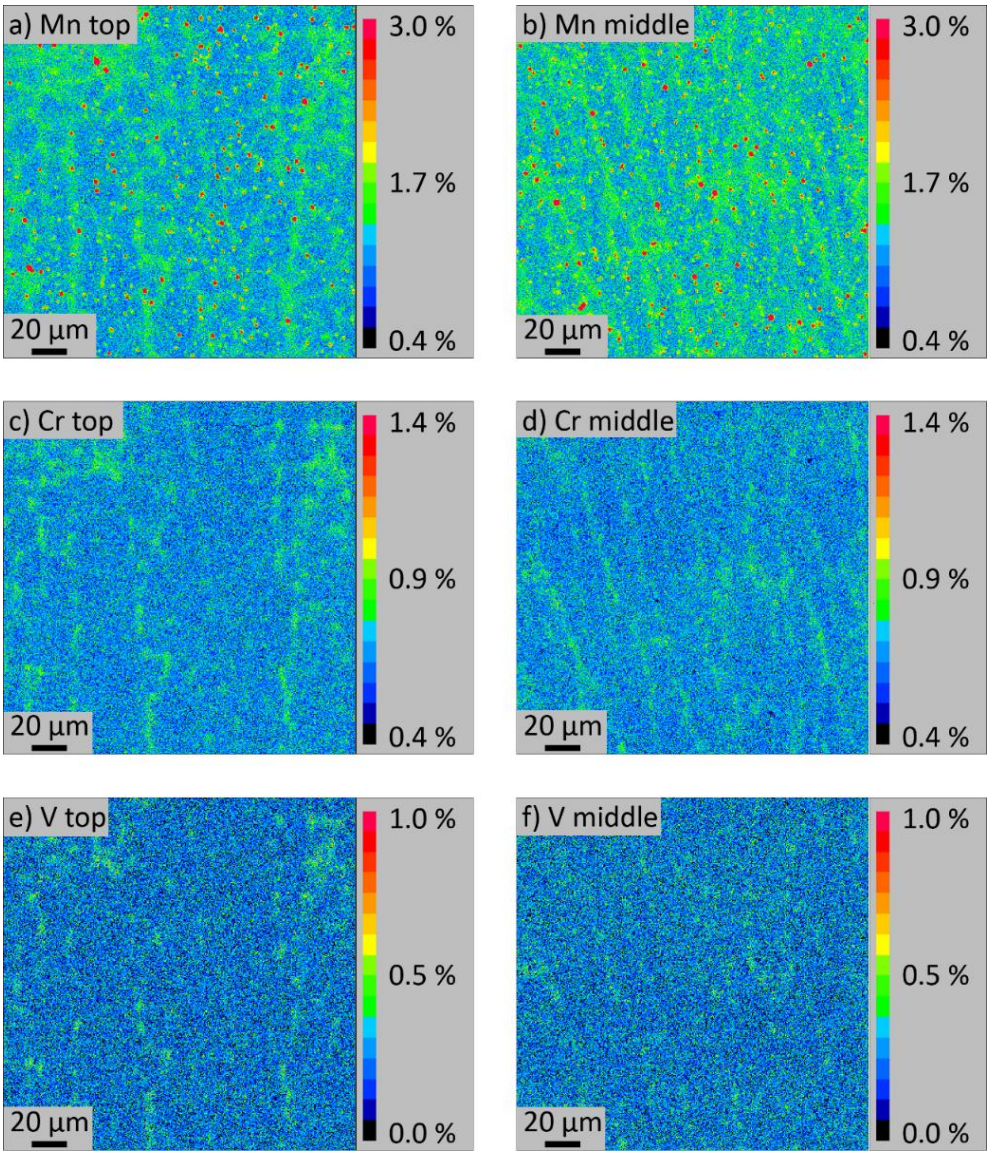

Figure 5: Microprobe mappings of sample with 0.2 m.% V. The distributions of Mn (a and b), Cr (c and d), and V (e and f) are shown for the top bead and the middle beads, respectively.

3.4 Grain size fluctuations

The nature of the multipass welding process implies the existence of grain size fluctuations between the passes due to reheating. This phenomenon of a mixture of zones with columnar grains and zones with equiaxed fine grains is well described in literature [6,7,10,12,16,17] and exemplarily shown in fig. 6 for the current material. On a different scale, grain size fluctuations inside a single weld bead may occur. Therefore, EBSD measurements were conducted at several positions in the last bead for a determination of the local effective grain size, which was defined by a tolerance angle of 15° [15,18]. This tolerance angle ensures that martensitic blocks are separated and that the grain size correlates to the fracture behaviour of the material [15]. The results in tab. 3 clearly indicate the existence of fluctuations of the effective grain size within the bead. Additionally, due to the irregular nature of the martensitic microstructure the standard deviation at each position is high. However, there was no evidence for changes in microstructure caused by the interdendritic segregations. The influence of the irregular microstructures on different scales will be discussed in the next section.

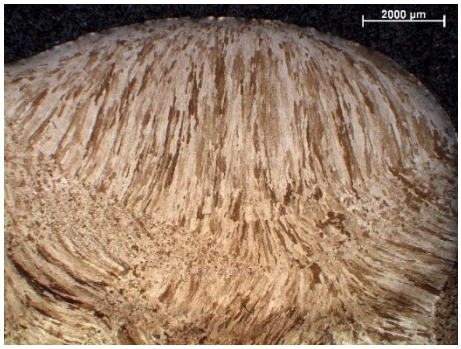

Figure 6: Last deposited bead and its surroundings etched with nital. Below the bead a zone consisting of equiaxed fine grains is visible.

Table 3: Local effective grain size in the last deposited bead depending on the distance to the fusion line.

Distance to the fusion line [mm]	Effective grain size [µm]
0.52	2.6 ± 1.6
2.4	2.7 ± 1.4
2.5	3.1 ± 2.1
3.8	2.8 ± 1.6
3.9	2.8 ± 1.7

4 Discussion

Several methods were used to investigate the influence of inhomogeneity on different scales on the local mechanical properties of a martensitic all-weld metal sample produced from a new type of welding consumables.

In multipass welds a weld bead will be heat treated by subsequent welding passes [7,12]. In the case of a martensitic weld metal this implies the assumption that the reheating will cause a tempering of the martensite which should generally increase the toughness [1]. Consequently, the last bead should have a higher strength and a lower toughness than the rest of the weld. However, the type of welding consumables investigated in this study is alloyed with V. This element is known for its potent strengthening effect in steels because of its tendency to form precipitates during reheating [4,19,20]. Therefore, hardness mappings and local Charpy V-notch tests were applied to study the local mechanical properties and the difference between the last weld bead and the underlying beads in this type of material.

The local Charpy V-notch tests delivered unexpected results. From fig. 3 it can be concluded that there is no significant difference between the impact toughness of the last bead (upper part) and the rest of the weld. Contrarily, the hardness mappings showed that the last bead is softer than the underlying structure (fig. 4). This behaviour can be explained by looking at the precipitate population in the material. In an atom probe study on the same type of material [4] it was proven that precipitates do not exist in the last bead. Compared to the rest of the weld, the toughness is hence not decreased by precipitate formation, but also there is no tempering of the martensitic matrix. These counteracting mechanisms result in a parity of the Charpy V-notch energies for all parts of the weld. The absence of V-rich precipitates in the last bead is also responsible for its comparatively low hardness.

Both the impact energy and the hardness show significant fluctuations. The standard deviation of the impact energy was up to 6 J (fig. 3). The hardness map depicts values between 350 and 410 HV for the weld metal (fig. 4). These fluctuations may stem from interdendritic segregations of alloying elements as well as grain size heterogeneity in the weld metal. As shown in fig. 5, several alloying elements tend to segregate during solidification in the investigated system. The effect of these segregations on the martensitic matrix is hard to quantify. According to tab. 3 the grain size varies depending on the location of the EBSD scan. However, there is no obvious evidence for a connection between interdendritic segregations and grain size. Nevertheless, it can be concluded that enrichments of elements like Mn, Cr and especially V will change the potential for precipitate formation. The resulting heterogeneity of the precipitate population will induce fluctuations in the local impact energy.

Furthermore, as each welding pass will create a heat affected zone inside the weld metal with areas of coarse grained microstructures and fine grained microstructures, a multilayer weld is always inhomogeneous in terms of grain size. The intercritical reheated zone may also contain areas with fresh martensite which leads to a local deterioration of both hardness and toughness [21,22]. This soft zone is clearly visible in fig. 4b. Additionally, the formation of precipitates is dependent on the reheating temperature. Hence, a Charpy V-notch sample will contain a mixture of zones with different grain sizes (fig. 6), microstructural constituents and precipitate populations, which may also lead to fluctuations in the impact energy values. Contrarily, fig. 3 shows as high standard deviations for the top bead as for the rest of the weld. Therefore, it can be concluded that these heterogeneities in the middle of the multipass weld are balanced over a whole Charpy V-notch sample and the impact energy of the mixed microstructure will always be similar despite the existing hardness fluctuations.

5 Conclusions

An all-weld metal sample was produced by gas metal arc welding with a V-alloyed welding consumable, resulting in a multipass weld with 21 weld beads. This type of material was investigated regarding its local mechanical properties and microstructural appearance with local Charpy V-notch tests, hardness mappings, microprobe, light optical microscopy and electron backscatter diffraction. The findings can be summarized as follows:

- There was no significant difference between the local impact energies of the last bead and the underlying weld. The last bead does not contain precipitates, but is also not tempered. In the underlying weld, the tempering of the martensitic microstructure counteracts the toughness loss by precipitate formation.
- The hardness of the last bead was lower compared to the rest of the weld because of the absence of V-rich precipitates.
- Multipass welding produces heat affected zones inside the weld with fluctuations of grain size and V-rich precipitate populations.
- Interdendritic segregations and effective grain size fluctuations are responsible for high standard deviations of the local impact toughness values.

6 Acknowledgement

The K-Project Network of Excellence for Metal JOINing is fostered in the frame of COMET - Competence Centers for Excellent Technologies by BMWFW, BMVIT, FFG, Land Oberösterreich, Land Steiermark, Land Tirol and SFG. The program COMET is handled by FFG.

7 References

1. Grong O, Matlock DK (1986) Microstructural development in mild and low-alloy steel weld metals. Int Met Rev 31:27–48. doi: 10.1179/imtr.1986.31.1.27
2. Keehan E, Karlsson L, Andrén H-O, Bhadeshia H (2006) New Developments with C-Mn-Ni High-Strength Steel Weld Metals, Part A — Microstructure. Weld J 85:200s–210s.
3. Powell GLF, Herfurth G (1998) Charpy V-notch properties and microstructures of narrow gap ferritic welds of a quenched and tempered steel plate. Metall Mater Trans A Phys Metall Mater Sci 29:2775–2784. doi: 10.1007/s11661-998-0318-4
4. Haslberger P, Holly S, Ernst W, Schnitzer R (2018) Precipitates in microalloyed ultra-high strength weld metal studied by atom probe tomography. Accepted for publication in Weld World.
5. Zhang Z, Farrar RA (1995) Columnar grain development in C-Mn-Ni low-alloy weld metals and the influence of nickel. J Mater Sci 30:5581–5588. doi: 10.1007/BF00356690
6. Yongyuth P, Ghosh PK, Gupta PC, et al (1992) Influence of Macro/Microstructure on the Toughness of “All Weld” Multipass Submerged Arc Welded C-Mn Steel Deposits. ISIJ Int 32:771–778.
7. Reed RC, Bhadeshia HKDH (1994) A simple model for multipass steel welds. Acta Metall Mater 42:3663–3678. doi: 10.1016/0956-7151(94)90432-4
8. Mythili R, Thomas Paul V, Saroja S, et al (2003) Microstructural modification due to reheating in multipass manual metal arc welds of 9Cr-1Mo steel. J Nucl Mater 312:199–206. doi: 10.1016/S0022-3115(02)01680-X
9. Avazkonandeh-Gharavol MH, Haddad-Sabzevar M, Haerian A (2009) Effect of copper content on the microstructure and mechanical properties of multipass MMA, low alloy steel weld metal deposits. Mater Des 30:1902–1912. doi: 10.1016/j.matdes.2008.09.023
10. Amrei MM, Monajati H, Thibault D, et al (2016) Microstructure characterization and hardness distribution of 13Cr4Ni multipass weld metal. Mater Charact 111:128–136. doi: 10.1016/j.matchar.2015.11.022
11. Jorge JC., Souza LF., Rebello JM. (2001) The effect of chromium on the microstructure/toughness relationship of C–Mn weld metal deposits. Mater Charact 47:195–205. doi: 10.1016/S1044-5803(01)00168-1
12. Bhadeshia HKDH, Svensson LE (1989) The microstructure of submerged arc-weld deposits for high-strength steels. J Mater Sci 24:3180–3188. doi: 10.1007/BF01139039
13. Haslberger P, Holly S, Ernst W, Schnitzer R (2017) Microstructural Characterization of Martensitic All-Weld Metal Samples. Pract Metallogr 54:513–532. doi: 10.3139/147.110464
14. Chao YJ, Ward JD, Sands RG (2007) Charpy impact energy, fracture toughness and ductile-brittle transition temperature of dual-phase 590 Steel. Mater Des 28:551–557. doi: 10.1016/j.matdes.2005.08.009

15. Kim M-C, Jun Oh Y, Hwa Hong J (2000) Characterization of boundaries and determination of effective grain size in Mn-Mo-Ni low alloy steel from the view of misorientation. Scr Mater 43:205–211. doi: 10.1016/S1359-6462(00)00392-4

16. Kikuta Y, Araki T, Yoneda M, et al (1982) The Reheated Zone Toughness of Multipass Weld Metal (Report 1). J Japan Weld Soc 51:359–365. doi: 10.2207/qjjws1943.51.359

17. Surian E, Ramini de Rissone M, De Vedia L (2005) Influence of Molybdenum on Ferritic High- Strength SMAW All-Weld-Metal Properties. Weld J 84:53–62.

18. Mine Y, Hirashita K, Takashima H, et al (2013) Micro-tension behaviour of lath martensite structures of carbon steel. Mater Sci Eng A 560:535–544. doi: 10.1016/j.msea.2012.09.099

19. Gladman T (1997) The physical metallurgy of microalloyed steels. The Institute of Materials, London

20. Lagneborg R, Siwecki T, Zajac S, Hutchinson B (1999) The Role Of Vanadium In Microalloyed Steels. Scand. J. Metall.

21. Akselsen OM, Solberg JK, Grong O (1988) Effects of martensite-austenite (M-A) islands on intercritical heat-affected zone toughness of low carbon microalloyed steels. Scand J Metall 17:194–200.

22. Matsuda F, Ikeuchi K, Fukada Y, et al (1995) Review of mechanical and metallurgical investigations of MA constituent in welded joint in japan. Trans JWRI 24:1–24.